Study on the properties of supported Pd catalysts and their resistance to sulfur poisoning

重信, 咲季

Study on the properties of supported Pd catalysts and their resistance to sulfur poisoning

Pd 担持触媒の特性および耐硫黄被毒性に関する研究

Saki Shigenobu

重信 咲季

Table of contains

Chapter 1 Introduction

1.1 Research background

The development of science and technology has enriched our lives. On the other hand, environmental problems caused by air pollutants emitted from both fixed and mobile sources, such as factories and automobiles, respectively, have become a global issue. Since the discovery of the iron catalyst to synthesize ammonia by Fritz Haber and Carl Bosch in the early 20th century, catalysts have been used to produce chemicals. In the 1960s, however, pollution was caused by byproducts of chemical production and environmental pollutants (for example, SOx, NOx) from energy production [1, 2]. In the 1980s, environmental issues became the subject of global debate. The United Nations World Commission on Environment and Development (WCED) issued a report titled "Our Common Future" that proposed the concept of sustainable development [3]. Furthermore, the United Nations adopted Sustainable Development Goals (SDGs) in 2015 [4]. In these goals, economic growth and industrial development are listed as “Goal 8: Promote sustained, inclusive and sustainable economic growth, full and productive employment and decent work for all” and “Goal 9: Build resilient infrastructure, promote inclusive and sustainable industrialization and foster innovation”. In addition, as in “Goal 3: Ensure healthy lives and promote well-being for all at all ages; 3.9 By 2030, substantially reduce the number of deaths and illnesses from hazardous chemicals and air, water and soil pollution and contamination” and “Goal 12. Ensure sustainable consumption and production patterns; 12.4 By 2020, achieve the environmentally sound management of chemicals and all wastes throughout their life cycle, in accordance with agreed international frameworks, and significantly reduce their release to air, water and soil in order to minimize their adverse impacts on human health and the environment”, some goals are related to the reduction of health hazards

caused by air pollutants. Economic development and environmental conservation must be compatible in order to establish a sustainable society.

1.2 Air pollution and catalysts

The air pollution issue must be resolved to establish a sustainable society. The health hazards caused by air pollution remain significant. The *Lancet* Commission on pollution and health reported that air pollution killed approximately 6-7 million people in 2019 [5].

The Air Pollution Control Law was established in Japan in 1968 to control air pollution. The Air Pollution Control Law includes emission controls for individual facilities such as factories and workplaces, total volume controls in designated areas, and limits on vehicle exhaust emissions [6]. Examples of air pollutants specified in this law include smoke (sulfur oxides and nitrogen oxides) and volatile organic compounds (VOCs) [7]. To comply with these regulations, various methods are used to remove air pollutants. For the case of VOCs, the methods can be broadly classified into adsorption and combustion methods. The adsorption method uses porous materials such as activated carbon and silica gel. The adsorption method has the advantage of being applicable to a wide range of gas concentrations and treatment volumes but has the disadvantage of requiring periodic replacement or regeneration of adsorbent materials, which is costly. Among combustion methods, the oxidative decomposition of gas containing VOCs at a high temperature of 600-900 °C is called the direct decomposition method. While the direct decomposition method can remove various types of hazardous substances, it has the disadvantages of requiring high energy for combustion and generating NOx. The catalytic combustion is one of combustion method. This method can decompose and remove even low-concentration substances and burn at lower temperatures than the direct combustion method. On the other hand, the catalytic combustion method has the disadvantage that it is expensive to replace the catalyst when it deteriorates.

Catalysts are used not only in the manufacture of chemical products but also for environmental cleanup. Various catalysts have been developed to purify environmental

pollutants emitted from factories and automobiles. Typical examples include desulfurization and denitrification catalysts in petroleum refining and three-way catalysts for purifying automobile exhaust gas (Table 1-1). Catalysts that contribute to environmental purification are called environmental catalysts.

Table 1-1. Examples of Air Pollutants [2].

	Environmental load	Source	Catalyst
NOx	photochemical smog, acid rain	gasoline car	Three-way catalyst
		diesel car	Storage reduction catalyst Urea-SCR Hydrocarbon-SCR
		thermal power station, garbage incinerator	Flue gas denitrification systems
CO	toxic	combustion equipment, automotive	Combustion catalysts, Automotive catalysts
SOx	acid rain	crude oil	Hydrodesulfurization catalyst
VOC	health damage	building materials	Photocatalyst
particulate matter	respiratory impairment	diesel car	Catalytic Combustion

1.3 Supported Pd catalyst

1.3.1 Characteristics of supported Pd catalysts and recent trends surrounding Pd

Noble metal-supported catalysts are key materials for purifying various toxic substances. Noble metal catalysts using platinum group elements (ruthenium (Ru), rhodium (Rh), palladium (Pd), osmium (Os), iridium (Ir), and platinum (Pt)) have high performance as oxidation and reduction catalysts. They also have a high melting point and excellent oxidation resistance [8]. These catalysts are widely used for catalytic reactions in various fields such as the chemical industry, energy industry, organic synthesis, purification of automobile exhaust gas, fuel cell electrodes, and others.

Pd has a characteristic electron configuration of $4d^{10}5s^{0}$ and shows excellent catalytic activity in various reactions[9], including chemical catalysts, dental materials, and jewelry. Pd is reported to have higher thermal stability than Pt [10]. Pd also has a high hydrogen storage capacity, absorbing about 935 times its volume of hydrogen [11]. It is also necessary for automobile exhaust gas catalysts (Three-way catalysts). Figure 1-1 shows the price trends of Pd and Pt over the last 15-year period. Before 2017, Pd was less expensive than Pt. Therefore, Pt was replaced by Pd to reduce costs; Pd demand for automotive emission catalysts reached nearly three times the demand for Pt, and the price reversed. Furthermore, Russia, South Africa, and North America account for 44%, 31%, and 15% of Pd production, respectively. The current situation in Russia has caused Pd prices to skyrocket due to concerns about declining supply and demand surge; demand for Pd as a catalyst reaches approximately 90% of global Pd demand. Thus, there is a need to enhance the activity of Pd catalysts to decrease the amount of noble metal needed [11].

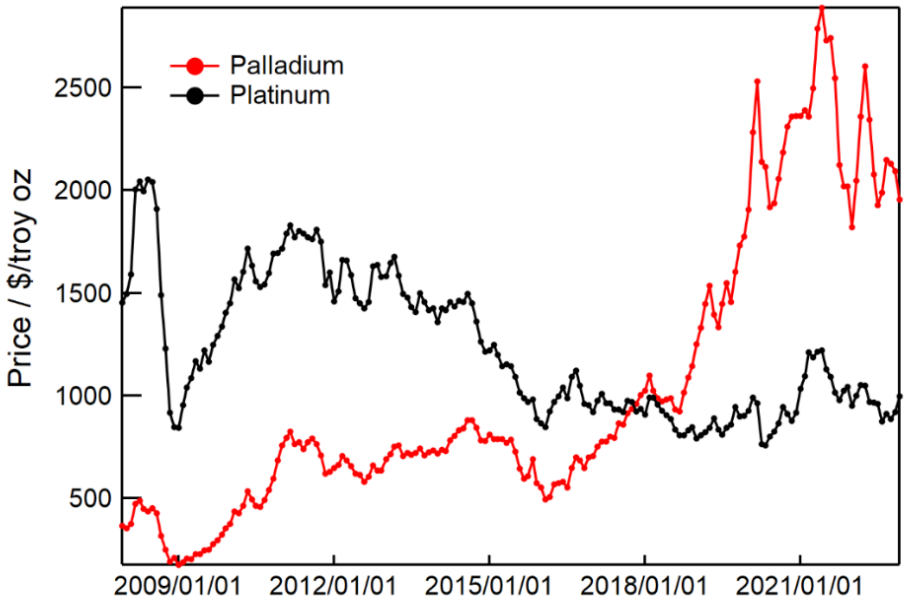

Figure 1-1. Price trends of Pd and Pt over a last 15-year period [12].

1.3.2 Considerations for improving the activity of catalysts

Many studies have been carried out to increase the activity of Pd catalysts. There are various factors that influence the activity of supported catalysts, such as metal dispersion, surface area, metal electronic state, metal surface structure, and metal-support interactions. The following are examples of what should be considered for higher activity of Pd catalysts.

Pd precursor and preparation conditions

Preparation conditions, such as precursor and calcination temperature, and preparation methods change catalytic properties such as dispersibility, particle size, and crystal orientation. Common Pd precursors include chloride ($PdCl_2$), acetylacetonate ($Pd(acac)_2$), nitrate ($Pd(NO_3)_2$). Monteiro et al. found that using different Pd precursors changed the ratio of Pd(100) to Pd(111) on the support, which also affected the catalytic activity [13].

Preparation methods include impregnation, precipitation, and ion exchange. Catalytic activity varies depending on the preparation method, even when the same Pd precursor and support are used [14]. The catalytic properties vary depending on the preparation conditions, even when the same preparation method is used; for example, the activity varies depending on the calcination temperature after loading the metal [15-17]. Therefore, it is essential to establish appropriate Pd precursors and preparation conditions to design more active Pd catalysts.

Selection of appropriate supports

The catalyst support is an essential factor in its activity. Figure 1-2 shows the example of the effect of catalyst support and the role of the catalyst support includes the following.

・The support improves the dispersion of the supported metal and increases its surface area.

・In the case of exothermic reactions, the support prevents the heat of the reaction from being concentrated locally.

・In the case of endothermic reactions, the support provides a source of heat.

・The support provides a place for the adsorption and diffusion of reactants

Interactions between Pd and supports can change the properties of the active site. For example, the oxidation state of Pd can change depending on the support used [18, 24-26]. Numerous papers also reported that the surface area, dispersion, and particle size of the catalyst can change depending on the catalyst support [18-23].

The catalyst support that exhibits high activity differs depending on the catalytic reaction; therefore, selecting appropriate support is essential. For example, Okumura et al. reported that Pd/ZrO_2 is highly active in the toluene combustion reaction [24]. On the other hand, Satsuma et al. reported that Pd/CeO_2 showed high activity in CO oxidation reaction at low temperatures [25]. In the combustion of methane, Pd/θ, α-Al_2O_3 showed higher catalytic activity than Pd/γ-Al_2O_3 [26]. Even for the same Pd catalyst, its catalytic properties vary greatly depending on the support. Consequently, selecting appropriate support is essential to improve the catalytic activity.

Figure 1-2. Example of the effect of catalyst support.

Addition of other elements, alloying

One way to improve the activity of Pd catalysts is the addition of other elements or alloying with other elements. Examples of Pd-bimetallic catalysts are shown in Table 1-2.

The enhancement of activity by adding other elements is mainly caused by the ensemble effect and the ligand effect. The ensemble effect is a specific structure formed by two different metal atoms that affect the catalytic properties. The ligand effect is an effect in which electron transfer occurs between metal atoms with different electronic states, changing the catalytic properties. Several types of bimetallic structures are formed by adding other elements. Typical structures of bimetallic catalysts of metal A and B include a core-shell structure and alloy structure. The core-shell structure is the core surface of metal A covered by a shell of metal B. Alloy structure is formed by a solid solution of metal atoms A and B. On the other hand, even when other elements are added, each element may not form new bonds and remain in a separate state.

Table 1-2. Example of Pd-M bimetallic catalyst.

Pd-M	support	reaction	References
Pd-Au	Al_2O_3, TiO_2	CO oxidation	27
Pd-Au	SiO_2	CO oxidation	28
Pd-Zn	alloy	Adsorption and reaction of ethanol and acetaldehyde	29
Pd-Zn	alloy	CO oxidation	30
Pd-Mo	Al_2O_3	benzene combustion	31
Pd-Mo	Al_2O_3	CH_4 combustion	32
Pd-Mo	Al_2O_3	NO reduction	33
Pd-Cu	CeO_2	Hydrogenation of CO_2	34
Pd-Cu	Al_2O_3	CO oxidation	35
Pd-Cu	CeO_2	water-gas-sift reaction	36

1.4 Catalyst deactivation

The life of a catalyst is one of the most important performances, along with activity and selectivity. Various factors contribute to catalyst inactivity and catalyst degradation. We have to suppress catalyst deactivation in order to design highly active catalysts. Typical examples of causes of catalyst deactivation are listed below.

Sintering

Sintering is the decrease in catalytic activity due to the decrease in the specific surface area of the metal caused by the aggregation of metal components due to heating. When exposed to high temperatures for a long time, particle growth and specific surface area reduction occur due to sintering. The higher the specific surface area, the higher the surface energy of the metal. Therefore, sintering is more likely to occur the larger the particular surface area. Sintering is thermodynamically unavoidable and is a typical cause of catalyst degradation. The resistance of a catalyst to sintering is significantly affected by the reaction temperature and the reaction atmosphere. The stability of metals against sintering in a hydrogen atmosphere corresponds well to the ordinal melting point of metals [2].

Re (3180 °C) > Os (3045 °C) >Ir (2443 °C) > Ru (2250 °C) > Rh (1960 °C)

> Pt (1769 °C) > Co (1495 °C) > Ni (1455 °C) > Fe (1536 °C) > Pd (1552 °C)

>Au (1063 °C) > Cu (1084 °C) > Ag (962 °C)

On the other hand, in an oxygen atmosphere, the tendency for occurring sintering depends on the vapor pressure. In an oxygen atmosphere, sintering is often induced simultaneously with oxide formation. Oxides tend to form in an oxygen atmosphere when the vapor pressure is high. Then, sintering is easily caused under high vapor pressure. The stability against sintering is in the following pecking order.[2]

Rh > Pd > Pt > Ir > Ru > Os

In addition to the melting point and vapor pressure of the metal, the metal-support bond also affects the stability of the sintering. The finer the metal particles, the greater the interaction with the support, which affects sintering behavior. Thus, selecting appropriate support and loading metal particles with appropriate particle sizes are important.

Poisoning

In practical catalytic reactions, there are usually impurities as well as reactants. These impurities can be strongly adsorbed on the catalyst, preventing the reactants from adsorbing to the active site and reducing the catalytic activity. This phenomenon is called catalyst poisoning. Substances that deactivate the catalyst are called catalyst poison. In general, atoms and molecules with non-covalent electron pairs that can participate in binding to the active site tend to be catalyst poison [1]. In metal catalysts, the compounds such as sulfur, selenium, and phosphorus are catalyst poisons. Catalyst poison adsorbs on the active site of the catalyst. The magnitude of the adsorption equilibrium constant determines the degree of poisoning. If the equilibrium constant is large and the poison is irreversibly and strongly adsorbed, permanent poisoning occurs. Heavy metals such as mercury, arsenic, and lead cause permanent poisoning [37]. In addition to heavy metals, sulfur compounds can cause permanent poisoning. Petroleum materials often contain sulfur components as impurities. Sulfur poisoning will be discussed in the next section.

Carbon deposition

The reactant or product hydrocarbons decompose and polymerize, and the carbonaceous material deposited on the catalyst coats the active sites, thereby reducing catalytic activity. Carbon deposition is often observed in hydrocarbon reforming reactions and the Fischer-Tropsch reaction. Generally, the carbon formed on metal catalysts is graphitized; on the other

hand, in the case of acid catalysts, they contain hydrogen and carbon and are often polycyclic aromatics. Methods to prevent deactivation due to carbon deposition include oxidizing the by-product carbon to CO and CO_2, hydrogenating it to CH_4, and reacting it with water vapor to CO + H_2.

1.5 Effect of sulfur compounds on the catalytic properties

Sulfur poisoning is one of the major causes of catalyst activity degradation. The adsorption of sulfur species on the catalyst or the reaction of sulfur species with the catalyst affects its catalytic properties and decreases its activity. There are several mechanisms by which sulfur poisoning can reduce catalytic activity [38]. Examples are listed below and in Figures 1-3.

・Adsorbed sulfur species inhibit adsorption and reaction at multiple sites on the metal surface.

・Strong chemisorption of sulfur species electronically modifies surrounding atoms

→ The ability to adsorb or dissociate reacting molecules is affected.

・Surface restructuring by adsorption of sulfur species

→ The activity is changed for surface-sensitive reaction

・Adsorbed sulfur species inhibit the reaction between adsorbed reactants.

・The adsorbed sulfur species prevent (or retard) the surface diffusion of adsorbed reactants.

・Sulfur species react with the supported metal or support to form inactive sites such as sulfide.

Table 1-3 shows examples of studies on sulfur poisoning of Pd catalysts.

As mentioned above, sulfur compounds generally cause significant deactivation in catalytic reactions. On the other hand, sulfur species can improve catalytic properties. For example, Liu et al. reported that CeO_2 sulfide produced by SO_2 treatment shows higher oxygen storage properties and has a high reduction of nitrogen oxides by ammonia [39]. Hilaire et al. reported that in the Pd/CeO_2 case, the alternating CO and O_2 pulse reactions showed that SO_2 poisoning increased the number of oxygen that could be transferred between the catalyst [40]. In addition, Ortloff et al. revealed that $PdSO_3$, which contributes to the improvement of activity in methane oxidation, was formed as a reaction intermediate by H_2S treatment of Pd/Al_2O_3 [41]. Therefore, understanding detailed knowledge of how sulfur species affect the catalytic structure and catalytic reactions is significant.

The structural change of the Pd catalyst by SO_2 remains fully unexplained. SO_2 is a typical sulfur compound contained in fuels such as gasoline. Pd catalysts are highly reactive with SO_2, forming stable $PdSO_4$. Therefore, SO_2 poisoning of Pd-only catalysts has not been adequately studied compared to Pt and bimetallic catalysts [51]. Furthermore, studies on sulfur poisoning of Pd catalysts have examined catalyst properties under SO_2-containing reaction gas conditions for catalyst performance evaluation; however, the effect of SO_2 itself on the catalyst structure has not been well studied. In order to design catalysts with high sulfur poisoning resistance, a detailed understanding of the effects of SO_2 on the catalyst structure is needed. For example, the adsorption behavior of sulfur species, local structural changes under SO_2 flow, and change at the Pd-support interface.

Table 1-3. Examples of studies on sulfur poisoning of Pd catalysts.

Catalyst	Sulfur species	Reason of deactivation	References
Pd/CeO_2	SO_2	formation of sulfate species	42
Pd/CZ	SO_2	formation of sulfate species	43
$Pd/(SiO_2 + TiO_2)$	SO_2	formation of $PdSO_4$ and sulfate/sulfite species on the support	44
Pd/Al_2O_3	SO_2	formation Brönsted acid sites on Al_2O_3 and hence in inactive $Pd^{\delta+}$ species	45
Pd/Al_2O_3	SO_2	formation of sulfate species	46
Pd/Al_2O_3	SO_2	adsorption of sulfur dioxide: low temperature formation of Pd sulfites or sulphates: high temperature	47
Pd/SiO_2	H_2S	sulfate groups adsorbed onto palladium particles	48
Pd/Al_2O_3	H_2S	strongly adsorbed on the Pd	49
Pd/Al_2O_3	H_2S	formation of sulfide, sulfite and sulfate	50

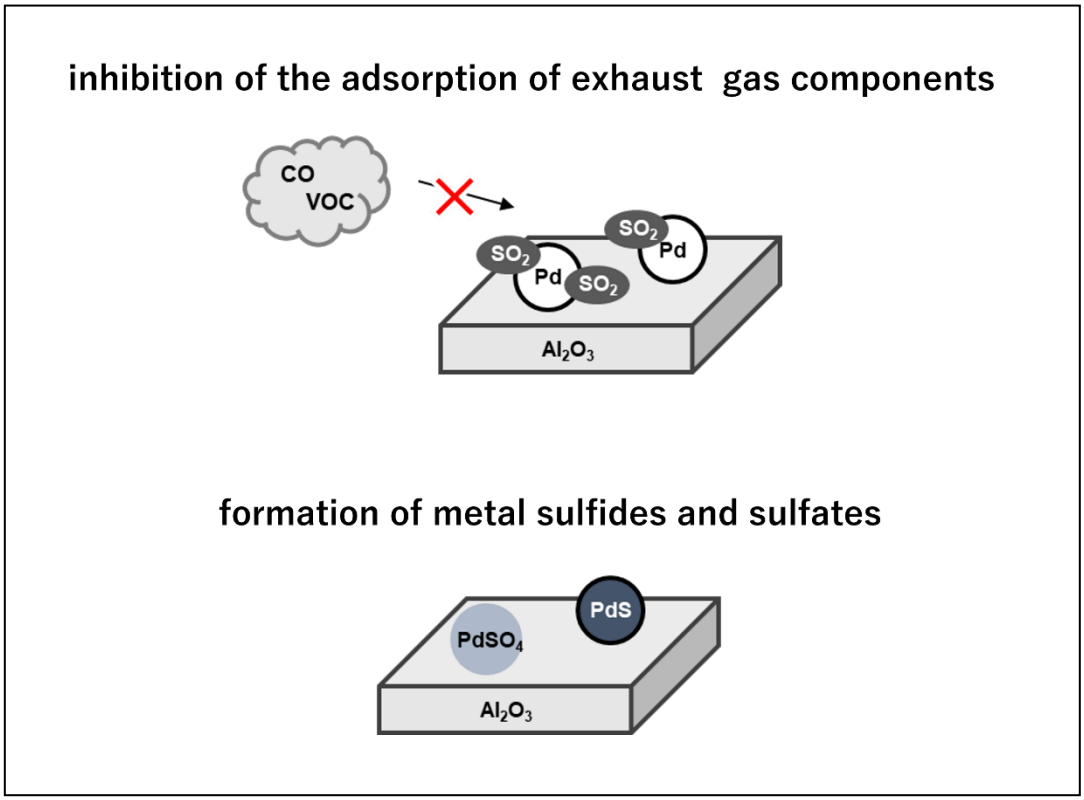

Figure 1-3. Conceptual diagram of sulfur poisoning.

1.6 Research objectives

Pd-supported catalysts are key materials for solving environmental problems such as air pollution. In recent years, emission regulations have been stricter worldwide. Furthermore, the price of Pd has been rising continuously due to the current global situation and increasing demand. Although alternative materials (ex. perovskite oxides) for Pd catalysts have also been investigated, Pd catalysts are still necessary for catalytic reactions at low temperatures. Therefore, it is urgent to reduce the amount of Pd used, that is, to improve the catalytic activity. In addition, the influence of sulfur species present as impurities in the exhaust gas purification reaction is inevitable. The deactivation caused by sulfur poisoning is a severe problem for enhancing catalyst activity and catalyst life. Consequently, a comprehensive understanding of the effects of sulfur species on catalytic properties is needed.

In this study, the effects of catalyst support and transition metal additions are investigated to improve catalytic activity. Furthermore, the effects of sulfur species on catalyst structure and activity are investigated in detail using various spectroscopic techniques to design catalysts with high resistance to sulfur poisoning.

This paper consists of the following 7 chapters. Chapter 1 (this chapter) describes the research background of this study and the fundamentals of catalyst chemistry. Chapter 2 discusses the effect of support on CO oxidation reaction under dilute O_2 conditions. In Chapter 3, the effect of SO_2 on the catalytic structure of Pd/CeO_2 was investigated by *in situ* XAFS measurements to observe the changes under SO_2 flow. In Chapter 4, morphology-controlled c-CeO_2 was prepared, and the effect of SO_2 on the CeO_2 structure of Pd/CeO_2 was analyzed at the atomic level using Scanning Transmission Electron Microscopy(STEM-EELS) measurements. In Chapter 5, the effect of Cu addition on the CO oxidation activity of Pd/CeO_2

catalysts under dilute conditions was investigated. In Chapter 6, the effect of SO_2 on VOC oxidation over Pd/Al_2O_3 is discussed. Finally, chapter 7 summarizes this paper.

References

[1] Kikuchi, E; Segawa, Y; Tadao, A; Imizu, Y; Hattori, H; Atarashii Shokubai Kagaku (New catalyst chemistry), SANKYO SHUPPAN Co.,Ltd., 1997.
(菊池英一, 瀬川幸一, 多田旭男, 射水雄三, 服部英, 新しい触媒化学, 第 2 版, 三共出版, 1997.)

[2] Eguchi, K; Kagaku Masta Kouza Shokubai Kagaku (Catalyst chemistry), Maruzen Publishing Co.,Ltd. 2011.
(江口浩一 編著, 化学マスター講座 触媒化学, 丸善出版, 2011.)

[3] Brundtland GH. Report of the World Commission on environment and development:" our common future.". UN; 1987.

[4] UN General Assembly, Transforming our world : the 2030 Agenda for Sustainable Development, 21 October 2015, https://www.refworld.org/docid/57b6e3e44.html , (accessed 5 December 2022)

[5] Balakrishnan, K.; Bathan, G.; Bose-O'Reilly, S. Pollution and Health: A Progress Update. *The Lancet Planetary* **2022**.

[6] Environmental Restoration and Conservation Agency. Taikiosen no Jouhoukan (Information of air pollution)
(独立行政法人 環境再生保全機構. 大気汚染の情報館),
https://www.erca.go.jp/yobou/taiki , (accessed 5 December 2022)

[7] Japan Society for Atmospheric Environment, Taiki Kankyo no Jiten (Encyclopedia of the Atmospheric Environment), Asakura Publishing Co., Ltd., 2019.
(大気環境学会編. 大気環境の事典, 朝倉書店, 2019.)

[8] Shimizu, S; Muravishi, Y; Etoki Kikinzoku Riyou Gijutu no Kiso (Basics of Precious Metal Utilization Technology), NIKKAN KOGYO SHIMBUN,LTD., 2011.
(清水進, 村岸幸宏.絵とき貴金属利用技術基礎のきそ, 日刊工業新聞社,2011.

[9] Fan, J.; Du, H.; Zhao, Y.; Wang, Q.; Liu, Y.; Li, D.; Feng, J. Recent Progress on Rational Design of Bimetallic Pd Based Catalysts and Their Advanced Catalysis. *ACS Catal.* **2020**, *10* (22), 13560–13583.

[10] Centi, G. Supported Palladium Catalysts in Environmental Catalytic Technologies for Gaseous Emissions. *J. Mol. Catal. A Chem.* **2001**, *173* (1), 287–312.

[11] JOGMEC 金属資源情報,鉱物資源マテリアルフロー2021 5.白金族(PGM), 2021.

[12] Johnson Matthey, PGM management, https://matthey.com/products-and-markets/pgms-and-circularity/pgm-management , (accessed 5 December 2022)

[13] Monteiro, R. S.; Dieguez, L. C.; Schmal, M. The Role of Pd Precursors in the Oxidation of Carbon Monoxide over Pd/Al_2O_3 and $Pd/CeO_2/Al_2O_3$ Catalysts. *Catal. Today* **2001**, *65* (1), 77–89.

[14] Xiao, L.-H.; Sun, K.-P.; Xu, X.-L.; Li, X.-N. Low-Temperature Catalytic Combustion of Methane over Pd/CeO_2 Prepared by Deposition–precipitation Method. *Catal. Commun.* **2005**, *6* (12), 796–801.

[15] Boccuzzi, F.; Chiorino, A.; Manzoli, M.; Lu, P.; Akita, T.; Ichikawa, S.; Haruta, M. Au/TiO_2 Nanosized Samples: A Catalytic, TEM, and FTIR Study of the Effect of Calcination Temperature on the CO Oxidation. *J. Catal.* **2001**, *202* (2), 256–267.

[16] Jung, C. R.; Han, J.; Nam, S. W.; Lim, T.-H.; Hong, S.-A.; Lee, H.-I. Selective Oxidation of CO over $CuO-CeO_2$ Catalyst: Effect of Calcination Temperature. *Catal. Today* **2004**, *93-95*, 183–190.

[17] Tang, X.; Li, Y.; Huang, X.; Xu, Y.; Zhu, H.; Wang, J.; Shen, W. $MnOx–CeO_2$ Mixed Oxide Catalysts for Complete Oxidation of Formaldehyde: Effect of Preparation Method and Calcination Temperature. *Appl. Catal. B* **2006**, *62* (3), 265–273.

[18] Yoshida, H.; Nakajima, T.; Yazawa, Y.; Hattori, T. Support Effect on Methane Combustion over Palladium Catalysts. *Appl. Catal. B* **2007**, *71* (1), 70–79.

[19] Stakheev, A. Y.; Kustov, L. M. Effects of the Support on the Morphology and Electronic Properties of Supported Metal Clusters: Modern Concepts and Progress in 1990s. *Appl. Catal. A* **1999**, *188* (1), 3–35.

[20] Garron, A.; Lázár, K.; Epron, F. Effect of the Support on Tin Distribution in $Pd–Sn/Al_2O_3$ and $Pd–Sn/SiO_2$ Catalysts for Application in Water Denitration. *Appl. Catal. B* **2005**, *59* (1), 57–69.

[21] Comotti, M.; Li, W.-C.; Spliethoff, B.; Schüth, F. Support Effect in High Activity Gold Catalysts for CO Oxidation. *J. Am. Chem. Soc.* **2006**, *128* (3), 917–924.

[22] Zheng, H. T.; Li, Y.; Chen, S.; Shen, P. K. Effect of Support on the Activity of Pd Electrocatalyst for Ethanol Oxidation. *J. Power Sources* **2006**, *163* (1), 371–375

[23] Huang, X.; Yan, H.; Huang, L.; Zhang, X.; Lin, Y.; Li, J.; Xia, Y.; Ma, Y.; Sun, Z.; Wei, S.; Lu, J. Toward Understanding of the Support Effect on Pd1 Single-Atom-Catalyzed Hydrogenation Reactions. *J. Phys. Chem. C* **2019**, *123* (13), 7922–7930.

[24] Okumura, K.; Kobayashi, T.; Tanaka, H.; Niwa, M. Toluene Combustion over Palladium Supported on Various Metal Oxide Supports. *Appl. Catal. B* **2003**, *44* (4), 325–331.

[25] Satsuma, A.; Osaki, K.; Yanagihara, M.; Ohyama, J.; Shimizu, K. Activity Controlling Factors for Low-Temperature Oxidation of CO over Supported Pd Catalysts. *Appl. Catal. B* **2013**, *132-133*, 511–518.

[26] Murata, K.; Mahara, Y.; Ohyama, J.; Yamamoto, Y.; Arai, S.; Satsuma, A. The Metal–Support Interaction Concerning the Particle Size Effect of Pd/Al_2O_3 on Methane Combustion. *Angew. Chem. Int. Ed Engl.* **2017**, *129* (50), 16209–16213.

[27] Ward, T.; Delannoy, L.; Hahn, R.; Kendell, S.; Pursell, C. J.; Louis, C.; Chandler, B. D. Effects of Pd on Catalysis by Au: CO Adsorption, CO Oxidation, and Cyclohexene Hydrogenation by Supported Au and Pd–Au Catalysts. *ACS Catal.* **2013**, *3* (11), 2644–2653.

[28] Xu, J.; White, T.; Li, P.; He, C.; Yu, J.; Yuan, W.; Han, Y.-F. Biphasic Pd-Au Alloy Catalyst for Low-Temperature CO Oxidation. *J. Am. Chem. Soc.* **2010**, *132* (30), 10398–10406.

[29] Jeroro, E.; Vohs, J. M. Exploring the Role of Zn in PdZn Reforming Catalysts: Adsorption and Reaction of Ethanol and Acetaldehyde on Two-Dimensional PdZn Alloys. *J. Phys. Chem. C* **2009**, *113* (4), 1486–1494.

[30] Johnson, R. S.; DeLaRiva, A.; Ashbacher, V.; Halevi, B.; Villanueva, C. J.; Smith, G. K.; Lin, S.; Datye, A. K.; Guo, H. The CO Oxidation Mechanism and Reactivity on PdZn Alloys. *Phys. Chem. Chem. Phys.* **2013**, *15* (20), 7768–7776.

[31] He, Z.; He, Z.; Wang, D.; Bo, Q.; Fan, T.; Jiang, Y. Mo-Modified Pd/Al_2O_3 Catalysts for Benzene Catalytic Combustion. *J. Environ. Sci.* **2014**, *26* (7), 1481–1487.

[32] Konopny, L. W.; Juan, A.; Damiani, D. E. Preparation and Characterization of γ-Al_2O_3-Supported PdMo Catalysts. *Appl. Catal. B* **1998**, *15* (1), 115–127.

[33] de Mello, L. F.; Noronha, F. B.; Schmal, M. NO Reduction with Ethanol on $Pd–Mo/Al_2O_3$ Catalysts. *J. Catal.* **2003**, *220* (2), 358–371.

[34] Choi, E. J.; Lee, Y. H.; Lee, D.-W.; Moon, D.-J.; Lee, K.-Y. Hydrogenation of CO_2 to Methanol over $Pd–Cu/CeO_2$ Catalysts. *Molecular Catalysis* **2017**, *434*, 146–153.

[35] Wang, F.; Zhao, K.; Zhang, H.; Dong, Y.; Wang, T.; He, D. Low Temperature CO Catalytic Oxidation over Supported Pd–Cu Catalysts Calcined at Different Temperatures. *Chem. Eng.*

J. **2014**, *242*, 10–18.F. Wang, K. Zhao, H. Zhang, Y. Dong, T. Wang and D. He, Chem. Eng. J., 2014, 242, 10–18.

[36] Kugai, J.; Fox, E. B.; Song, C. Role of CeO_2 Support for Pd-Cu Bimetallic Catalysts for Oxygen-Enhanced Water Gas Shift. *Appl. Catal. A* **2013**, *456*, 204–214.

[37] Muracami, Y; Saishin Shokubai no Rekkagennin Kaimei to Boushi Taisaku (Elucidation of causes of catalyst degradation and preventive measures), Technical information instirute Co., Ltd., 2006.
(村上雄一. 最新 触媒の劣化原因解明と防止対策, 技術情報協会, 2006.)

[38] Argyle, M. D.; Bartholomew, C. H. Heterogeneous Catalyst Deactivation and Regeneration: A Review. *Catalysts* **2015**, *5* (1), 145–269.

[39] Liu, X.; Wang, P.; Shen, Y.; Bi, S.; Ren, W.; Zhang, D. Boosting SO_2-Tolerant Catalytic Reduction of NOx via Selective Adsorption and Activation of Reactants over Ce^{4+}–SO_4^{2-} Pair Sites. *ACS Catal.* **2022**, *12* (18), 11306–11317.

[40] Hilaire, S.; Sharma, S.; Gorte, R. J.; Vohs, J. M.; Jen, H.-W. Effect of SO_2 on the Oxygen Storage Capacity of Ceria-Based Catalysts. *Catal. Letters* **2000**, *70* (3), 131–135.

[41] Ortloff, F.; Bohnau, J.; Kramar, U.; Graf, F.; Kolb, T. Studies on the Influence of H_2S and SO_2 on the Activity of a PdO/Al_2O_3 Catalyst for Removal of Oxygen by Total Oxidation of (bio-)methane at Very Low O_2:CH_4 Ratios. *Appl. Catal. B* **2016**, *182*, 550–561.

[42] Jeong, H.; Bae, J.; Han, J. W.; Lee, H. Promoting Effects of Hydrothermal Treatment on the Activity and Durability of Pd/CeO_2 Catalysts for CO Oxidation. *ACS Catal.* **2017**, *7* (10), 7097–7105.

[43] Monai, M.; Montini, T.; Melchionna, M.; Duchoň, T.; Kúš, P.; Chen, C.; Tsud, N.; Nasi, L.; Prince, K. C.; Veltruská, K.; Matolín, V.; Khader, M. M.; Gorte, R. J.; Fornasiero, P. The Effect of Sulfur Dioxide on the Activity of Hierarchical Pd-Based Catalysts in Methane Combustion. *Appl. Catal. B* **2017**, *202*, 72–83.

[44] Chenakin, S. P.; Melaet, G.; Szukiewicz, R.; Kruse, N. XPS Study of the Surface Chemical State of a $Pd/(SiO_2+TiO_2)$ Catalyst after Methane Oxidation and SO_2 Treatment. *J. Catal.* **2014**, *312*, 1–11.

[45] Konsolakis; Yentekakis; Pekridis. Insights into the Role of SO_2 and H_2O on the Surface Characteristics and de-N_2O Efficiency of Pd/Al_2O_3 Catalysts during N_2O Decomposition in the Presence of CH_4 and O_2 excess. *Appl. Catal. B* **2013**.

[46] Arosio, F.; Colussi, S.; Groppi, G.; Trovarelli, A. Regeneration of S-Poisoned Pd/Al_2O_3 Catalysts for the Combustion of Methane. *Catal. Today* **2006**, *117* (4), 569–576.

[47] Ordóñez, S.; Hurtado, P.; Díez, F. V. Methane Catalytic Combustion over Pd/Al_2O_3 in Presence of Sulphur Dioxide: Development of a Regeneration Procedure. *Catal. Letters* **2005**, *100* (1), 27–34.

[48] Hoyos, L. J.; Praliaud, H.; Primet, M. Catalytic Combustion of Methane over Palladium Supported on Alumina and Silica in Presence of Hydrogen Sulfide. *Appl. Catal. A* **1993**, *98* (2), 125–138.

[49] Zhao, X.; Chen, B.; Han, L.; Wen, C.; Yu, X.; Chang, L.; Wang, J.; Feng, G.; Liu, J. Density Functional Study on H_2S Adsorption on Pd(111) and Pd/γ-Al_2O_3(110) Surfaces. *Appl. Surf. Sci.* **2017**, *423*, 592–601.

[50] Yu, T.-C.; Shaw, H. The Effect of Sulfur Poisoning on Methane Oxidation over Palladium Supported on γ-Alumina Catalysts. *Appl. Catal. B* **1998**, *18* (1), 105–114.

[51] Yang, W.; Gong, J.; Wang, X.; Bao, Z.; Guo, Y.; Wu, Z. A Review on the Impact of SO_2 on the Oxidation of NO, Hydrocarbons, and CO in Diesel Emission Control Catalysis. *ACS Catal.* **2021**, *11* (20), 12446–12468.

Chapter 2

Effects of catalyst support on CO oxidation reaction under dilute O_2 conditions by Pd catalysts

2.1 Introduction

CO oxidation by O_2 is one of the most fundamental reactions in catalytic chemistry. It has been applied in various industrial and environmental processes, including exhaust gas purification reactions in automobiles and facilities and unburned gas treatment in indoor environments [1]. The emission source of CO changes the reaction conditions. CO concentrations are from below pm to several percent levels, and temperatures are from room temperature to several hundred degrees Celsius. The optimal catalyst composition and preparation process should be selected depending on the CO oxidation reaction conditions. For example, precious metals such as Pt and Pd are commonly used at reaction temperatures above 100 °C, while support Au catalysts and mixed metal oxides such as hopcalite are used at relatively low temperatures [2-8]. In the current energy conversion process, technologies are needed to efficiently react CO with low concentrations of O_2 using waste heat of about100 °C. Developing a catalyst that shows high CO oxidation activity under low O_2 concentration conditions will make it possible to apply in processes that remove harmful CO and low oxygen concentrations.

The properties of the catalyst support have a significant influence on CO oxidation activity in supported Pt and Pd catalysts. In the case of using nonreducing supports such as TiO_2 or Al_2O_3, the active site of CO oxidation is on the precious metal and the metal-support interface [9-11]. The catalytic properties were affected by the size and structure of the metal

nanoparticles and the electronic state of the metal particles due to the interaction between the metal particles and the support [9, 12-13]. On the other hand, in the case of the support itself being highly redox-active, the catalytic properties were also affected by the reactivity of the support. For example, CeO_2, a common support for automotive exhaust gas purification catalysts, has high productivity and oxygen storage capacity, and the lattice oxygen of CeO_2 is involved in the redox reaction. Furthermore, when metals such as Pt and Pd are supported on the CeO_2 surface, the reactivity of the lattice oxygen is significantly enhanced [14-16]. Therefore, in addition to the above factors, it is essential to consider the extent to which Pd activates the lattice oxygen on CeO_2 for CeO_2-supported Pd catalysts.

In this study, I focused on the support effect in CO oxidation under dilute O_2 conditions using Pd catalysts. CO oxidation under excess O_2 conditions using Pd catalysts was reported by Satsuma et al. [19]. Comparing temperatures at 50% CO conversion, light-off temperatures were $Pd/CeO_2 < Pd/TiO_2 < Pd/Al_2O_3 < Pd/ZrO_2 \leq Pd/SiO_2$. TiO_2 and CeO_2 have high oxygen storage properties, which causes their high CO oxidation activity at low temperatures. On the other hand, the factors that cause the difference in activity between Pd/TiO_2 and Pd/CeO_2, the effect of Pd particle size on catalytic activity, and the mechanism of CO oxidation are still under discussion. In addition, catalytic activity varies greatly depending on the reaction gas conditions. Therefore, the catalytic activity is expected to change significantly in the CO oxidation reaction under dilute O_2 conditions. In this study, TiO_2, Al_2O_3, and CeO_2 were used as catalyst supports, and their CO oxidation activities were compared under dilute O_2 conditions. The effects of Pd particle size and Pd oxidation state on the catalytic activity and the CO oxidation reaction mechanism were also investigated.

2.2 Experimental

2.2.1 Catalyst preparation

Supported Pd catalysts (Pd/TiO_2, Pd/Al_2O_3, Pd/CeO_2) were prepared by impregnation methods. Catalyst supports (TiO_2: JRC-TIO-4(2), Al_2O_3: JRC-ALO-8, CeO_2: JRC-CEO-5) were from the Catalysis Society of Japan. $Pd(NH_3)_4(NO_3)_2$ (Sigma-Aldrich Co., Ltd.) was used as Pd precursors for the catalysts. The aqueous precursor solution was dropped into the support powder and dried in a hot water bath. The catalyst samples were dried at 100 °C, calcined at 400 °C for 2 h in the air, and then reduced at 200 °C for 1 h under H_2 flow. The Pd loading was set to 1 wt %.

2.2.2 Catalyst characterization

X-ray diffraction (XRD) patterns were obtained using a RIGAKU RINT 2200 instrument with Cu-Kα radiation at 40 kV and 20 mA. Scanning transmission electron microscopy (STEM) observations and energy dispersive spectroscopy (EDS) elemental mapping were performed using Titan G2 cubed (Gatan). X-ray absorption near edge structure (XANES) and extended X-ray absorption fine structure (EXAFS) spectra were measured at Kyushu Synchrotron Light Research Center (SAGA-LS). EXAFS spectra of the Pd K-edge were obtained in transmission mode. XANES spectra of the Pd L_3-edge were obtained in fluorescence mode. The k^3-weighted EXAFS data were Fourier transformed to r-space over 3.0–13.0 Å. Fourier transform infrared (FTIR) studies were performed with an FTIR-4100 (Jasco) equipped with a diffuse reflectance accessory with KBr windows. Before the measurements, the sample was heated at 300 °C in a He flow. The spectra were collected at 80 °C with a resolution of 4 cm^{-1}.

2.2.3 Catalytic CO oxidation

Catalytic CO oxidation was carried out with a fixed bed flow reactor. Catalyst samples were loaded in a U-shaped glass flow reactor, which was placed in a furnace for catalyst heating. The catalyst amount was 0.030 g. Reaction gases (CO 0.5%, O_2 0.25%, He balance) were fed to the reactor with a flow rate of 100 mL/min. The concentrations of CO_2 and CO were determined using GC-TCD (GC-8A, Shimadzu). Prior to the reaction, the catalyst was heated at 300 °C in a He flow for 1 h. The reaction temperature was set in the range of 90 to 250 °C. For each catalytic reaction, a time course of CO consumption and CO_2 production was obtained at each temperature. CO conversion was measured at steady-state conditions. The carbon balance between CO consumption and CO_2 production was also confirmed in all cases.

2.3 Results and discussion

2.3.1 Structures of Pd particles on the supporting materials

Figure 2-1 shows the XRD patterns of the supported Pd catalysts. For comparison, the patterns of the supporting materials (TiO_2, Al_2O_3, and CeO_2) are shown. The XRD pattern of TiO_2 shows peaks attributed to the anatase structure of TiO_2, Al_2O_3 shows peaks attributed to γ-Al_2O_3, and CeO_2 shows peaks attributed to the fluorite structure of CeO_2. The XRD patterns of the Pd catalysts were almost the same as those of the support, indicating that the structure of the support remained unchanged after Pd deposition and calcination, and H_2 reduction. No diffraction peaks attributed to the Pd or PdO phases were observed in the Pd catalysts, indicating that the Pd species were highly dispersed on the supports.

Pd K-edge XANES spectra of the Pd catalysts and reference samples are shown in Figure 2-2(a). In the XANES spectra of the Pd catalysts, a peak was observed at 24.4 keV, attributed to the transition from the 1s orbital to the 5p orbital. The peak intensity of the spectra depends on the valence of the measured atom. As the Pd valence increased, the intensity of the peak increased. The peak intensity of the Pd catalysts decreased in the order Pd/CeO_2 > Pd/Al_2O_3 > Pd/TiO_2. This finding indicates that the oxidation state of Pd on the CeO_2 was the highest.

XAFS studies on the supported Pd catalysts were performed to investigate the local structures of Pd species. Pd K-edge EXAFS spectra of the supported Pd catalysts are shown in Figure 2-2(b). The spectra of Pd/CeO_2 have peaks at 1.6 Å and 3.0 Å, attributed to the Pd-O and Pd-(O)-Pd bonds, respectively; the peak intensity of Pd-(O)-Pd bond of Pd/CeO_2 is much less than that of PdO, indicating the formation of small-sized PdO on the CeO_2 support on the CeO_2 substrate. Peaks corresponding to Pd-O were observed for Pd/Al_2O_3 and Pd/TiO_2 catalysts, indicating the formation of oxidized Pd on these supported catalysts the same as Pd/CeO_2. On the other hand, a peak at 2.5 Å corresponding to the Pd-Pd bond appeared in the spectra of the Pd/Al_2O_3 and

Pd/TiO_2 catalysts, indicating that reduced Pd species are also formed on these catalysts. This revealed that Pd on TiO_2 and Al_2O_3 was more easily reduced than on CeO_2.

Figure 2-3 shows the Pd L_3-edge XANES spectra of the supported Pd catalyst together with the reference sample; the Pd catalyst spectrum shows a peak at 3174.4 eV, which is attributed to the transition from the 2p to 4d orbitals. Thus, the Pd L_3-edge XANES spectra strongly depend on the oxidation state of Pd on the support [17, 18]. The peak intensity of Pd/TiO_2 is smaller than that of Pd/Al_2O_3 and Pd/CeO_2, indicating that Pd on TiO_2 is reduced more than on Al_2O_3 and CeO_2. These EXAFS studies agreed with the Pd K-edge EXAFS spectra.

STEM-EDS images of Pd catalysts are shown in Figures 2-4. Pd/TiO_2 and Pd/Al_2O_3 images show nanoparticles with strong brightness contrast corresponding to Pd particles. For both Pd/TiO_2 and Pd/Al_2O_3 catalysts, the Pd particle size is around 2-5 nm. This result agreed with the XRD results, which indicate that Pd is highly dispersed. The contrast difference in the STEM-HAADF image of Pd/CeO_2 is small due to the close atomic number of Pd and Ce atoms. Therefore, Pd particles could not be detected in EDS mapping. The results of Pd elemental mapping showed that Pd particles in Pd/CeO_2 were highly dispersed less than 2 nm.

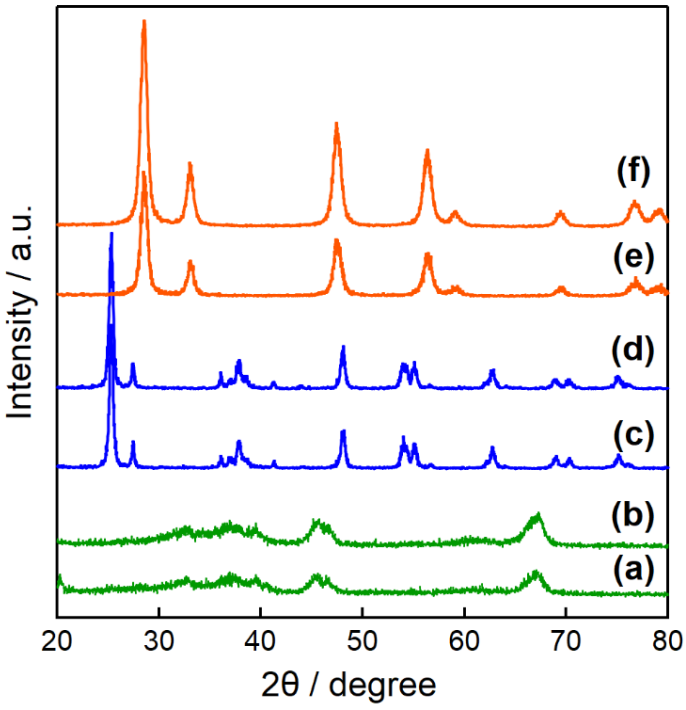

Figure 2-1. XRD patters of supports and Pd catalysts (a)Al_2O_3; (b)Pd/Al_2O_3; (c)TiO_2; (d)Pd/TO_2; (e)CeO_2; (f)Pd/CeO_2.

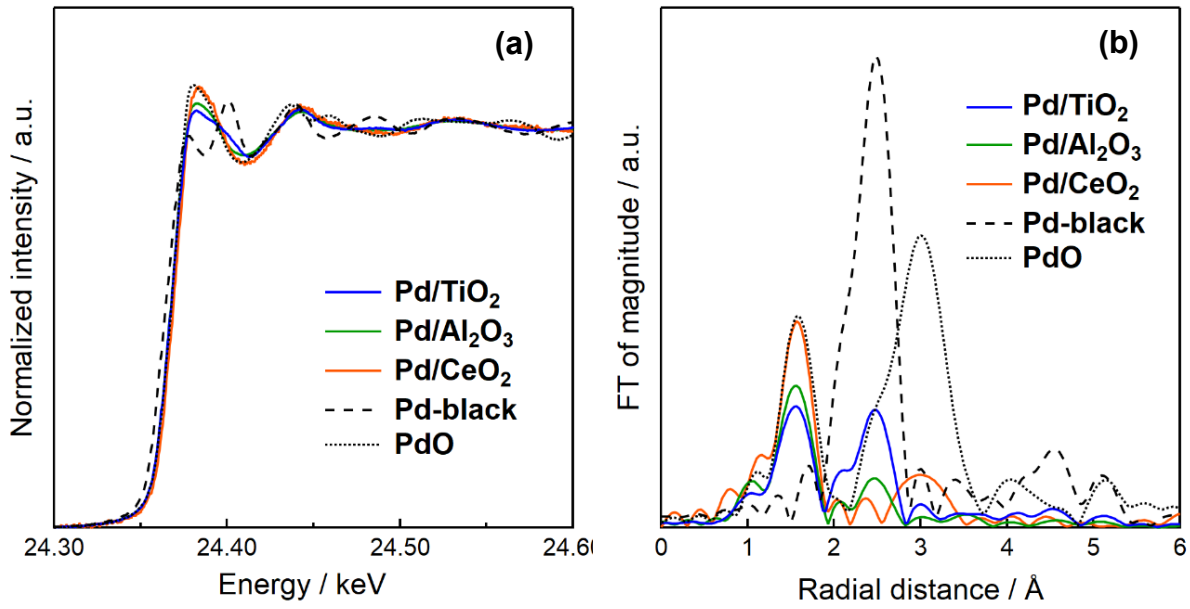

Figure 2-2. Pd K-edge (a)XANES spectra and (b)EXAFS spectra of Pd catalysts and references.

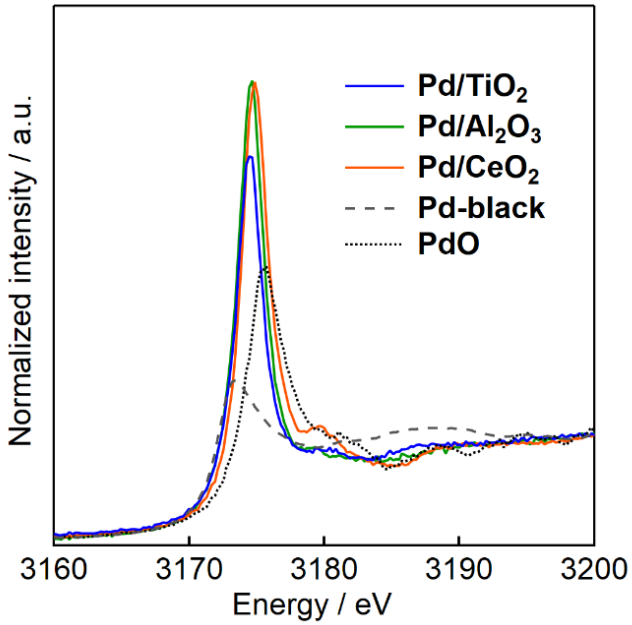

Figure 2-3. Pd L_3-edge XANES spectra of Pd catalysts and references.

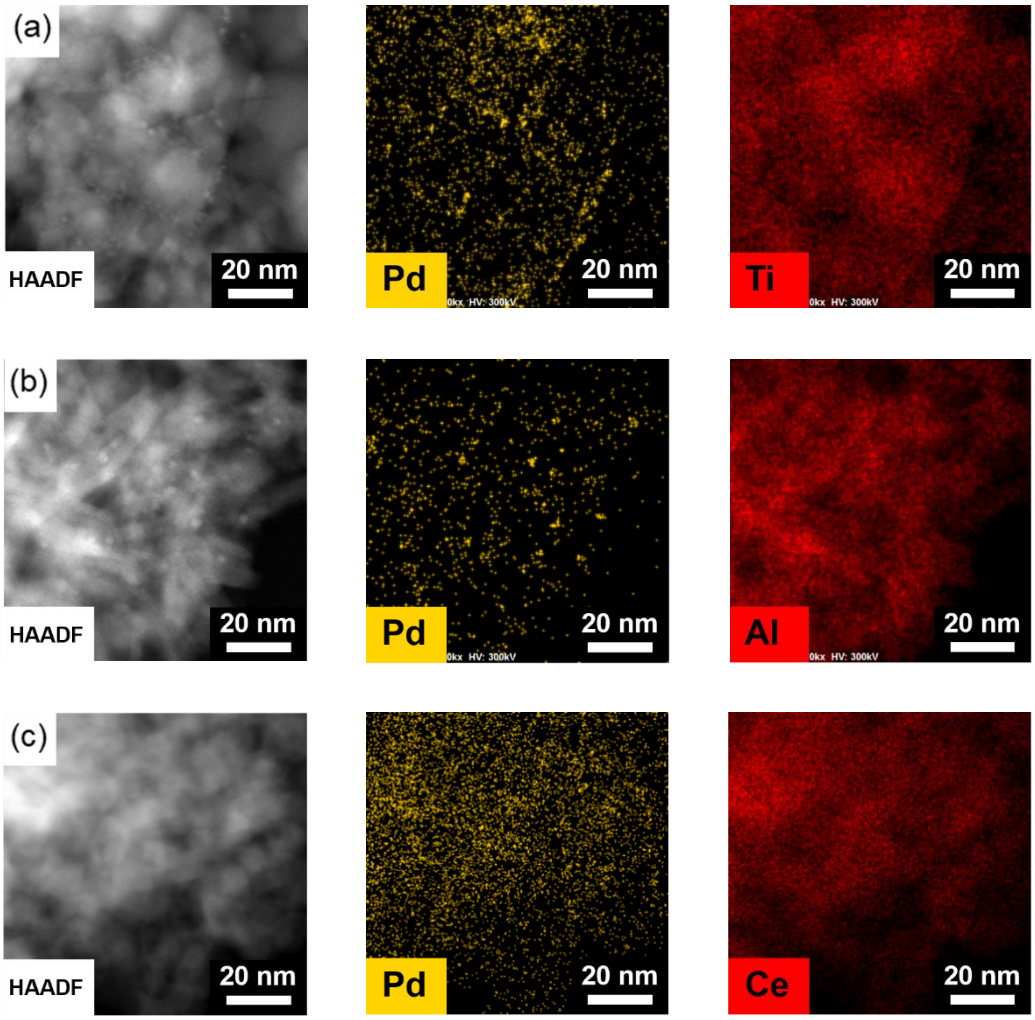

Figure 2-4. STEM-EDS images of (a)Pd/TiO_2 (b)Pd/Al_2O_3 (c)Pd/CeO_2.

2.3.2 Catalytic CO oxidation

CO oxidation activity of the supported Pd catalysts under dilute oxygen conditions is shown in Figure 2-5. CO oxidation activity of Pd/CeO_2 showed in the temperature range above 90 °C. The light-off temperatures of Pd/Al_2O_3 and Pd/TiO_2 were 150 °C and 120 °C, respectively. CO conversion increased with increasing temperature for all catalysts, but the temperature dependence of the CO conversion varied significantly depending on the type of substrate. The activity of Pd/CeO_2 increased gradually, while the activity of Pd/TiO_2 and Pd/Al_2O_3 increased rapidly above 210 °C. in addition, Pd/Al_2O_3 and Pd/ TiO_2 showed higher CO oxidation activity than that of Pd/CeO_2. In addition, unlike previous studies under oxygen-rich conditions [19], a distinct difference in activity between Pd/CeO_2 and Pd/TiO_2 was observed.

The redox properties of catalyst support strongly affect the temperature dependence of CO oxidation activity. For example, the lattice oxygen of CeO_2 contributes to CO oxidation at low temperatures in the case of Pd/CeO_2. Furthermore, the CeO_2 support enhances the oxidation of Pd to PdO. Satsuma et al. revealed that the Light-off temperature of Pd/CeO_2 is lower than that of other oxide support catalysts in the CO oxidation reaction under high concentrations of O_2 [19]. The reduction of PdO to Pd, the reactivity of the lattice oxygen of the CeO_2 support, and oxygen release and storage properties contribute to the activity in the CO oxidation reaction.

In this research, Pd/CeO_2 also showed higher CO oxidation activity under low temperatures and dilute oxygen conditions. In the case of Pd/Al_2O_3 and Pd/TiO_2, the catalyst supports were not strong reductants. Therefore, the lattice oxygen of the support did not contribute to the reaction. In these catalysts, CO oxidation proceeded by the Langmuir-Hinshelwood-type or Mars-van Krevelen mechanism. Langmuir-Hinshelwood-type mechanism related to the molecular oxygen in the air is dissociated and adsorbed. Mars-van Krevelen mechanism based on the redox behavior of Pd. Pd is covered with CO at low reaction temperatures, which inhibits

the dissociative adsorption of oxygen on the metal or the reoxidation of Pd. Therefore, CO oxidation is less likely to proceed under low-temperature conditions, while CO oxidation proceeds rapidly under high-temperature conditions where CO desorption is more likely to occur.

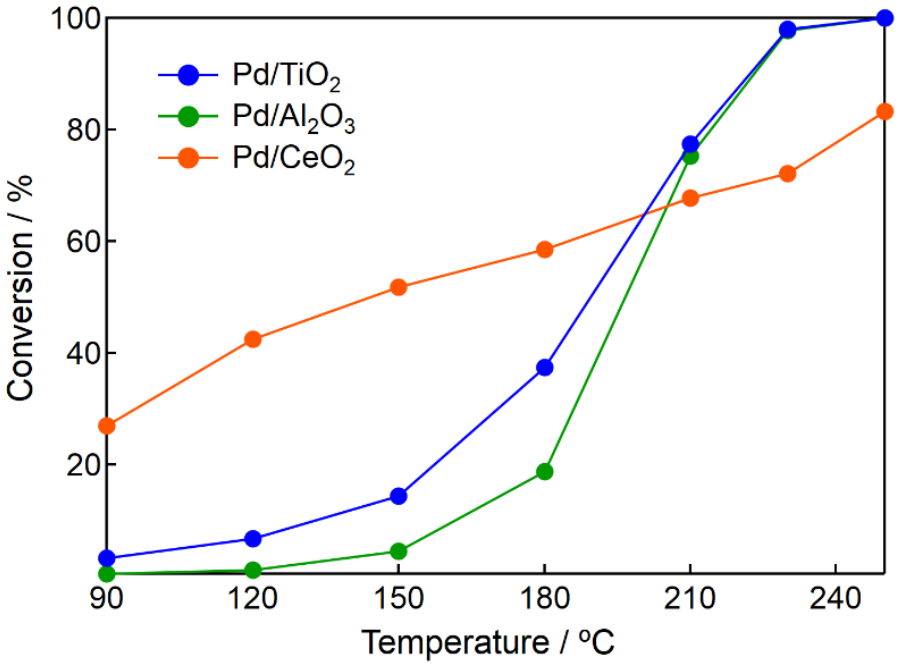

Figure2-5. Catalytic CO oxidation with Pd catalysts under dilute O_2 condition.

3.3 Diffuse reflectance FTIR studies

FTIR spectra of CO species adsorbed on the supported Pd catalysts are shown in Figure 2-6. The FTIR spectra provided information on the reactivity of CO chemisorbed on the Pd sites. The spectra were measured under CO-N_2 flow, and then the gas was changed to CO-O_2-N_2. The spectra of the catalysts showed peaks of CO linearly coordinated on Pd at approximately 2100 cm^{-1} and peaks of CO bridged coordinated at approximately 1960 cm^{-1}. The peaks at approximately 2110 cm^{-1} are attributed to CO species linearly coordinated on Pd^{2+} or Pd^{+} [20-25]. Peaks of CO species adsorbed on Pd^0 were detected in the spectrum of Pd/CeO_2 under CO gas flow. On the other hand, XAFS spectra showed that Pd was oxidized to PdO on CeO_2 in the air, as described above. These results indicate that in Pd/CeO_2, Pd was oxidized to PdO in the air, and then PdO was quickly reduced to Pd^0 under CO flow. From these results, the reduction and reoxidation of PdO are rapidly promoted under these reaction conditions. FTIR spectra of Pd/Al_2O_3 and Pd/TiO_2 under CO gas flow showed peaks attributed to CO species adsorbed on Pd^0. Especially Pd on Al_2O_3 was oxidized to PdO in the air same as Pd/CeO_2, indicating that Pd/Al_2O_3 is also highly reducible from PdO to Pd.

In the Pd/CeO_2, the peak intensity of linearly coordinated CO on Pd^0 was higher than bridge coordinated CO on Pd^0. On the other hand, in the spectra of Pd/TiO_2 and Pd/Al_2O_3, bridge-coordinated CO was the main peak. This result indicates that Pd is more highly dispersed on CeO_2 than on Al_2O_3 and TiO_2 and agreed with STEM-EDS images.

FTIR spectra of Pd/CeO_2 and other supported Pd catalysts under CO oxidation reaction gases showed important differences. The FTIR spectra of Pd/CeO_2 revealed that the peak intensity of adsorbed CO species under CO-O_2-N_2 flow was significantly lower than under CO-N_2 flow. This decrease in peak intensity is attributed to the oxidative desorption of CO adsorbed on Pd in reaction with O_2. For Pd/TiO_2 and Pd/Al_2O_3, the decrease in peak intensity under CO-O_2-N_2 flow was smaller than that of Pd/CeO_2. This result indicates that CO species adsorbed on Pd on

CeO_2 desorbed more readily than CO species on Pd on TiO_2 or Al_2O_3 substrates. This may be because CO species linearly adsorbed on Pd are less stable and more easily desorbed than cross-linked CO species or/and because the lattice oxygen of CeO_2 is more reactive. PdO reduction at the Pd site and oxidative desorption of CO species are important steps in CO oxidation on supported Pd catalysts. Therefore, these catalytic properties of Pd/CeO_2 are the factor contributing to the high activity in the catalytic CO oxidation.

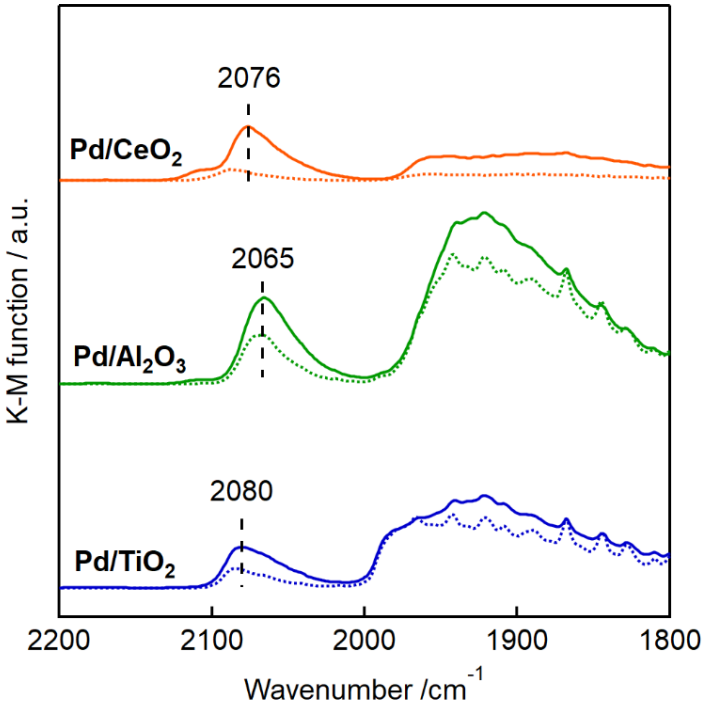

Figure 2-6. FTIR spectra of Pd catalysts.
solid line: 1% CO-He(balance); dotted line: 0.5% CO-0.25% O_2- He(balance).

2.4 Conclusion

In this chapter, the effect of the support on CO oxidation reaction under dilute O_2 conditions was discussed. The catalytic activity of Pd/CeO_2 was higher than that of Pd/TiO_2 and Pd/Al_2O_3 in CO oxidation at low temperatures below 180 °C. XAFS and FTIR measurements revealed that Pd on CeO_2 exists as PdO at room temperature and in air and is easily reduced to Pd^0 under CO flow. The STEM-EDS images and FTIR measurements showed that the Pd particles on CeO_2 were smaller and more highly dispersed than those on TiO_2 and Al_2O_3. FTIR studies revealed that the oxidative desorption of CO species adsorbed on Pd/CeO_2 was faster than that on Pd/TiO_2 and Pd/Al_2O_3 at low temperatures. CO oxidation under dilute O_2 condition of Pd/CeO_2 follows the Mars-van Krevelen mechanism in Figure 2-7. Therefore, the reasons Pd/CeO_2 shows higher low-temperature activity than Pd/TiO_2 or Pd/Al_2O_3 are (1) Pd particles are small and highly dispersed, (2) Oxidation and reduction of Pd on CeO_2 easily occur (3) oxidative desorption of CO is faster.

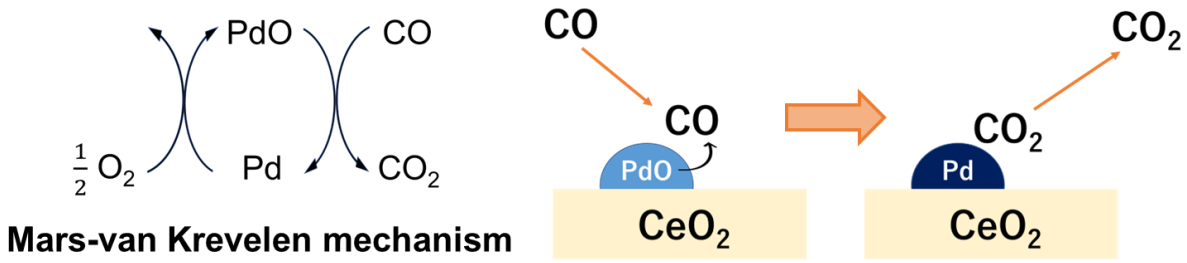

Figure 2-7. Reaction mechanism of CO oxidation on Pd/CeO_2.

References

[1] Zhou, Y.; Wang, Z.; Liu, C. Perspective on CO Oxidation over Pd-Based Catalysts. *Catalysis Science & Technology* **2015**, *5* (1), 69–81.

[2] Berlowitz, P. J.; Peden, C. H. F.; Goodman, D. W. Kinetics of Carbon Monoxide Oxidation on Single-Crystal Palladium, Platinum, and Iridium. *J. Phys. Chem.* **1988**, *92* (18), 5213–5221.

[3] Chen, M. S.; Cai, Y.; Yan, Z.; Gath, K. K.; Axnanda, S.; Goodman, D. W. Highly Active Surfaces for CO Oxidation on Rh, Pd, and Pt. *Surf. Sci.* **2007**, *601* (23), 5326–5331.

[4] Haruta, M.; Yamada, N.; Kobayashi, T.; Iijima, S. Gold Catalysts Prepared by Coprecipitation for Low-Temperature Oxidation of Hydrogen and of Carbon Monoxide. *J. Catal.* **1989**, *115* (2), 301–309.

[5] Kung, H. H.; Kung, M. C.; Costello, C. K. Supported Au Catalysts for Low Temperature CO Oxidation. *J. Catal.* **2003**, *216* (1), 425–432.

[6] Bansmann, J.; Abdel-Mageed, A. M.; Chen, S.; Fauth, C.; Häring, T.; Kučerová, G.; Wang, Y.; Behm, R. J. Chemical and Electronic Changes of the CeO_2 Support during CO Oxidation on Au/CeO_2 Catalysts: Time-Resolved Operando XAS at the Ce LIII Edge. *Catalysts* **2019**, *9* (10), 785.

[7] Dey, S.; Chandra Dhal, G.; Mohan, D.; Prasad, R. Synthesis of Silver Promoted CuMnOx Catalyst for Ambient Temperature Oxidation of Carbon Monoxide. *Journal of Science: Advanced Materials and Devices* **2019**, *4* (1), 47–56.

[8] Jones, C.; Cole, K. J.; Taylor, S. H.; Crudace, M. J.; Hutchings, G. J. Copper Manganese Oxide Catalysts for Ambient Temperature Carbon Monoxide Oxidation: Effect of Calcination on Activity. *J. Mol. Catal. A Chem.* **2009**, *305* (1), 121–124.

[9] Li, N.; Chen, Q.-Y.; Luo, L.-F.; Huang, W.-X.; Luo, M.-F.; Hu, G.-S.; Lu, J.-Q. Kinetic Study and the Effect of Particle Size on Low Temperature CO Oxidation over Pt/TiO_2 Catalysts. *Appl. Catal. B* **2013**, *142-143*, 523–532.

[10] Carlsson, P.-A.; Österlund, L.; Thormählen, P.; Palmqvist, A.; Fridell, E.; Jansson, J.; Skoglundh, M. A Transient in situ FTIR and XANES Study of CO Oxidation over Pt/Al_2O_3 Catalysts. *J. Catal.* **2004**, *226* (2), 422–434.

[11] Haneda, M.; Todo, M.; Nakamura, Y.; Hattori, M. Effect of Pd Dispersion on the Catalytic Activity of Pd/Al_2O_3 for C3H6 and CO Oxidation. *Catal. Today* **2017**, *281*, 447–453.

[12] Cuenya, B. R. Synthesis and Catalytic Properties of Metal Nanoparticles: Size, Shape, Support, Composition, and Oxidation State Effects. *Thin Solid Films* **2010**, *518* (12), 3127–3150.

[13] van Deelen, T. W.; Hernández Mejía, C.; de Jong, K. P. Control of Metal-Support Interactions in Heterogeneous Catalysts to Enhance Activity and Selectivity. *Nature Catalysis* **2019**, *2* (11), 955–970.

[14] Zhu, H.; Qin, Z.; Shan, W.; Shen, W.; Wang, J. Low-Temperature Oxidation of CO over Pd/CeO_2–TiO_2 Catalysts with Different Pretreatments. *J. Catal.* **2005**, *233* (1), 41–50.

[15] Liu, B.; Zhao, Z.; Henkelman, G.; Song, W. Computational Design of a CeO_2-Supported Pd-Based Bimetallic Nanorod for CO Oxidation. *J. Phys. Chem. C* **2016**, *120* (10), 5557–5564.

[16] Nie, L.; Mei, D.; Xiong, H.; Peng, B.; Ren, Z.; Hernandez, X. I. P.; DeLaRiva, A.; Wang, M.; Engelhard, M. H.; Kovarik, L.; Datye, A. K.; Wang, Y. Activation of Surface Lattice Oxygen in Single-Atom Pt/CeO_2 for Low-Temperature CO Oxidation. *Science* **2017**, *358* (6369), 1419–1423.

[17] Tew, M. W.; Miller, J. T.; van Bokhoven, J. A. Particle Size Effect of Hydride Formation and Surface Hydrogen Adsorption of Nanosized Palladium Catalysts: L_3 Edge vs K Edge X-Ray Absorption Spectroscopy. *J. Phys. Chem. C* **2009**, *113* (34), 15140–15147.

[18] Shimizu, K.-I.; Kamiya, Y.; Osaki, K.; Yoshida, H.; Satsuma, A. The Average Pd Oxidation State in Pd/SiO_2 Quantified by L_3 -Edge XANES Analysis and Its Effects on Catalytic Activity for CO Oxidation. *Catalysis Science & Technology* **2012**, *2* (4), 767–772.

[19] Satsuma, A.; Osaki, K.; Yanagihara, M.; Ohyama, J.; Shimizu, K. Activity Controlling Factors for Low-Temperature Oxidation of CO over Supported Pd Catalysts. *Appl. Catal. B* **2013**, *132-133*, 511–518.

[20] Shen, Y.; Lu, G.; Guo, Y.; Wang, Y.; Guo, Y.; Gong, X. Study on the Catalytic Reaction Mechanism of Low Temperature Oxidation of CO over Pd–Cu–Clx/Al_2O_3 Catalyst. *Catal. Today* **2011**, *175* (1), 558–567.

[21] Ortega, A.; Huffman, F. M.; Bradshaw, A. M. The Adsorption of CO on Pd (100) Studied by IR Reflection Absorption Spectroscopy. *Surf. Sci.* **1982**.

[22] Zeinalipour-Yazdi, C. D.; Willock, D. J.; Thomas, L.; Wilson, K.; Lee, A. F. CO Adsorption over Pd Nanoparticles: A General Framework for IR Simulations on Nanoparticles. *Surf. Sci.* **2016**, *646*, 210–220.

[23] Ryczkowski, J. IR Spectroscopy in Catalysis. *Catal. Today* **2001**, *68*, 263–381.

[24] Mondelli, C.; Ferri, D.; Grunwaldt, J.-D.; Krumeich, F.; Mangold, S.; Psaro, R.; Baiker, A. Combined Liquid-Phase ATR-IR and XAS Study of the Bi-Promotion in the Aerobic Oxidation of Benzyl Alcohol over Pd/Al_2O_3. *J. Catal.* **2007**, *252* (1), 77–87.

[25] Busca, G.; Finocchio, E.; Escribano, V. S. Infrared Studies of CO Oxidation by Oxygen and by Water over Pt/Al_2O_3 and Pd/Al_2O_3 Catalysts. *Appl. Catal. B* **2012**, *113-114*, 172–179.

Chapter 3

in situ XAFS studies for Sulfurization of CeO_2 by SO_2

3.1 Introduction

Pd catalysts are a key material for purifying exhaust gas from factories and vehicles [1-4]. These gases contain air pollutants and harmful compounds such as NOx, CO, and hydrocarbons. The regulations on these compounds are becoming increasingly stringent worldwide to achieve a sustainable society. Generally, platinum group metal catalysts oxidize/reduce harmful compounds to non-toxic substances. There is a strong need to reduce the amount of platinum group metals used because they are scarce and expensive. Therefore, the activity of the PGM catalyst is required to improve. It has been reported that Pd has better thermal durability than Pt [1,5-7]. Various oxides such as Al_2O_3, SiO_2, and TiO_2 have been used as supports for Pd catalysts. CeO_2 has excellent redox properties and improves CO oxidation activity at low temperatures when used as a supporting material for Pd catalysts. Therefore, CeO_2-supported Pd catalysts (Pd/CeO_2) are frequently used as catalysts for oxidation.

Catalyst poisoning by sulfur-containing substances (e.g., SO_2 and H_2S) is an important issue in exhaust gas purification. The catalytic performance of Pd catalysts seriously deteriorates after sulfur poisoning [8-12]. Since SO_2 is contained in emissions from many stationary and mobile sources, it is necessary to develop Pd catalysts that exhibit high activity and resistance to sulfur poisoning. Understanding the mechanism for sulfur poisoning is essential for designing sulfur-tolerant catalysts.

It has been reported that treatment of supported Pd catalysts with SO_2 generally reduces the activity of Pd catalysts due to the formation of palladium sulfide and a decrease in the catalyst

surface area [11, 13-16]. However, the effect of SO_2 on the catalyst structure has not yet been fully investigated. The effect of SO_2 treatment on the properties of CeO_2 has already been investigated. When CeO_2 is sulfurized, oxygen defects are introduced, reducing Ce^{4+} to Ce^{3+} [17-19]. The sulfurized CeO_2 produced by the SO_2 treatment has exhibited oxygen storage properties and high activity in the reduction of nitrogen oxides by ammonia [20]. The activities of Pd/CeO_2 deteriorated in the presence of SO_2. On the other hand, Hilaire et al. reported that in the case of Pd/CeO_2, pulse reactions with alternating CO and O_2 pulses showed that SO_2 poisoning increased the amount of oxygen that could be transferred to and from the catalyst over the entire temperature range that was examined [21]. These results prompted us to investigate the poisoning behavior of CeO_2-supported Pd catalysts by SO_2, which would affect the catalytic activities of the Pd/CeO_2 catalysts.

In this study, *in situ* XAFS measurements under SO_2 gas flow were mainly carried out to investigate the structure change of CeO_2-supported Pd catalyst by sulfur poisoning. The Ce L_3-edge and Pd L_3-edge XAFS studies can clarify the local structure of the Pd and Ce sites in the Pd/CeO_2 catalyst under reaction conditions. The XAFS studies also allowed us to analyze the oxidation state of the Ce site quantitatively and revealed the pathways for the sulfurization of CeO_2 and the role of Pd in these reactions. We also performed the *in situ* S K-edge XAFS measurements to investigate the formation behavior of sulfate species on the Pd/CeO_2 catalysts. The structure of sulfurized Pd/CeO_2 was also analyzed based on XRD, STEM-EDS, and XPS analyses, and the applicability of the catalyst to oxidation reactions is discussed.

3.2 Experimental

3.2.1 Catalyst preparation

Pd/CeO_2 catalysts were prepared by an impregnation method. CeO_2 (JRC-CEO-5, Catalysis Society of Japan) was used as catalyst support. The aqueous solution containing $Pd(NH_3)_4(NO_3)_2$ (Sigma-Aldrich Japan) was dropped into the CeO_2 powders. Then the sample was well mixed and dried. Subsequently, the precursor hydroxides were dried at 100 °C overnight, calcined at 400 °C for 2 h, and then reduced in H_2 flow at 200 °C for 1 h. The Pd loading was set to 1 wt%.

3.2.2 Catalyst characterization

The X-ray diffraction (XRD) patterns were obtained at 40 kV and 20 mA (the step rate was 2°/min) by using a RINT 2200 diffractometer (RIGAKU, Japan) with Cu-Kα radiation (1.54 Å). Temperature-programmed reduction with H_2 (H_2-TPR) was performed using BEL-CAT (Microtrac BEL). The sample (0.10 g) was pretreated in an air flow at 350 °C for 1 h. Catalyst samples were heated from 50 °C to 950 °C at the rate of 5 °C/min. X-ray photoelectron spectroscopy studies were performed using a Kratos ESCA-3400 spectrometer (XPS, AXIS-165, KRATOS, Japan) with an Al K source. X-ray fluorescence (XRF) spectra were obtained using a ZSX PrimusIV/RX9 (Rigaku).

3.2.3 XAFS measurement

XAFS measurements were performed at Kyushu Synchrotron Light Research Center (SAGA-LS) beamline BL06 (Saga, Japan). The storage ring energy was 1.4 GeV. The double crystal monochromator Si(111) was used. Ce L_3-edge spectra were obtained with a transmission

mode, and S K-edge and Pd L_3-edge spectra were obtained with a fluorescence mode. For the *in situ* measurement, the catalyst and boron nitride were weighed in the required amount, mixed well with a mortar, and formed into 10 mmφ disks. The *in situ* measurements were performed using a glass cell (Figure 3-1). The catalysts were heated at a reaction temperature under 500 ppm SO_2 flow (100 mL/min) and then measured at room temperature. After that, the catalysts were reoxidized with O_2 at 500 °C and measured as same. The measurements were also performed at 200 °C and 400 °C under the same conditions. XAFS analyses were carried out using Athena [22].

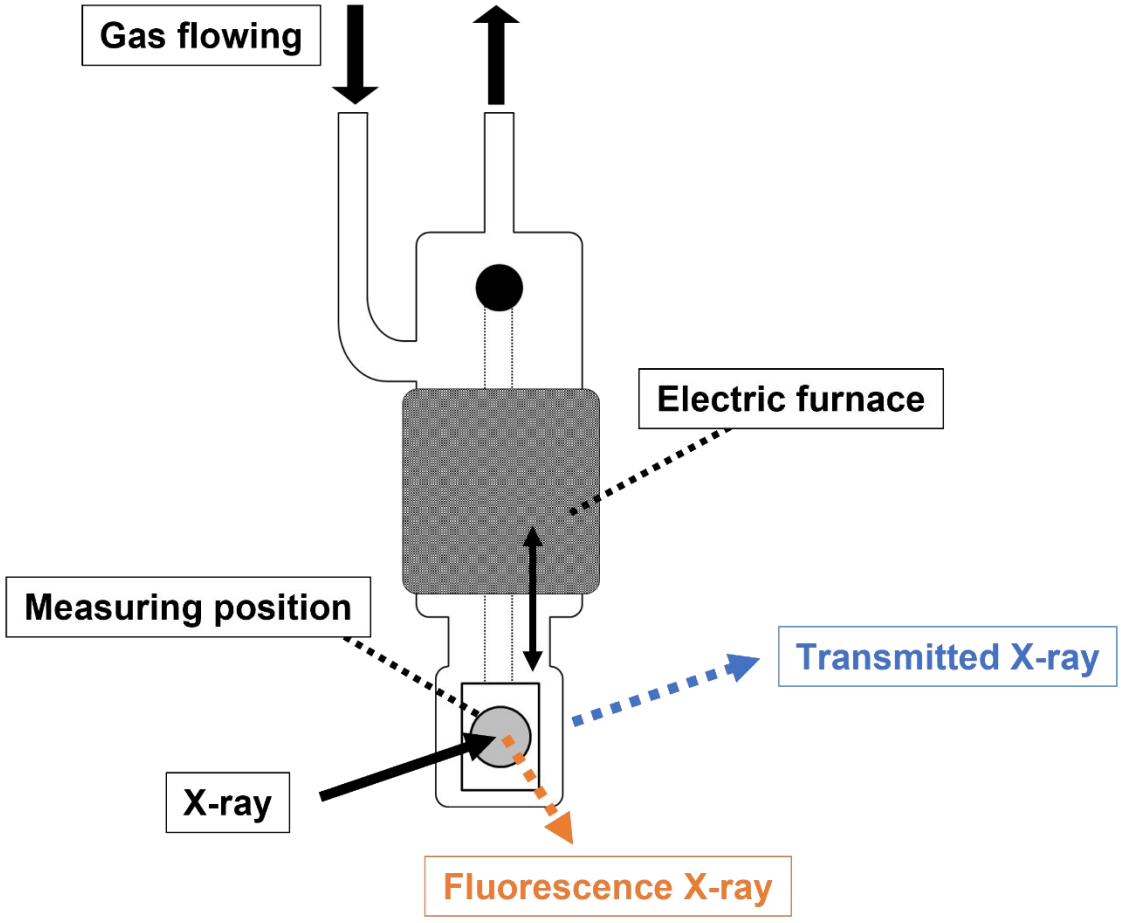

Figure 3-1. Image of a glass cell of *in situ* measurements.

3.3 Results and discussion

3.3.1 Catalyst characterization

XRD analyses were performed to investigate changes in crystal structure after the SO_2 treatment. Figure 3-2 shows XRD patterns of fresh Pd/CeO_2 and SO_2-treated Pd/CeO_2. For the fresh Pd/CeO_2 sample, the peaks were observed at 2θ = 28, 33, 47, 56, 59, 69, 76, 79, 88, and 95°. These peaks are attributed to the pattern of the fluorite structure of CeO_2 [26]. Pd metal and Pd oxide phases were not detected, implying that Pd species were highly dispersed on the CeO_2 support. The peak intensities of SO_2-treated catalysts were lower than those of the fresh sample, whereas the peak positions remained unchanged, and no new peak was detected. These findings mean that Pd/CeO_2 maintained the fluorite structure after the SO_2 treatment, although the fraction of the fluorite phase was reduced.

Pd/CeO_2 samples before and after SO_2 treatment at 500 °C were observed by TEM and STEM-EDS. HR-TEM images and STEM-EDS mapping of Pd/CeO_2 showed that the particle size of Pd in the fresh sample was about 3 nm, and Pd particles were highly dispersed on CeO_2 (Figure 3-3). No Pd particles larger than 30 nm were observed. These results are consistent with the XRD results, in which no X-ray diffraction lines were observed for Pd and PdO. STEM-EDS mapping also revealed that the Pd particle size was 2-4 nm, and the particle size did not change after the SO_2 treatment (Figure 3-4). Sulfur species were detected on the entire catalyst surface, indicating that the entire CeO_2 surface was sulfurized.

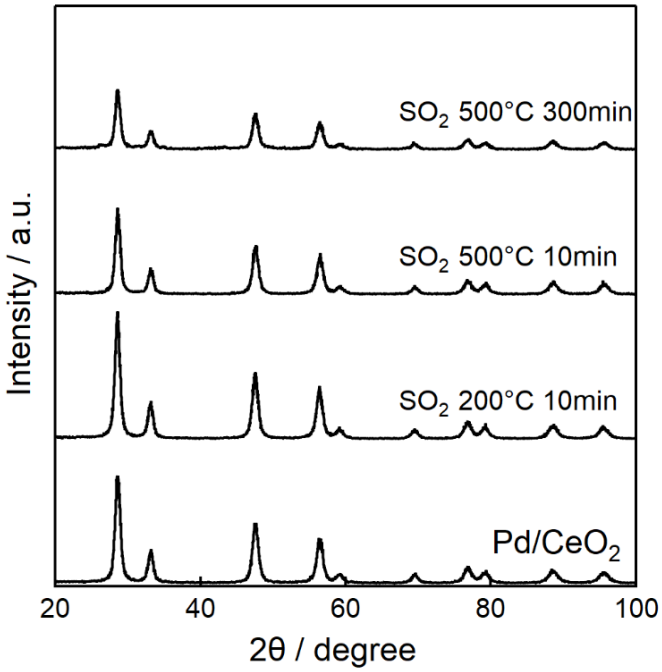

Figure 3-2. XRD patterns of fresh Pd/CeO_2 and Pd/CeO_2 after SO_2 flow.

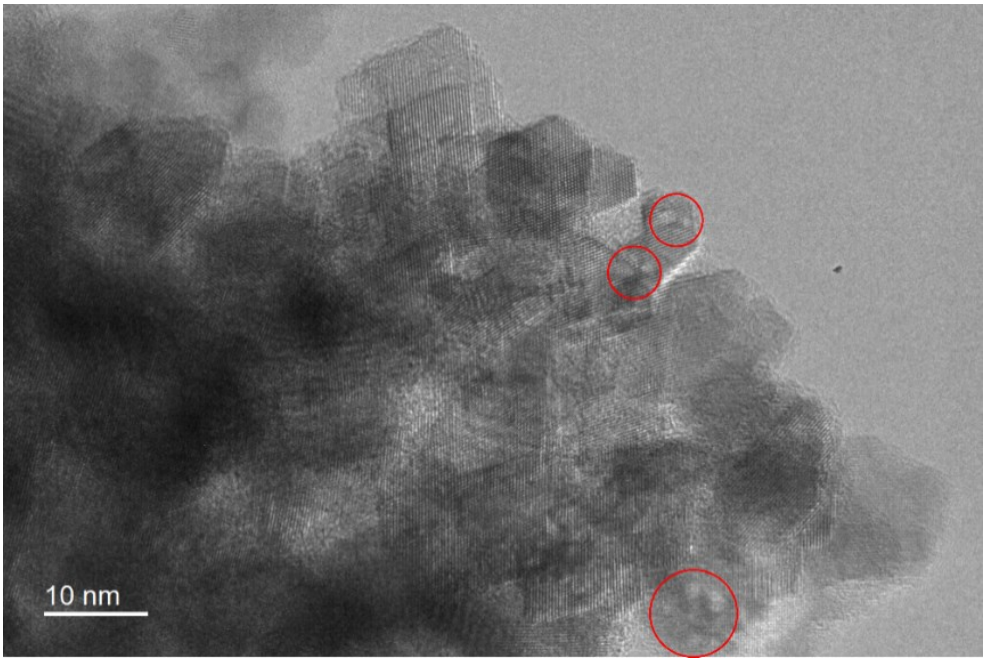

Figure 3-3. HR-TEM image of Pd/CeO_2.

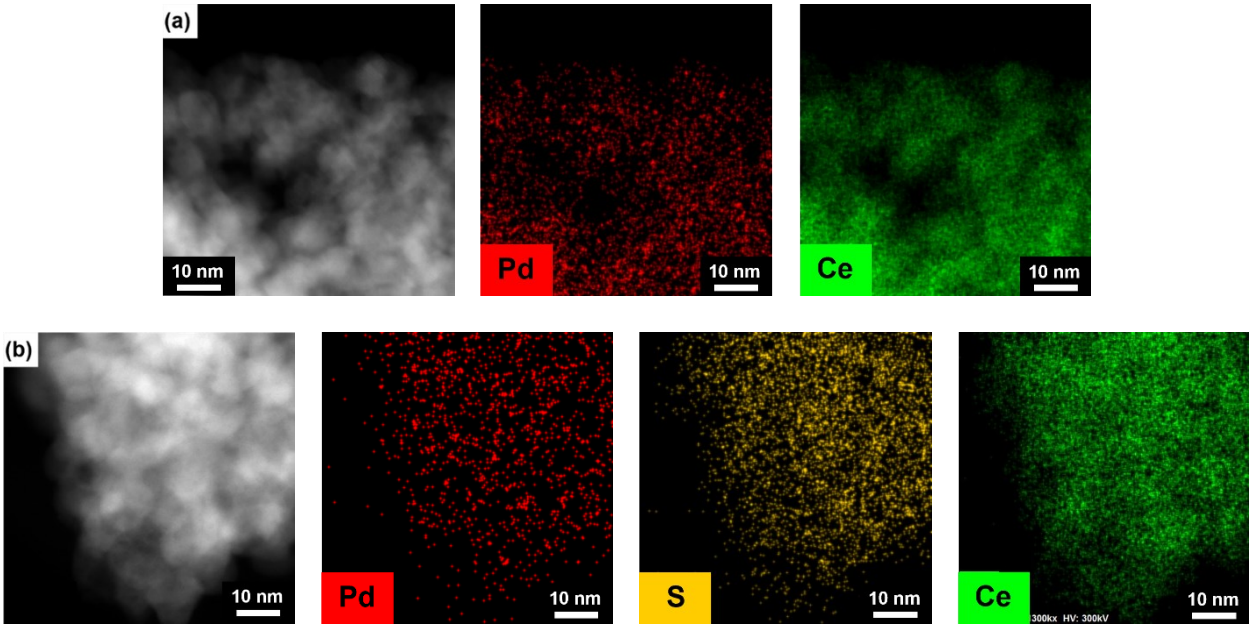

Figure 3-4. STEM-EDS image of (a)fresh Pd/CeO_2 (b)Pd/CeO_2 after SO_2 treatment at 500 °C for 300 min.

3.3.2 Investigation of structural change of CeO_2 by SO_2 with *in situ* XAFS

Figure 3-5 shows *in situ* Ce L_3-edge XANES spectra of CeO_2 and Pd/CeO_2 during SO_2 treatment at 500 °C. For fresh Pd/CeO_2 and CeO_2, peaks attributed to quasi-atomic Ce $2p_{3/2}$ to $5d_{5/2, 3/2}$ electronic transitions [23-25] are observed at 5730 and 5737 eV, indicating that Ce^{4+} is predominantly present in both samples (figure 3-5(a)). The spectra for Pd/CeO_2 and CeO_2 are almost similar, indicating that Pd loading does not affect the average oxidation state of Ce in CeO_2. After the SO_2 flow started, the intensities of the peaks at 5730 eV and 5737 eV gradually decreased for both samples, and the position of the absorption edge shifted to the lower energy side (Figure 3-5(b)). In particular, Pd/CeO_2 shows a larger change than CeO_2, with a peak at 5726 eV attributed to Ce^{3+} after 40 minutes. Therefore, the loading of Pd promotes the reduction of the supported CeO_2 in the presence of SO_2. Isosbestic points are observed for Pd/CeO_2 and CeO_2 samples, indicating that the CeO_2 support is directly converted to a chemical species containing Ce^{3+} and that no intermediate or other species are formed.

The ratio of Ce^{3+} to Ce^{4+} can be determined by applying a curve fitting to the Ce L_3-edge XANES spectra using CeO_2 and $Ce(NO_3)_3$ as the reference samples. Figure 3-6 shows the time course of the Ce^{3+}/Ce^{4+} ratio for Pd/CeO_2 and CeO_2. In the SO_2 treatment, the Ce^{3+}/Ce^{4+} ratio = 0.18 for CeO_2 after 60 minutes and did not change after that time. On the other hand, in Pd/CeO_2, the Ce^{3+}/Ce^{4+} ratio changes up to 0.68. Thus, Pd on CeO_2 promotes the reduction of CeO_2 by the SO_2 treatment.

The reaction gas was then changed to O_2 at 500 °C. In the XANES spectra of CeO_2, the Ce^{3+} peak intensity was slightly reduced (Figure 3-5(c)). Therefore, a part of the reduced CeO_2 was re-oxidized by O_2 treatment. On the other hand, the XANES spectra of Pd/CeO_2 did not change by the O_2 treatment, indicating that the sulfurized CeO_2 support in the Pd/CeO_2 was not re-oxidized by O_2. This result means that Ce_2O_3 species were not produced in the SO_2 treatment because the Ce_2O_3 species are known to be readily oxidized by oxygen back to CeO_2.

Figure 3-7 shows *in situ* Ce L_3-edge EXAFS spectra of CeO_2 and Pd/CeO_2 at 500 °C in the SO_2 flow. CeO_2 and Pd/CeO_2 samples show a Ce-O bond peak at 2 Å and a Ce-(O)-Ce bond peak at 3.5 Å. In the presence of SO_2, the intensities of these peaks decreased with time. This indicates that SO_2 reduced the structural regularity of CeO_2. After 40 min, the peak intensities of Ce-O and Ce-O-Ce bonds after the SO_2 treatment were lower for Pd/CeO_2 than for CeO_2. Thus, the Pd loading decreases structural regularity due to the SO_2 treatment. No change was observed in the EXAFS spectra of Pd/CeO_2 when the gas flow was changed to the O_2 flow. On the other hand, the peak intensity of the Ce-O bond slightly increased for the unpromoted CeO_2. From the XANES studies (Figure 3-5(c)) mentioned above, Ce^{3+} is partially reoxidized to Ce^{4+} when O_2 is introduced after SO_2 treatment for unpromoted CeO_2. These findings also indicate that the Pd loading improves the stability of sulfurized CeO_2.

We subsequently tracked the state of sulfur species formed on the catalysts during the SO_2 treatment. Figure 3-8 shows *in situ* S K-edge XANES spectra of CeO_2 and Pd/CeO_2 during SO_2 treatment at 500 °C in N_2. Both catalysts mainly showed the peak at 2.481 keV, assignable to SO_4^{2-} species. The peak intensity increased after 60 min, and the spectrum shape was almost unchanged. For Pd/CeO_2, no other S-containing species with lower valence were detected, further indicating that SO_2 directly reacted with Pd/CeO_2 to form the chemical species containing sulfate. For CeO_2, the small peak attributed to S^{4+} was also detected near 2.479 keV. However, it was oxidized to S^{6+} after 60 minutes. Thus, both Pd/CeO_2 and CeO_2 were reacted to form sulfate species on the catalyst in the SO_2 treatment.

It has been reported that the deposition of Pd on CeO_2 greatly improved its reactivity [32-34]. In this case, the reactivity of the interface with CeO_2, with which the Pd is contacted, is improved. The state of Pd during this process strongly affects the reactivity. Therefore, the state of Pd during the SO_2 treatment process was traced by *in situ* Pd L_3-edge XANES measurements. Figure 3-9 shows the Pd L_3-edge XANES spectra during the SO_2 treatment at 500 °C. Here, the

measurement conditions were the same as those for the *in situ* Ce L_3-edge XAFS measurements. Pd L_3-edge spectrum corresponds to the 2p → 4d transition. Therefore, this XANES spectrum shows the information on the d electron density (oxidation state) of Pd. The Pd L_3-edge spectra did not change during the SO_2 treatment, revealing that Pd reduction and sulfide formation did not occur under our conditions.

XRF analyses revealed the amount of sulfur species on the SO_2-poisoned CeO_2 and Pd/CeO_2 catalysts (Table 3-1). The mol ratio of S/CeO_2 was 0.24 for Pd/CeO_2 and 0.09 for CeO_2, indicating that more sulfate species were detected on Pd/CeO_2 than on CeO_2. Therefore, the Pd deposition promotes the reduction of CeO_2 and the formation of sulfate species in the catalysts. These results showed that lattice oxygen in CeO_2 was removed, and SO_4^{2-} was formed when SO_2 was introduced to Pd/CeO_2, whereas the fluorite structure was maintained. Based on the amount of sulfate species and that of Ce^{3+}, the molar ratio of Ce^{3+}/S was approximately 1.7 for both samples.

The reduction behavior of Pd/CeO_2 by SO_2 depends on the reaction temperature. Figure 3-10 shows *in situ* Ce L_3-edge XANES spectra in the presence of SO_2 at 200 °C and 400 °C. At 400 °C, the position of the absorption edge shifted to the lower energy side, and the intensity of the peak attributed to Ce^{4+} decreased, indicating that Ce^{4+} sites were partly reduced to Ce^{3+} by the SO_2 treatment. In this case, the isosbestic point was still observed, indicating that CeO_2 was directly converted to chemical species containing Ce^{3+} even when the reaction temperature was decreased. However, the Ce^{3+}/Ce^{4+} ratio determined from curve fitting was lower than that in the SO_2 treatment at 500 °C, indicating that the decrease in reaction temperature reduced the degree of Ce reduction. At 200 °C, little spectral change was observed even after SO_2 was circulated for a long time. In this case, only the topmost surface of CeO_2 was sulfurized.

The composition of sulfurized cerium compounds has already been extensively studied. Thermodynamically, $Ce(SO_4)_2$ and $Ce_2(SO_4)_3$ are stable. Unlike other rare earth elements,

cerium oxysulfate is not expected to be present [27]. From other previous reports, it is also known that cerium sulfate oxide ($Ce_2O_2SO_4$) that contains Ce^{3+} is formed when CeO_2 is contacted with SO_2 [28, 29]. In this study, it is also possible that cerium sulfate oxide is mainly formed because the molar ratio of Ce^{3+}/S was approximately 1.7 species. The presence of isosbestic points in both Pd/CeO_2 and CeO_2 samples confirms that CeO_2 is directly converted to cerium sulfate oxide upon contact with SO_2 and that no other intermediate species are observed.

H_2-TPR profiles provide information on the reducibility of CeO_2 and Pd/CeO_2 (Figure 3-11). For the CeO_2, the H_2-TPR profile exhibited two reduction peaks in a lower temperature range (50-600 °C) and higher temperature range (600-950 °C), which were assigned to the H_2 reduction of surface and bulk of CeO_2, respectively [30]. In H_2-TPR with Pd/CeO_2, the H_2 reduction peak in the lower temperature range disappeared. This finding suggests that H_2 is dissociated and reduces the surface CeO_2 at 50 °C during pretreatment [31]. Thus, Pd loading improves the reactivity of the surface lattice oxygen. On the other hand, the H_2 reduction profile at the high-temperature side was not changed by Pd loading, indicating that Pd on CeO_2 does not affect the reactivity of the lattice oxygen in bulk.

XANES measurement was carried out for CeO_2 and Pd/CeO_2 at 600 °C under H_2 (Figure 3-12(a)). As described above, H_2 reacts with the surface lattice oxygen at 50-600 °C. Therefore, the hydrogen reduction with the surface lattice oxygen proceeds at 600 °C. Thus, this measurement condition allowed us to track the reduction process for the surface lattice oxygen. In both samples, the position of the absorption edge shifted, indicating that CeO_2 was reduced. In these cases, both samples show similar reduction profiles. The linear combination fitting for the Ce L_3-edge spectra showed that 15 % of Ce^{4+} sites were reduced to Ce^{3+} at 600 °C. The ratio of Ce^{3+} to Ce^{4+} after the H_2 reduction was the same extent for CeO_2 and Pd/CeO_2.

Figure 3-12(b) shows *in situ* Ce L_3-edge EXAFS spectra of CeO_2 and Pd/CeO_2 in the H_2 flow at 600 °C The peak intensities of the Ce-O and Ce-O-Ce bond-derived peaks in both CeO_2 and Pd/CeO_2 decreased in the H_2 flow at 600 °C. Therefore, it is clear that H_2 treatment decreases the structural regularity of CeO_2. The peak intensity after H_2 reduction was similar for CeO_2 and Pd/CeO_2. The presence of Pd promoted the reduction of CeO_2 but did not affect the structures of the reduced CeO_2.

Based on the above results, we again discuss the *in situ* Ce L_3-edge XANES spectra in the SO_2 treatment. For CeO_2, the Ce^{3+}/Ce^{4+} ratio after the SO_2 treatment at 500 °C was the same as that after H_2 reduction at 600 °C. This finding indicates that the surface lattice oxygen was consumed by SO_2 to form sulfate species during the SO_2 treatment. Even after prolonged SO_2 treatment, only the surface lattice oxygen was consumed, and the lattice oxygen in bulk was not reacted with SO_2. On the other hand, in the case of SO_2 treatment with Pd/CeO_2, the Ce^{3+}/Ce^{4+} ratio exceeded the value in the H_2 reduction at 600 °C, revealing that not only the surface lattice oxygen but also the bulk lattice oxygen was consumed in the SO_2 treatment. These results indicate that Pd loading on the surface of CeO_2 promotes the reaction of SO_2 with CeO_2 on the support and significantly enhances the reaction with surface lattice oxygen and bulk lattice oxygen.

XPS studies were performed to investigate the surface structure of the Pd/CeO_2 catalyst before and after SO_2 treatment at 500 °C (Figure 3-13). Ce 3d XPS spectra show peaks of V, V', V'', V''', U, U'', U''', U'''' [35-37]. The peaks of U correspond to the $3d_{3/2}$ orbital interaction and V to the $3d_{5/2}$ orbital interaction, respectively. Among these peaks, the U' and V' peaks are attributed to Ce^{3+} species [35, 37], while in fresh CeO_2, peaks attributed to Ce^{4+} were mainly detected. The peak intensities of U' and V' increased after SO_2 treatment, confirming the tendency of SO_2 to reduce Ce^{4+} to Ce^{3+}, similar to the *in situ* XAFS results. The average free

path of electrons in CeO_2 is about 2 nm [38, 39], suggesting that the Ce^{4+} and Ce^{3+} are present at the topmost surface of the SO_2-treated Pd/CeO_2 samples.

It has been reported that cerium sulfate oxide is reported to have excellent oxygen storage properties [20, 21]. This finding prompted us to investigate the CO oxidation activity of Pd/CeO_2 after SO_2 treatment. Figure 3-14 shows the effect of SO_2 treatment on CO oxidation with Pd/CeO_2. The Pd/CeO_2 catalyst shows high activity at 120 °C and higher temperatures. After the SO_2 treatment at 500 °C, the CO oxidation activity completely deteriorated. Thus, the sulfurized Pd/CeO_2 exhibited almost no CO oxidation activity. Particularly, even after the SO_2 treatment at 200 °C, the light-off temperatures increased, and CO oxidation activity was greatly reduced. This indicates that only sulfurizing the surface of Pd/CeO_2 significantly decreases CO oxidation activity.

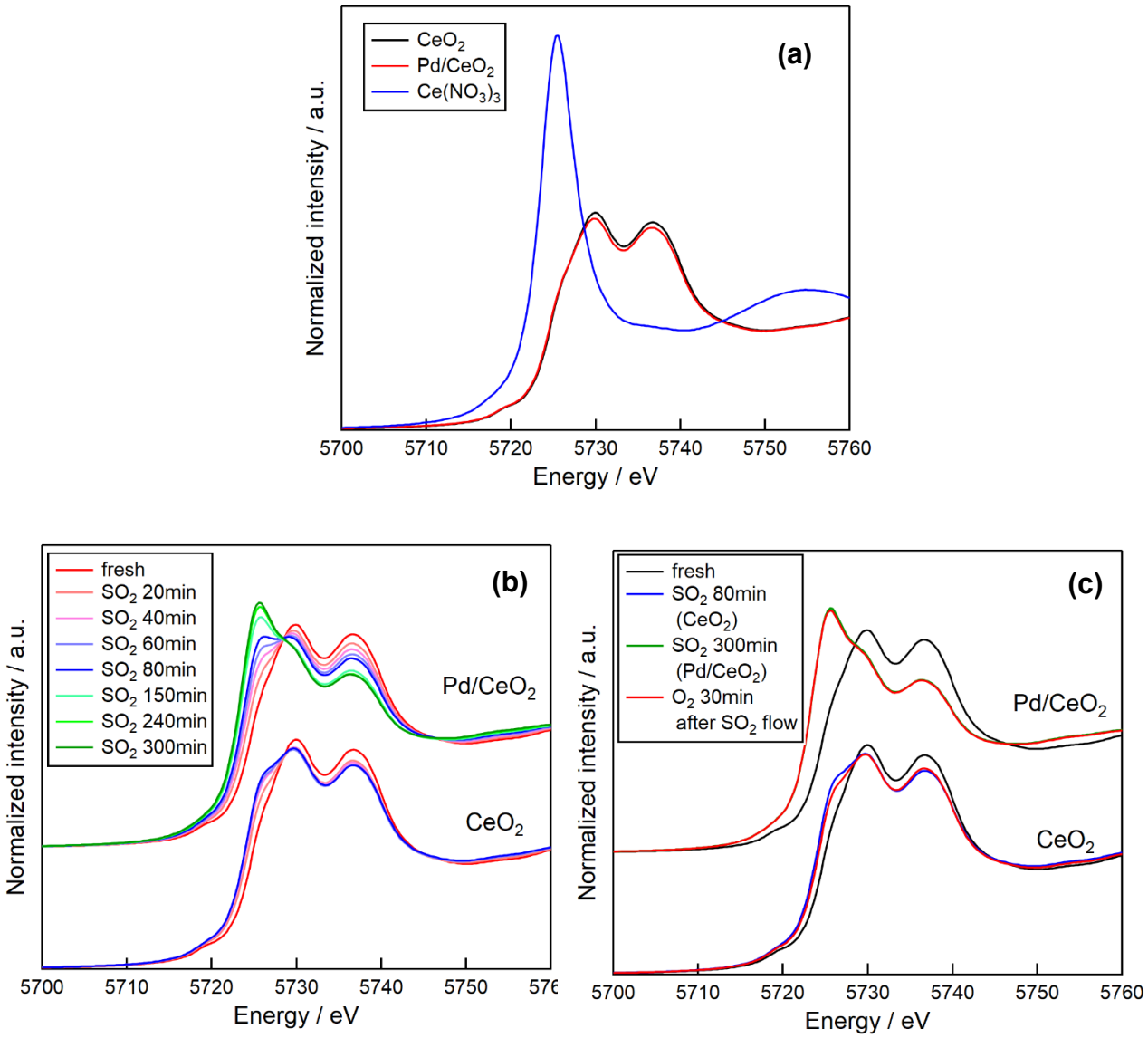

Figure 3-5. Ce L_3-XANES spectra of CeO_2 and Pd/CeO_2.

(a)XANES spectra of references samples, (b)XANES spectra under SO_2 flow, (c)XANES spectra under O_2 flow after SO_2 flow.

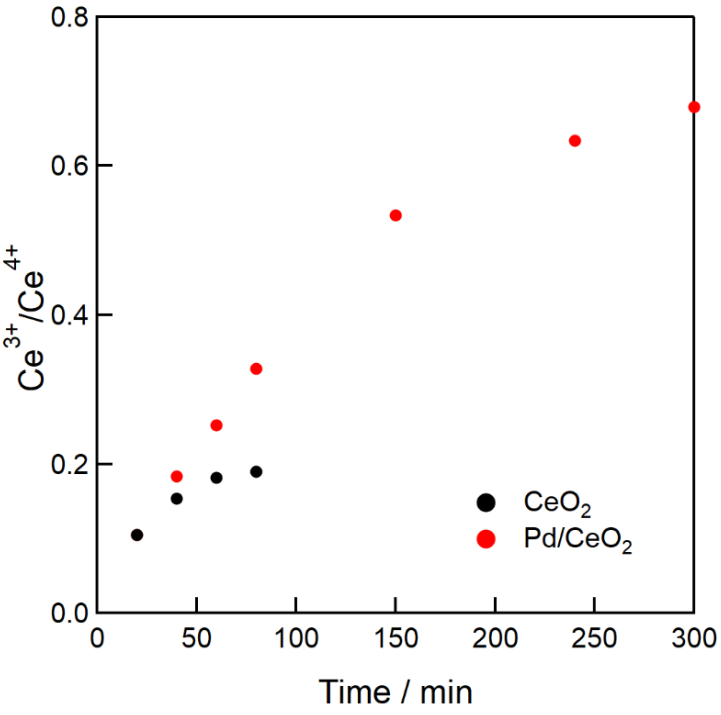

Figure 3-6. The change over time of the Ce^{3+}/Ce^{4+} ratio for Pd/CeO_2 and CeO_2.

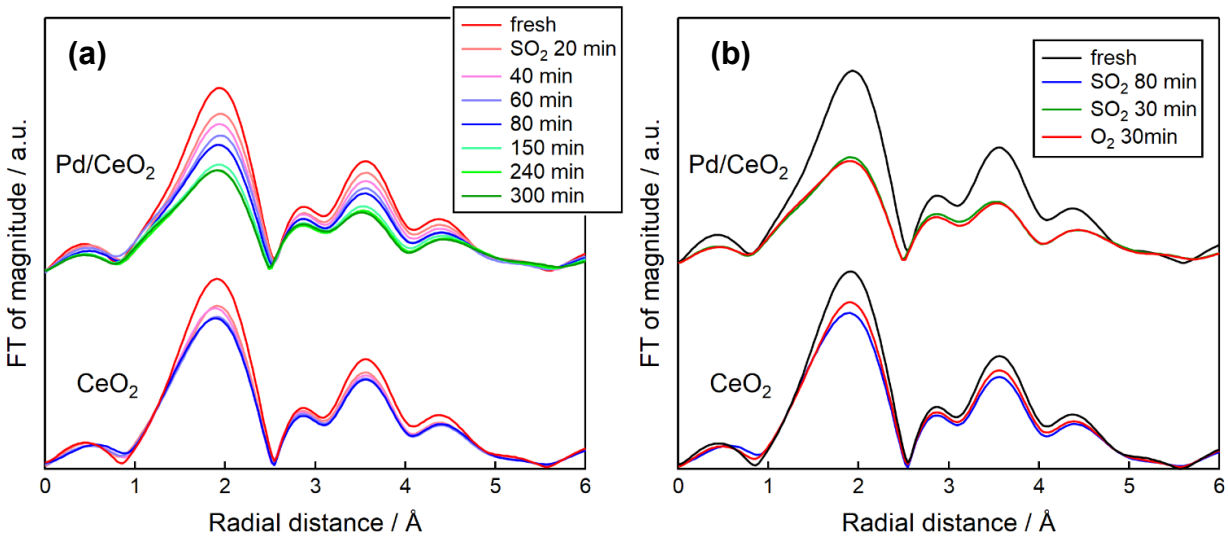

Figure 3-7. EXAFS spectra under SO_2 flow and O_2 flow.

(a)EXAFS spectra under SO_2 flow, (b)EXAFS spectra under O_2 flow after SO_2 flow.

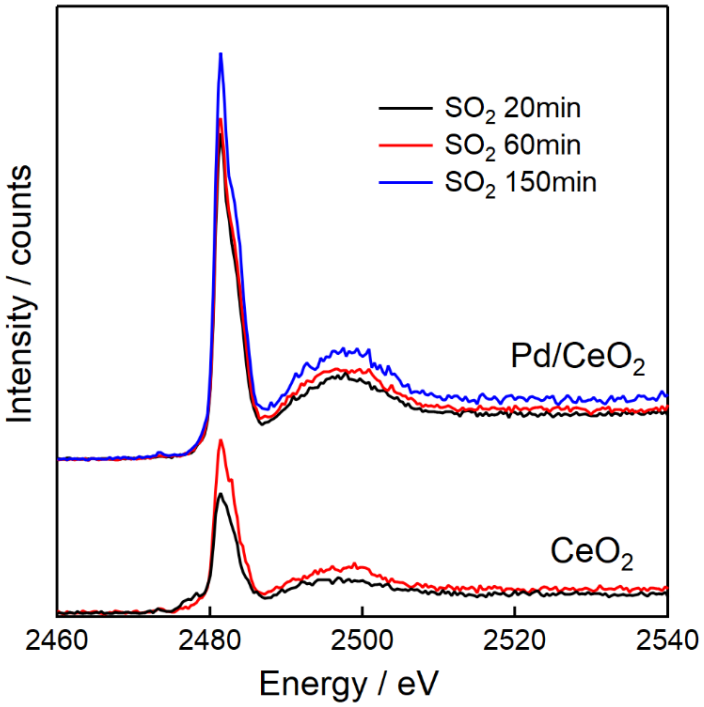

Figure 3-8. S K-XANES spectra of CeO_2 and Pd/CeO_2 under SO_2 flow.

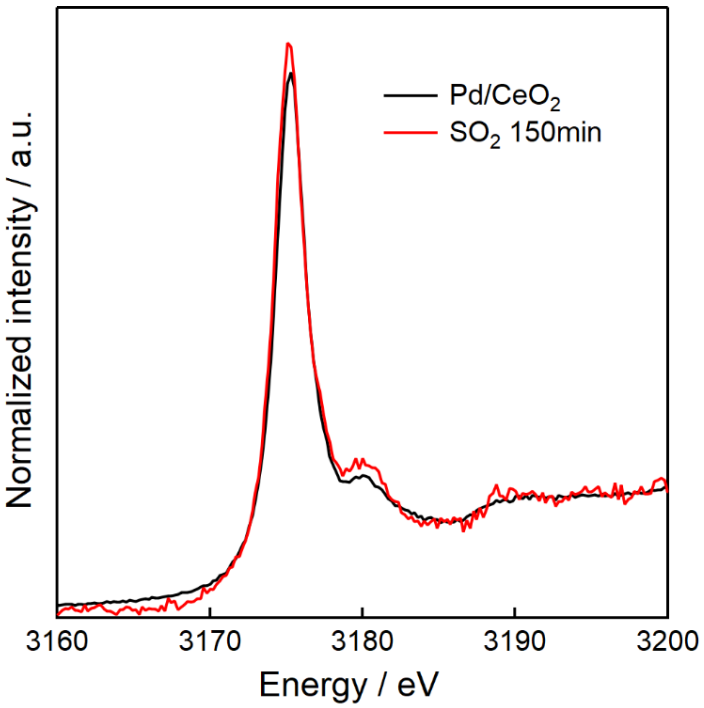

Figure 3-9. Pd L_3-XANES spectra of Pd/CeO_2 under SO_2 flow.

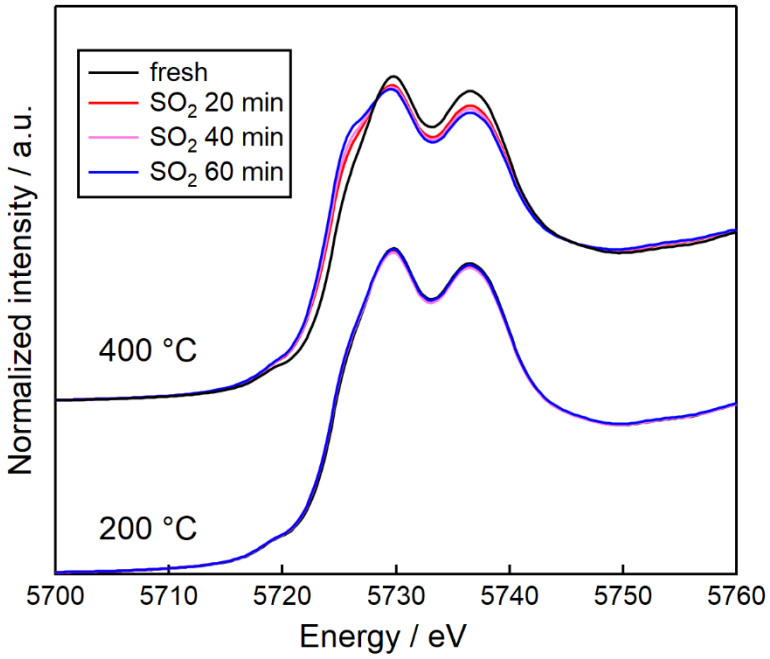

Figure 3-10. Ce L_3-XANES spectra of CeO_2 and Pd/CeO_2 under SO_2 flow at 200 °C and 400 °C.

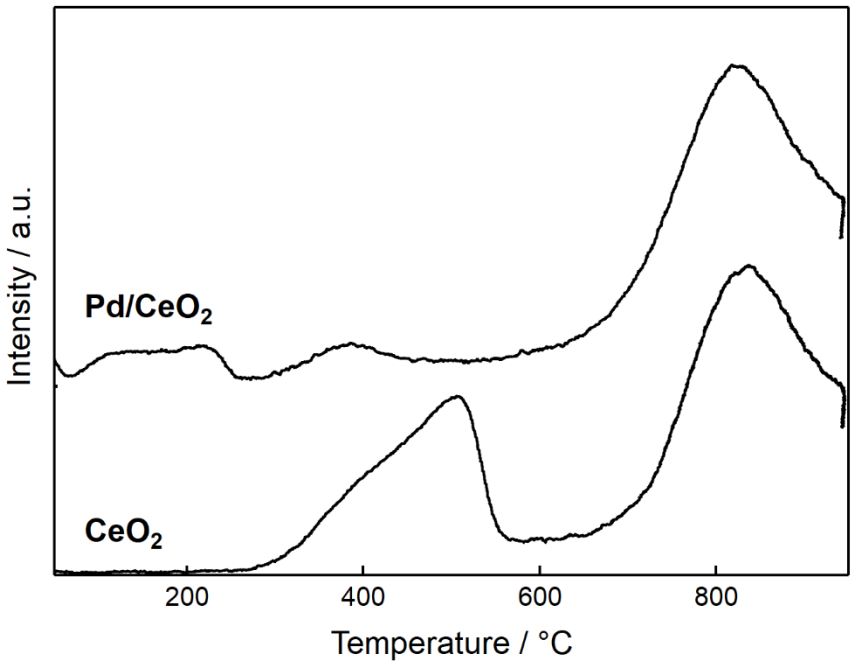

Figure 3-11. H_2-TPR profile of CeO_2 and Pd/CeO_2.

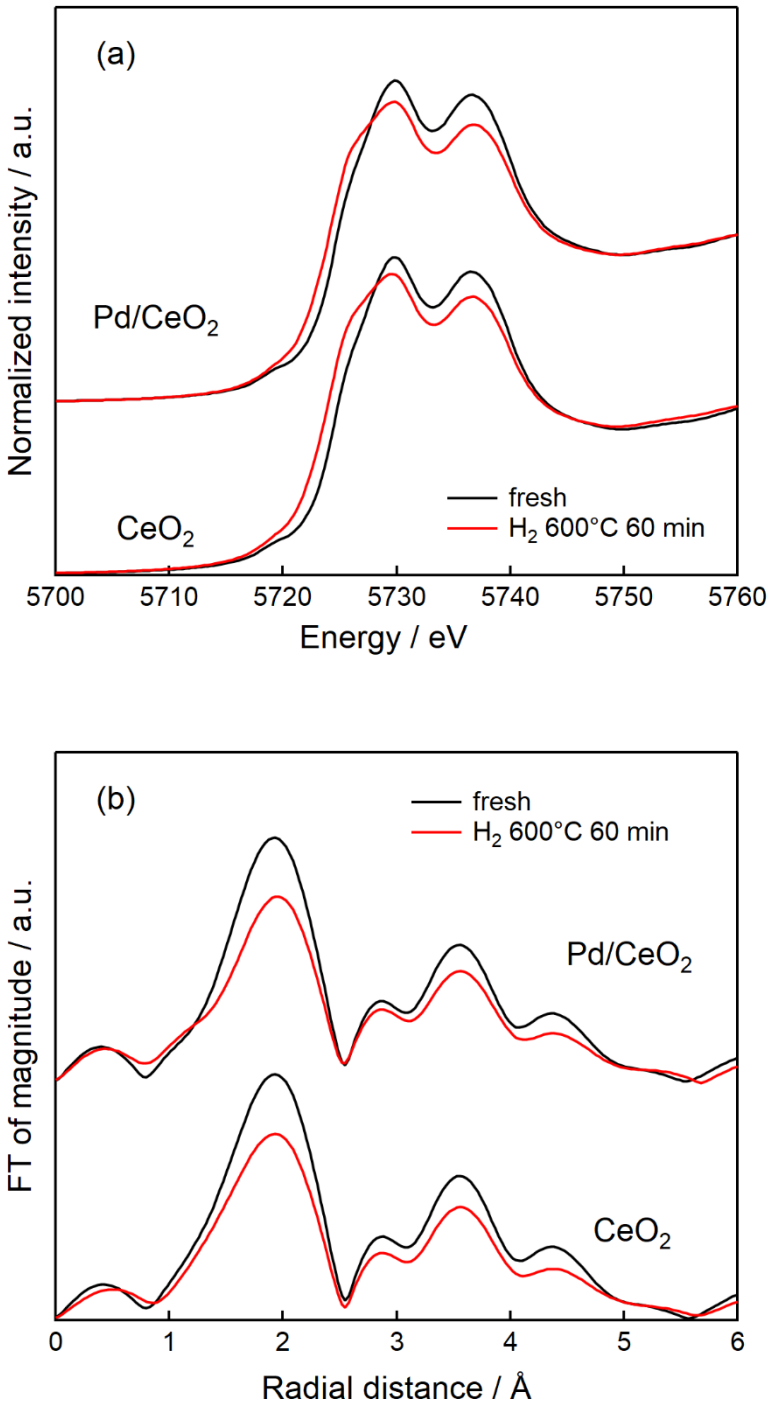

Figure 3-12. (a)Ce L_3-XANES spectra and (b)EXAFS spectra of CeO_2 and Pd/CeO_2 under H_2 flow.

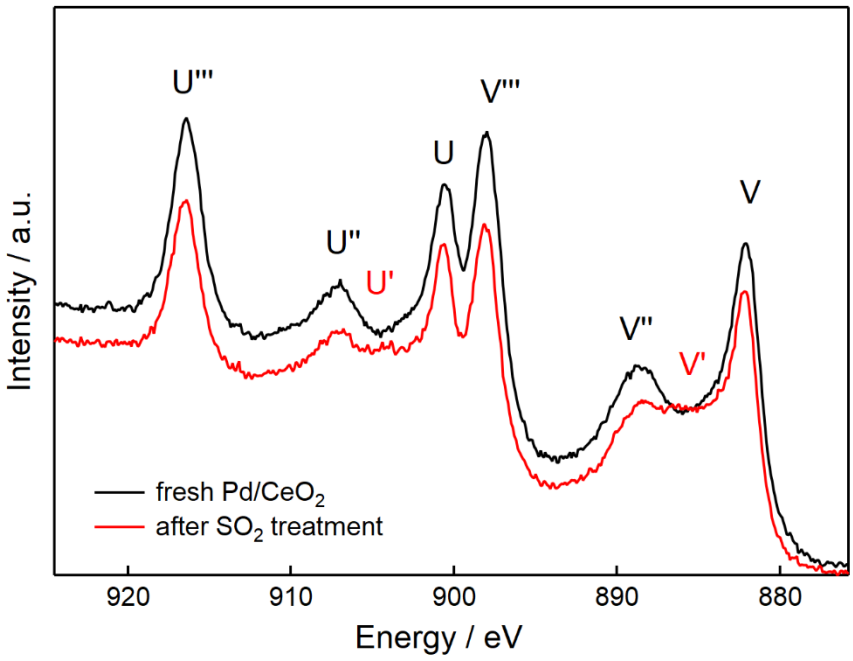

Figure 3-13. XPS spectra of Pd/CeO_2 and 500 °C SO_2 treated Pd/CeO_2.

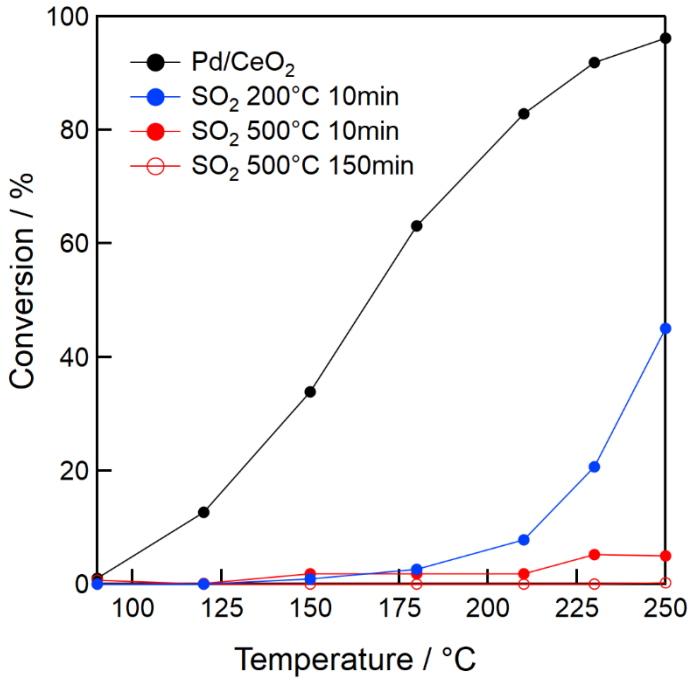

Figure 3-14. catalytic CO oxidation activity of the fresh catalyst and after SO_2 treatment.

Table 3-1. Ce ion ratios calculated by linear combination fitting with standards and the molar ratio of SO_3/CeO_2 calculated by XRF.

	Ce^{3+}	Ce^{4+}	SO_3/CeO_2
CeO_2 after SO_2	**0.15**	**0.85**	**0.09**
Pd/CeO_2 after SO_2	**0.40**	**0.60**	**0.24**
CeO_2 after H_2	**0.15**	**0.85**	**-**
Pd/CeO_2 after H_2	**0.15**	**0.85**	**-**

3.4 Conclusion

In this study, *in situ* XAFS measurements were performed to understand the structural changes of Pd/CeO_2 in the SO_2 treatment. The Ce^{3+}/Ce^{4+} ratio was obtained by curve fitting the Ce L_3 absorption edge spectra compared with the spectra of reference samples containing Ce^{3+} and Ce^{4+}. We obtained the important results from the Ce L_3-, S K-, and Pd L_3-edge XANES studies, along with XRD and SEM-EDS mapping. 1) the SO_2 treatment at 500 °C sulfurized the surface lattice of CeO_2 to form sulfate and Ce^{3+} species. 2) Addition of Pd to CeO_2 promoted the sulfurization of CeO_2; by the SO_2 treatment at 500 °C, the inner lattice oxygen and the surface lattice oxygen were reacted with SO_2 in Pd/CeO_2, resulting in the formation of Ce^{3+} and sulfate species. 3) Re-oxidation of Ce^{3+} did not occur in Pd/CeO_2 when oxygen was contacted with Pd/CeO_2 after sulfurization. 4) The entire Pd/CeO_2 sample was sulfurized by SO_2. 5) Pd species were not sulfurized by the SO_2 treatment. The chemical species formed by sulfurization of Pd/CeO_2 by SO_2 (cerium sulfate oxide) has a fluorite structure similar to CeO_2, but the structure is less regular than CeO_2. The sulfurized CeO_2 showed lower activity for CO oxidation.

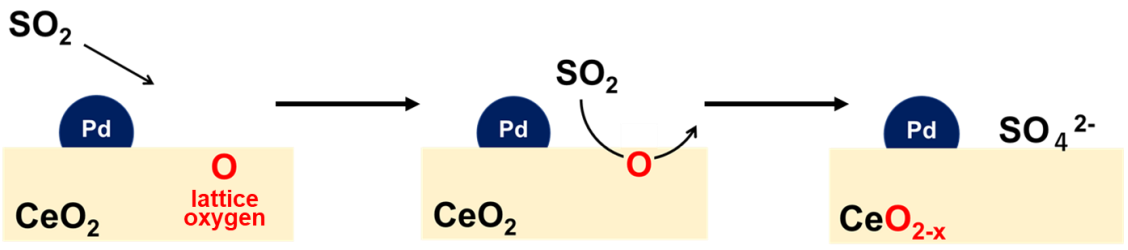

Figure 3-15. Sulfur poisoning process of Pd/CeO_2 investigated in chapter 3.

References

[1] Wang, J.; Chen, H.; Hu, Z.; Yao, M.; Li, Y. A Review on the Pd-Based Three-Way Catalyst. *Catalysis Reviews* **2015**, *57* (1), 79–144.

[2] van Spronsen, M. A.; Frenken, J. W. M.; Groot, I. M. N. Surface Science under Reaction Conditions: CO Oxidation on Pt and Pd Model Catalysts. *Chem. Soc. Rev.* **2017**, *46* (14), 4347–4374.

[3] Ciuparu, D.; Lyubovsky, M. R.; Altman, E.; Pfefferle, L. D.; Datye, A. CATALYTIC COMBUSTION OF METHANE OVER PALLADIUM-BASED CATALYSTS. *Catalysis Reviews* **2002**, *44* (4), 593–649.

[4] Heck, R. M.; Farrauto, R. J. Automobile Exhaust Catalysts. *Appl. Catal. A* **2001**, *221* (1), 443–457.

[5] Ryou, Y.; Lee, J.; Lee, H.; Choung, J. W.; Yoo, S.; Kim, D. H. Roles of ZrO_2 in SO_2-Poisoned Pd/(Ce-Zr)O_2 Catalysts for CO Oxidation. *Catal. Today* **2015**, *258*, 518–524.

[6] Kaneeda, M.; Iizuka, H.; Hiratsuka, T.; Shinotsuka, N.; Arai, M. Improvement of Thermal Stability of NO Oxidation Pt/Al_2O_3 Catalyst by Addition of Pd. *Appl. Catal. B* **2009**, *90* (3), 564–569.

[7] Chen, M.; Schmidt, L. D. Morphology and Composition of Pt-Pd Alloy Crystallites on SiO_2 in Reactive Atmospheres. *J. Catal.* **1979**, *56* (2), 198–218.

[8] Bartholomew, C. H. Mechanisms of Catalyst Deactivation. *Appl. Catal. A* **2001**, *212* (1), 17–60.

[9] Gélin, P.; Primet, M. Complete Oxidation of Methane at Low Temperature over Noble Metal Based Catalysts: A Review. *Appl. Catal. B* **2002**, *39* (1), 1–37.

[10] Colussi, S.; Arosio, F.; Montanari, T.; Busca, G.; Groppi, G.; Trovarelli, A. Study of Sulfur Poisoning on Pd/Al_2O_3 and Pd/CeO_2/Al_2O_3 Methane Combustion Catalysts. *Catal. Today* **2010**, *155* (1), 59–65.

[11] Gandhi, H. S.; Shelef, M. Effects of Sulphur on Noble Metal Automotive Catalysts. *Appl. Catal.* **1991**, *77* (2), 175–186.

[12] Pinna, F.; Menegazzo, F.; Signoretto, M.; Canton, P.; Fagherazzi, G.; Pernicone, N. Consecutive Hydrogenation of Benzaldehyde over Pd Catalysts: Influence of Supports and Sulfur Poisoning. *Appl. Catal. A* **2001**, *219* (1), 195–200.

[13] Monai, M.; Montini, T.; Melchionna, M.; Duchoň, T.; Kúš, P.; Chen, C.; Tsud, N.; Nasi, L.; Prince, K. C.; Veltruská, K.; Matolín, V.; Khader, M. M.; Gorte, R. J.; Fornasiero, P. The

Effect of Sulfur Dioxide on the Activity of Hierarchical Pd-Based Catalysts in Methane Combustion. *Appl. Catal. B* **2017**, *202*, 72–83.

[14] Chenakin, S. P.; Melaet, G.; Szukiewicz, R.; Kruse, N. XPS Study of the Surface Chemical State of a Pd/(SiO_2+TiO_2) Catalyst after Methane Oxidation and SO_2 Treatment. *J. Catal.* **2014**, *312*, 1–11.

[15] Kinnunen, N. M.; Hirvi, J. T.; Kallinen, K.; Maunula, T.; Keenan, M.; Suvanto, M. Case Study of a Modern Lean-Burn Methane Combustion Catalyst for Automotive Applications: What Are the Deactivation and Regeneration Mechanisms? *Appl. Catal. B* **2017**, *207*, 114–119.

[16] Kolli, T.; Huuhtanen, M.; Hallikainen, A.; Kallinen, K.; Keiski, R. L. The Effect of Sulphur on the Activity of Pd/Al_2O_3, Pd/CeO_2 and Pd/ZrO_2 Diesel Exhaust Gas Catalysts. *Catal. Letters* **2009**, *127* (1), 49–54.

[17] Yang, H.; Wei, G.; Wang, X.; Lin, F.; Wang, J.; Shen, M. Regeneration of SO_2-Poisoned Diesel Oxidation Pd/CeO_2 Catalyst. *Catal. Commun.* **2013**, *36*, 5–9.

[18] Luo, T.; Gorte, R. J. Characterization of SO_2-Poisoned Ceria-Zirconia Mixed Oxides. *Appl. Catal. B* **2004**, *53* (2), 77–85.

[19] Flouty, R.; Abi-Aad, E.; Siffert, S.; Aboukaïs, A. Formation of Cereous Sulphate Phase upon Interaction of SO_2 with Ceria at Room Temperature. *J. Therm. Anal. Calorim.* **2003**, *73* (3), 727–734.

[20] Liu, X.; Wang, P.; Shen, Y.; Bi, S.; Ren, W.; Zhang, D. Boosting SO_2-Tolerant Catalytic Reduction of NOx via Selective Adsorption and Activation of Reactants over Ce^{4+}–SO_4^{2-} Pair Sites. *ACS Catal.* **2022**, *12* (18), 11306–11317.

[21] Hilaire, S.; Sharma, S.; Gorte, R. J.; Vohs, J. M.; Jen, H.-W. Effect of SO_2 on the Oxygen Storage Capacity of Ceria-Based Catalysts. *Catal. Letters* **2000**, *70* (3), 131–135.

[22] Ravel, B.; Newville, M. ATHENA, ARTEMIS, HEPHAESTUS: Data Analysis for X-Ray Absorption Spectroscopy Using IFEFFIT. *J. Synchrotron Radiat.* **2005**, *12* (Pt 4), 537–541.

[23] Soldatov, A. V.; Ivanchenko, T. S.; Della Longa, S.; Kotani, A.; Iwamoto, Y.; Bianconi, A. Crystal-Structure Effects in the Ce L_3-Edge X-Ray-Absorption Spectrum of CeO_2: Multiple-Scattering Resonances and Many-Body Final States. *Phys. Rev. B: Condens. Matter Mater. Phys.* **1994**, *50* (8), 5074.

[24] Nachimuthu, P.; Shih, W.-C.; Liu, R.-S.; Jang, L.-Y.; Chen, J.-M. The Study of Nanocrystalline Cerium Oxide by X-Ray Absorption Spectroscopy. *J. Solid State Chem.* **2000**, *149* (2), 408–413.

[25] Dexpert, H.; Karnatak, R. C.; Esteva, J.-M.; Connerade, J. P.; Gasgnier, M.; Caro, P. E.;

Albert, L. X-Ray Absorption Studies of CeO_2,PrO_2, andTbO_2. II. Rare-Earth Valence State byLIIIabsorption Edges. *Phys. Rev. B Condens. Matter* **1987**, *36* (3), 1750–1753.

[26] Xu, Y.; Yamazaki, M.; Villars, P. Inorganic Materials Database for Exploring the Nature of Material. *Jpn. J. Appl. Phys.* **2011**, *50* (11S), 11RH02.

[27] Dwivedi, R. K.; Kay, D. A. R. Thermodynamics of the Oxidation of Rare Earth Oxysulfides at High Temperatures. *Metall. Trans. B* **1984**, *15* (3), 523–528.

[28] Smirnov, M. Y.; Kalinkin, A. V.; Pashis, A. V.; Sorokin, A. M.; Noskov, A. S.; Kharas, K. C.; Bukhtiyarov, V. I. Interaction of Al_2O_3 and CeO_2 Surfaces with SO_2 and SO_2 + O_2 Studied by X-Ray Photoelectron Spectroscopy. *J. Phys. Chem. B* **2005**, *109* (23), 11712–11719.

[29] Smirnov, M. Y.; Kalinkin, A. V.; Pashis, A. V.; Prosvirin, I. P.; Bukhtiyarov, V. I. Interaction of SO_2 with Pt Model Supported Catalysts Studied by XPS. *J. Phys. Chem. C Nanomater. Interfaces* **2014**, *118* (38), 22120–22135.

[30] Romeo, M.; Bak, K.; El Fallah, J.; Le Normand, F.; Hilaire, L. XPS Study of the Reduction of Cerium Dioxide. *Surf. Interface Anal.* **1993**, *20* (6), 508–512.

[31] Leitenburg, C. de; Trovarelli, A.; Kašpar, J. A Temperature-Programmed and Transient Kinetic Study of CO_2 Activation and Methanation over CeO_2 Supported Noble Metals. *J. Catal.* **1997**, *166* (1), 98–107.

[32] Shigenobu, S.; Hojo, H.; Einaga, H. Catalytic Oxidation of CO to CO_2 over CeO_2-Supported Pd–Cu Catalysts under Dilute O_2 Conditions. *Ind. Eng. Chem. Res.* **2022**, *61* (43), 15856–15865.

[33] Oh, S.-H.; Hoflund, G. B. Chemical State Study of Palladium Powder and Ceria-Supported Palladium during Low-Temperature CO Oxidation. *J. Phys. Chem. A* **2006**, *110* (24), 7609–7613.

[34] Luo, M.-F.; Hou, Z.-Y.; Yuan, X.-X.; Zheng, X.-M. Characterization Study of CeO_2 Supported Pd Catalyst for Low-Temperature Carbon Monoxide Oxidation. *Catal. Letters* **1998**, *50* (3), 205–209.

[35] Park, P. W.; Ledford, J. S. Effect of Crystallinity on the Photoreduction of Cerium Oxide: A Study of CeO_2 and Ce/Al_2O_3 Catalysts. *Langmuir* **1996**, *12* (7), 1794–1799.

[36] Bêche, E.; Charvin, P.; Perarnau, D.; Abanades, S.; Flamant, G. Ce 3d XPS Investigation of Cerium Oxides and Mixed Cerium Oxide (CexTiyOz). *Surf. Interface Anal.* **2008**, *40* (3-4), 264–267.

[37] Fornasiero, P.; Balducci, G.; Di Monte, R.; Kašpar, J.; Sergo, V.; Gubitosa, G.; Ferrero, A.; Graziani, M. Modification of the Redox Behaviour of CeO_2Induced by Structural Doping

with ZrO2. *J. Catal.* **1996**, *164* (1), 173–183.

[38] Powell, C. J.; Jablonski, A. NIST Electron Inelastic-Mean-Free-Path Database 71, Version 1.0. *Cedric J. Powell, Aleksander Jablonski* **1999**.

[39] Tanuma, S.; Powell, C. J.; Penn, D. R. Calculations of Electron Inelastic Mean Free Paths. V. Data for 14 Organic Compounds over the 50–2000 eV Range. *Surf. Interface Anal.* **1994**, *21* (3), 165–176.

Chapter 4 Structural change of Pd/c-CeO_2 by SO_2

4.1 Introduction

The morphology of CeO_2 can be controlled by using appropriate synthesis methods. Zhou et al. successfully synthesized rod CeO_2 with exposed 100 and 110 planes [1]. Since then, many researchers have reported on the morphology control of CeO_2. To date, in addition to rod CeO_2, synthesis of cubic CeO_2 with exposed 100 planes and octahedral CeO_2 with exposed 111 planes have been reported [2-4]. Such morphology-controlled CeO_2 is synthesized by selective adsorption of anion species on specific crystal faces, thereby inhibiting crystal growth on those faces. Various studies have reported the correlation between the exposed face and catalytic properties, taking advantage of the ability to expose only specific planes [5-12].

The metal-support interaction is one of the factors that determine catalytic properties. The reasons for supporting noble metals, which are the active components, on supports are to increase the specific surface area of the noble metals and to improve their stability. In addition, interactions at the metal-support interface can give new catalytic properties not observed for the metal alone. Furthermore, the metal-support interface can be the active site of a catalytic reaction. Therefore, the catalytic properties at the metal-support interface are an important factor in investigating the reaction mechanism of catalysts. On the other hand, interfaces are difficult to observe and evaluate structurally, and not enough knowledge has been obtained about structural changes at interfaces.

Scanning transmission electron microscopy (STEM) helps analyze local structures such as interfaces. Figure 4-1 shows a schematic diagram of STEM-EELS: In STEM-EELS measurement, an electron beam is narrowed down to about one atom by a focusing lens, scanned over the sample, and the electrons transmitted through the sample are detected to obtain

an EELS spectrum. By analyzing this spectrum, it is possible to evaluate the valence of the sample.

In this chapter, the change in catalytic properties of Pd/CeO_2 due to SO_2 is analyzed in more detail at the atomic level. In Chapter 3, the effect of SO_2 on the catalytic structure of Pd/CeO_2 is discussed using *in situ* XAFS measurements. The results showed that Pd/CeO_2 was reduced to Ce^{3+} under SO_2 flow. Pd loading promoted the reduction of CeO_2 by SO_2. In this chapter, morphology-controlled cubic CeO_2 (c-CeO_2) was synthesized and used as catalyst support to investigate further the SO_2-induced changes in catalyst structure, especially the reduction of supported CeO_2. Furthermore, I succeeded in analyzing the structural change of Pd/c-CeO_2 induced by SO_2 at the atomic level by STEM-EELS and in observing the change in the Pd-CeO_2 interface structure.

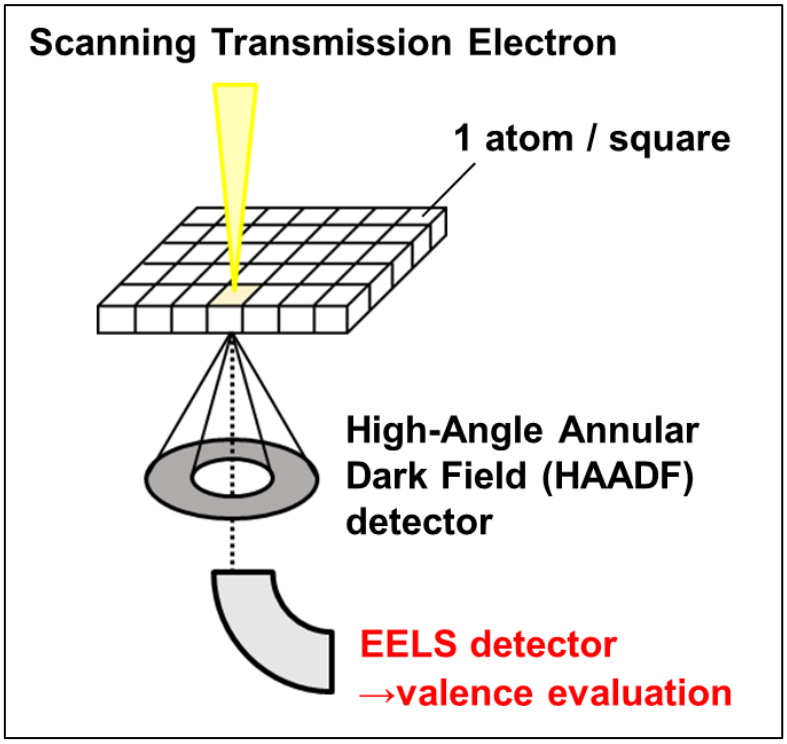

Figure 4-1. Scheme of the STEM-EELS measurements.

4.2.Experimental

4.2.1 Synthesis of Pd/c-CeO_2

To further investigate the change of Pd/CeO_2 by SO_2 treatment, morphology-controlled ceria was used as catalyst support. c-CeO_2 with an exposed (100) plane was synthesized. c-CeO_2 was prepared by hydrothermal synthesis method. $Ce(NO_3)_3$ solution was dropwise with NaOH solution, followed by hydrothermal synthesis at 200 °C for 24 h. The solid was calcined in a muffle oven at 300 °C for 5 h.

The c-CeO_2 was used as support, and $Pd(NH_3)4(NO_3)_2$ solution was used as the Pd precursor. The precursor solution was dropped into the c-CeO_2 and dried in a hot water bath. The catalyst samples were dried at 100 °C, calcined at 400 °C for 2 h, and then reduced at 200 °C for 1 h under H_2 flow.

4.2.2 Catalyst characterization

The X-ray diffraction (XRD) patterns were obtained at 40 kV and 20 mA (the step rate was 2°/min) by using a RINT 2200 diffractometer (RIGAKU, Japan) with Cu-Kα radiation (1.54 Å). Temperature-programmed reduction with H_2 (H_2-TPR) was performed using BEL-CAT (Microtrac BEL). The sample (0.10 g) was pretreated in an air flow at 350 °C for 1 h. Catalyst samples were heated from 50 °C to 950 °C at the rate of 5 °C/min. XAFS measurements were performed at Kyushu Synchrotron Light Research Center (SAGA-LS) beamline BL06 (Saga, Japan). The storage ring energy was 1.4 GeV. The double crystal monochromator Si(111) was used. Ce L_3-edge spectra were obtained with a transmission mode, and S K-edge and Pd L_3-edge spectra were obtained with a fluorescence mode. *in situ* XAFS measurements were performed in the same way as in Chapter 2.

4.2.3 STEM-EELS

STEM-EELS measurements were performed to evaluate the valence of Ce. FEI Titan G2 cubed was used for STEM-EDS and STEM-EELS measurements at an acceleration voltage of 300 kV. Figure 4-2 shows a scheme of the STEM-EELS measurements.

STEM-HAADF and STEM-EELS measurements were performed from the [011] direction. Each square has information on the loss spectrum of one row of atoms. The actual EELS spectrum obtained is shown in Figure 4-3. EELS spectrum shows peaks derived from the M_4 and M_5 edges. In a previous study [13], the intensity ratio M_4/M_5 is Ce^{4+} when the ratio is 0.9 and Ce^{3+} when the ratio is 1.25. To visualize the valence of Ce, the intensity ratio values for each spectrum are colored, as shown in Figure 4-3(e).

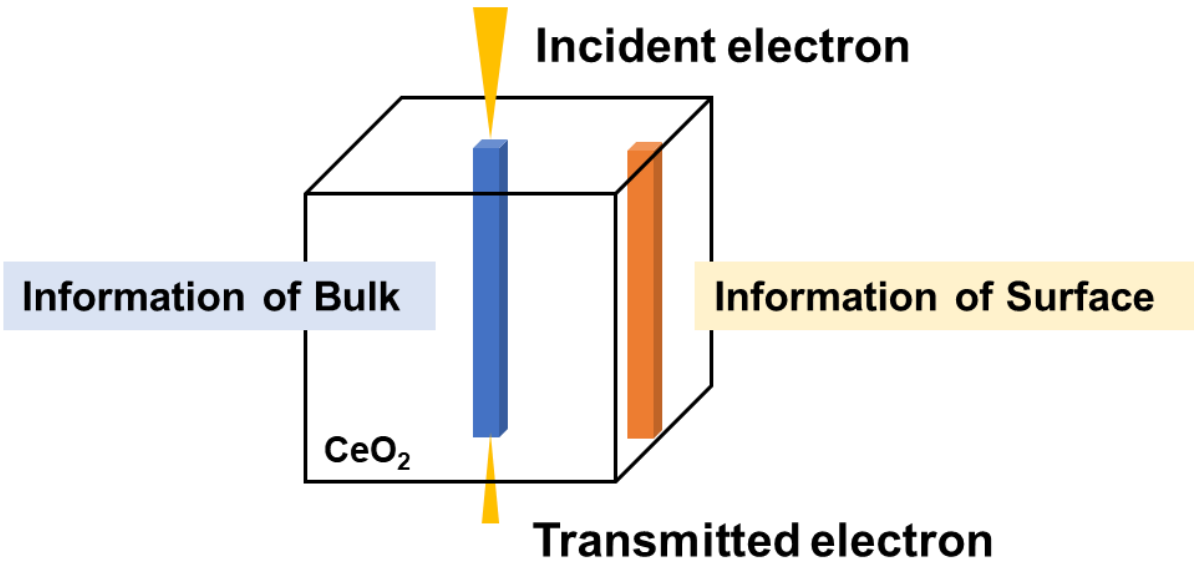

Figure 4-2. Scheme of the STEM-EELS measurements in this study.

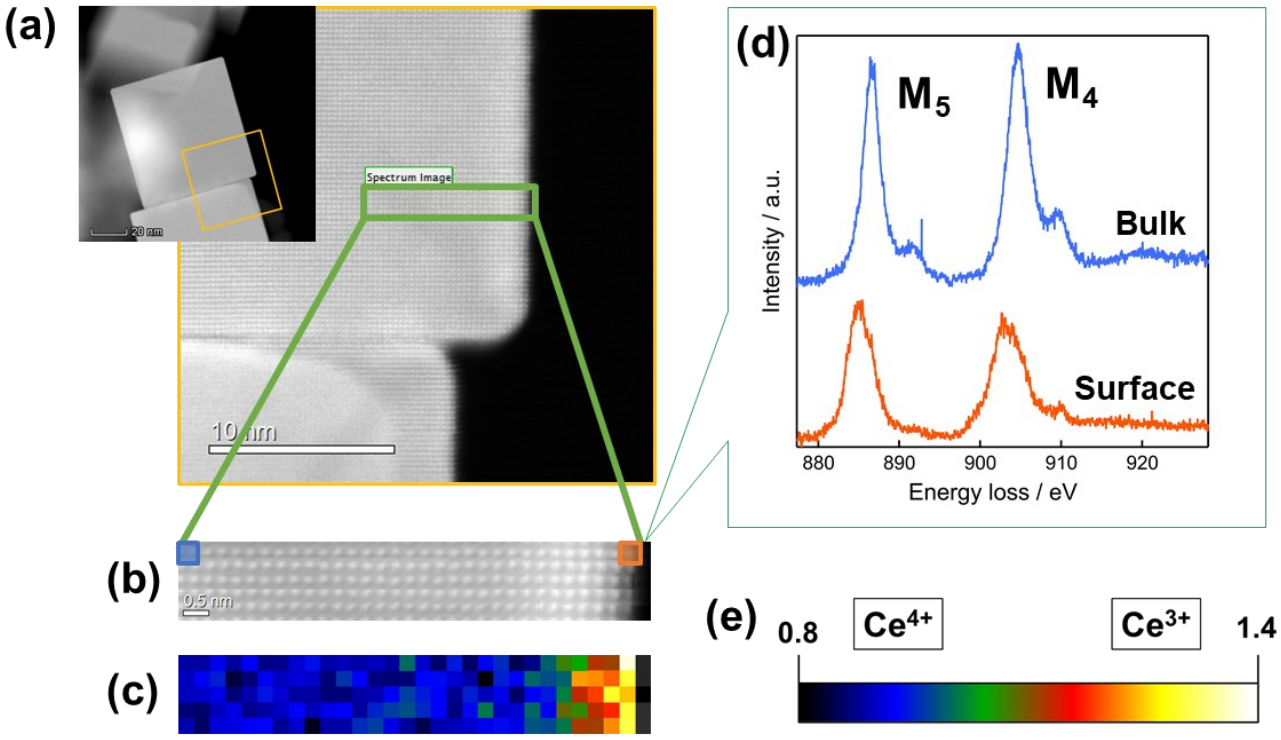

Figure 4-3. Example of STEM-EELS measurement (c-CeO_2).

(a) Low-magnification STEM-HAADF image of the measured catalyst.

(b) STEM-HAADF image of the measured area.

(c) Ce valence mapping images obtained from EELS spectra.

(d) STEM-EELS spectra of bulk side (blue) and surface side (orange).

(e) colored calculated M_5/M_4 values (0.8-1.4) of each EELS spectrum.

4.3 Results and discussion

4.3.1 Catalyst characterization

Table 4-1 shows the specific surface areas of c-CeO_2 and Pd/c-CeO_2 determined from N_2 adsorption. The surface area of c-CeO_2 is about 5% of that of the irregularly shaped reference catalyst CeO_2.

Figure 4-4 shows SEM and STEM images of the synthesized c-CeO_2. The particle size of the prepared c-CeO_2 was about 20-500 nm. STEM image of Pd/c-CeO_2 is shown in Figure 4-5, showing that the cubic structure was maintained after Pd loading. The contrast of STEM images is proportional to the atomic number (Z) [14, 15]. Pd and Ce have close atomic numbers, and the contrast difference is slight. Therefore, in the case of Pd/CeO_2 using irregularly shaped CeO_2 as a support, it was difficult to observe the supported Pd particles on CeO_2. On the other hand, Pd supported on c-CeO_2 made it possible to identify Pd in the STEM images; Pd was found to be highly dispersed on CeO_2 at about 2-5 nm.

Figure 4-6 shows the XRD patterns of c-CeO_2 and Pd/c-CeO_2 before and after SO_2 treatment. The XRD patterns of c-CeO_2 and irregular CeO_2 show peaks corresponding to fluorite-type CeO_2 [16]. XRD patterns of c-CeO_2 show sharper peaks than that of irregular CeO_2. The crystallite diameter calculated from Scherrer's formula was 9.2 nm for irregular CeO_2 and 71 nm for c-CeO_2. The crystallite diameter of c-CeO_2 increased compared to that of irregular CeO_2. No change in the XRD pattern was observed after Pd loading. Even after SO_2 treatment at 200 °C and 400 °C, the XRD patterns showed fluorite-type peaks, and no peak shift was observed. Thus, the crystal structure was not changed by SO_2 treatment, and the fluorite-type structure was maintained.

Figure 4-7 shows the H_2-TPR profile. The TPR profile of irregular CeO_2 shows two peaks on the low (200-600 °C) and high (650-950 °C) temperature side, respectively [17], originating from the reduction of surface CeO_2 and bulk CeO_2. c-CeO_2 surface reduction peaks are much decreased compared to irregular CeO_2. This finding indicates that PdO on c-CeO_2 was reduced to Pd^0 during the 50 °C keeping before measurement, H_2 was dissociatively adsorbed on Pd, and H_2 was desorbed as the temperature increased [18, 19]. The peak positions on the high-temperature side of c-CeO_2 and Pd/c-CeO_2 did not shift from irregular CeO_2. Consequently, the preparation method of CeO_2 and the loading of Pd do not affect the reduction inside CeO_2.

Table 4-1. Surface area calculated from N_2 adsorption.

	surface area / m^2g^{-1}
c-CeO_2	**6.1**
Pd/c-CeO_2	**6.5**
CeO_2	**117.8**
Pd/CeO_2	**104.9**

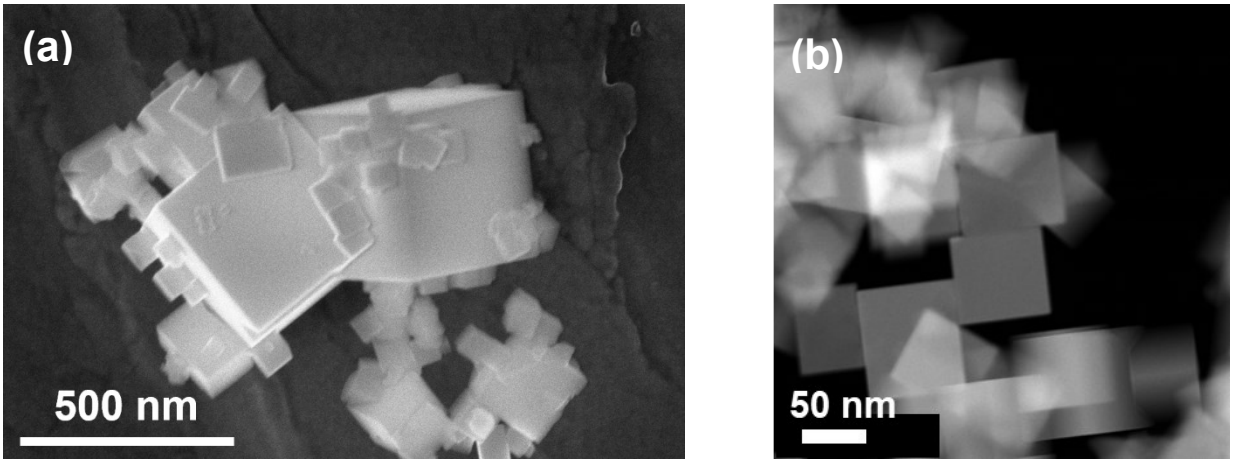

Figure 4-4. (a) SEM image of c-CeO_2; (b) STEM-HAADF image of c-CeO_2.

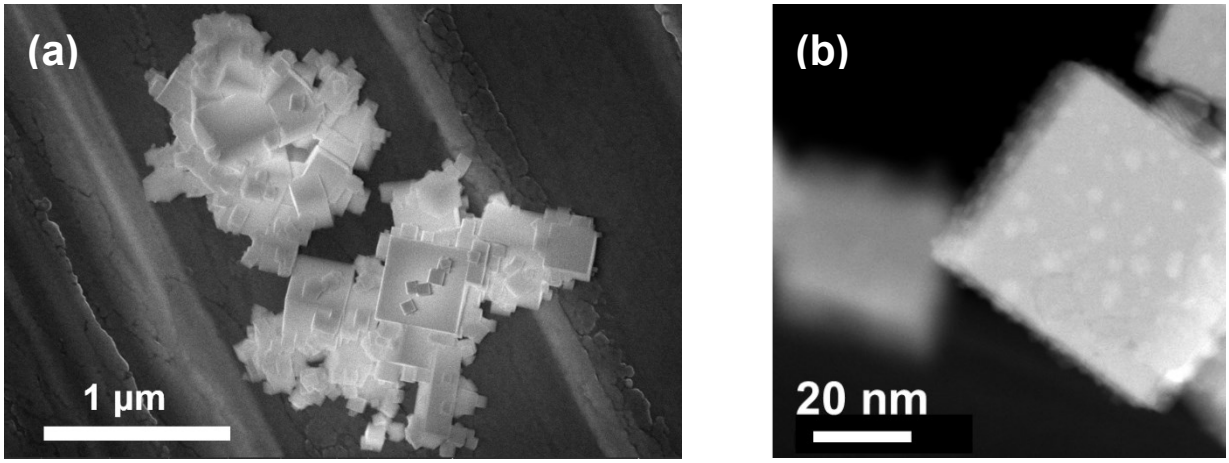

Figure 4-5. (a) SEM image of Pd/c-CeO_2; (b) STEM-HAADF image of Pd/c-CeO_2.

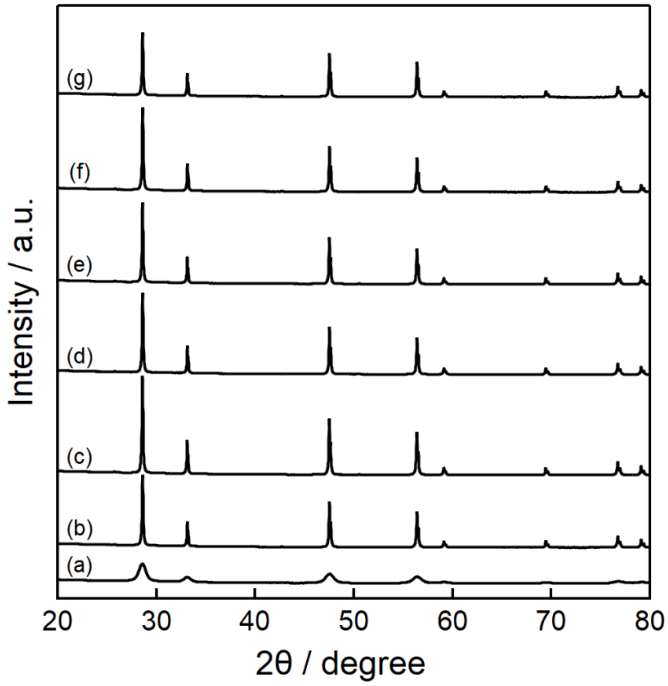

Figure 4-6. XRD patterns of (a)irregular CeO_2; (b)c-CeO_2; (c)c-CeO_2 after 400 °C 1 h SO_2 treatment; (d)Pd/c-CeO_2; (e)Pd/c-CeO_2 after 400 °C 1 h SO_2 treatment; (f)Pd/c-CeO_2 after 400 °C 5 h SO_2 treatment; (g)Pd/c-CeO_2 after 600 °C 1 h SO_2 treatment.

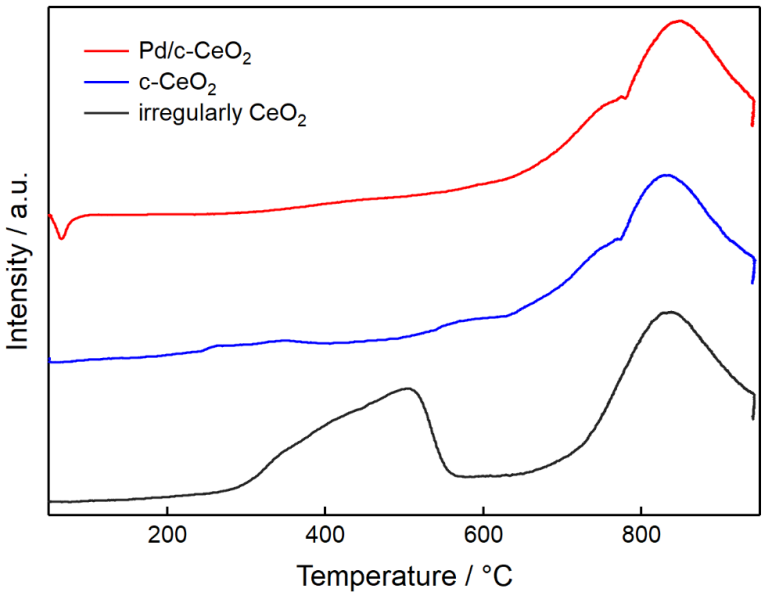

Figure 4-7. H_2-TPR profiles.

4.3.2 *in situ* XAFS measurements

Figure 4-8 shows the *in situ* Ce L_3-edge XANES spectra of c-CeO_2 at 400 °C and 500 °C under SO_2 distribution over time. Measurements were performed for 60 min in each case. The spectra of the fresh-CeO_2 show the peaks attributed to Ce $2p_{3/2}$ to $5d_{5/2, 3/2}$ electronic transitions are observed at 5730 and 5737 eV [20-22], similar to those shown in Chapter 3, indicating that Ce^{4+} is predominantly present. The XANES spectra of c-CeO_2 did not change under SO_2 distribution at 400 °C and 500 °C. Therefore, the average valence of c-CeO_2 does not change after SO_2 treatment up to 500 °C.

Figure 4-9 shows the *in situ* Ce L_3-edge XANES spectra of Pd/c-CeO_2 at 400-600 °C under SO_2 flow. The XANES spectrum of fresh-Pd/c-CeO_2 shows peaks at 5730 eV and 5737 eV, which are attributed to Ce^{4+}. The spectra of Pd/c-CeO_2 and c-CeO_2 are almost similar, indicating that Pd loading does not affect the average oxidation state of Ce in c-CeO_2. No change was observed in the XANES spectra at either 400 °C or 500 °C under SO_2 flow. Thus, the average oxidation state of the support c-CeO_2 of Pd/c-CeO_2 is not changed by SO_2 treatment up to 500 °C, as is the case with c-CeO_2. On the other hand, under SO_2 flow at 600 °C, the intensities of the peaks at 5730 eV and 5737 eV gradually decreased. The position of the absorption edge shifted to the lower energy side, and the peak according to Ce^{3+} was detected at 5726 eV. Thus, SO_2 treatment at 600 °C reduced the support c-CeO_2 of Pd/c-CeO_2.

in situ XANES spectra of irregular CeO_2 and Pd/CeO_2 with irregular support-CeO_2 showed a reduction of Ce^{4+} to Ce^{3+} under SO_2 flow at 400 °C . On the other hand, no reduction by SO_2 was observed for c-CeO_2 under SO_2 flowing at 400 °C. This result could be due to the difference in oxygen vacancy formation energy. In irregular CeO_2, various planes are exposed, and the oxygen vacancy formation energy is low. On the other hand, c-CeO_2 has a higher oxygen

vacancy formation energy than irregular CeO_2, which may explain the difference in XANES spectra.

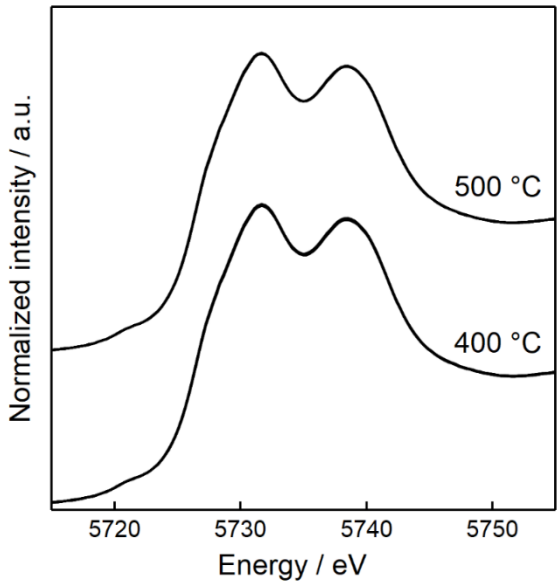

Figure 4-8. Ce L_3-XANES spectra of c-CeO_2 under SO_2 flow at 400 °C and 500 °C.
Measuring time = 0, 20, 40, 60 min.

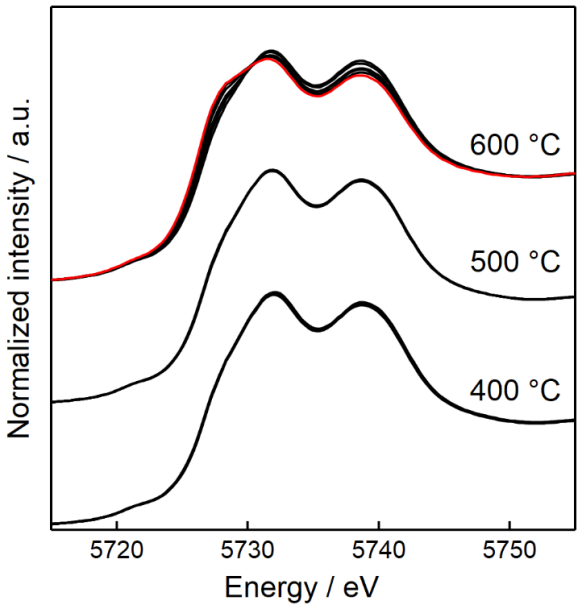

Figure 4-9. Ce L_3-XANES spectra of Pd/c-CeO_2 under SO_2 flow at 400-600 °C.
Measuring time = 0, 20, 40, 60 min.
Red line: under O_2 flow after SO_2 treatment.

4.3.3 STEM-EELS measurements

Figures 4-10 show STEM-HAADF images and Ce valence mapping images obtained from EELS spectra of Pd/c-CeO_2. The mapping image indicates that the bulk of c-CeO_2 is Ce^{4+}. This result agrees with the Ce L_3-edge XANES measurements. One layer on the surface of CeO_2 was Ce^{3+}. The surface from the 2 to 5 layer is between Ce^{3+} and Ce^{4+}, which is the region where the oxygen vacancies exist. Thus, 5 layers of oxygen vacancies form from the surface. The same method was used to quantify the oxygen vacancies in Pd/c-CeO_2. Figure 4-14 shows the number of oxygen vacancies calculated from the Ce valence mapping image versus the particle size of the support c-CeO_2. The fresh Pd/c-CeO_2 has 2-15 layers of oxygen vacancies from the surface. There is no correlation between the grain size of c-CeO_2 and the number of oxygen vacancies.

STEM-EDS measurements were performed to investigate the structural changes of Pd/c-CeO_2 after SO_2 treatment (Figure 4-11). After SO_2 treatment at 200 °C and 400 °C, the supported c-CeO_2 was found to maintain its cube structure. Elemental mapping by EDS revealed that sulfur species after SO_2 treatment were not localized around Pd but were present on the entire catalyst surface.

Figure 4-12 shows STEM-HAADF and Ce valence mapping images of Pd/c-CeO_2 after SO_2 treatment at 200 °C. The mapping images show that the bulk of CeO_2 is Ce^{4+} even after SO_2 treatment at 200 °C. The number of oxygen vacancies present was 2-15 layers for most of the particles. Therefore, SO_2 treatment at 200 °C did not decrease the c-CeO_2 support nor increase the oxygen vacancies.

Figure 4-13 shows STEM-HAADF images of Pd/c-CeO_2 after SO_2 treatment at 400 °C. Oxygen vacancies are present in about 15 layers from the surface, which is an increase compared to fresh Pd/c-CeO_2. Figure 4-14 shows that SO_2 treatment at 400 °C tends to increase the number of oxygen vacancies. As in the case of the fresh catalyst, there was no correlation

between the oxygen vacancies and the particle size of c-CeO_2 after sulfurization. *in situ* XANES measurements showed no change in the valence of Pd/c-CeO_2 under SO_2 distribution at 400 °C. On the other hand, STEM-EELS measurements revealed that c-CeO_2 was reduced by 400 °C SO_2 treatment. This could be because the reduction of c-CeO_2 occurred in a narrow region within 20 layers from the surface, and the average oxidation number of c-CeO_2 remained Ce^{4+}.

After SO_2 treatment at 400 °C, the distribution of oxygen vacancies on c-CeO_2 varied. To investigate this reason, the number of oxygen vacancies at the Pd-CeO_2 interface and on the Pd-free CeO_2 surface were compared. Figures 4-16 and 4-17 show STEM-HADF image and Ce valence mapping images obtained from s and EELS spectra of fresh-Pd/c-CeO_2 and Pd/c-CeO_2 after 400 °C SO_2 treatment, respectively. Figure 4-16 shows that in the fresh catalyst, both the Pd-CeO_2 interface and the c-CeO_2 surface showed 3-4 layers of oxygen vacancies from the surface. After SO_2 treatment at 400 °C, the c-CeO_2 surface had about 13 layers of oxygen vacancies in the Ce mapping image. On the other hand, about 16 layers of oxygen vacancies existed at the Pd-c-CeO_2 interface, forming more oxygen vacancies than at the c-CeO_2 surface. The Pd-c-CeO_2 interface tends to be more easily reduced than the surface. These results revealed that the Pd-CeO_2 interaction could promote CeO_2 reduction.

The oxygen vacancies calculated from the Ce valence mapping image versus particle size of c-CeO_2 and c-CeO_2 after 400 °C SO_2 treatment are shown in Figure 4-15. In contrast to Pd/c-CeO_2, no tendency for an increase in oxygen vacancies was observed after SO_2 treatment at 400 °C. This tendency indicates that the Pd loading may have promoted the reduction of the supported CeO_2 by SO_2 treatment. Pd-CeO_2 interfacial interactions affect the reduction of CeO_2 by SO_2.

Some researchers have discussed the interactions at the Pd-CeO_2 interface. Yang et al. reported that the oxygen vacancy formation energy is lower at the Pd-CeO_2 interface than at the

fresh-CeO_2 surface [23]. They explain that this is due to the Pd-CeO_2 interaction, which induces MIGS and facilitates reduction. It has also been reported that Pd loading distorts the CeO_2 structure and increases the bond length of Ce-O bonds near the Pd-CeO_2 interface [24]. This facilitates the cleavage of Ce-O bonds and improves the reactivity of lattice oxygen. Therefore, the electronic interaction between Pd and CeO_2 and the distortion of the CeO_2 structure due to Pd loading could promote the reduction of SO_2 at the Pd-CeO_2 interface.

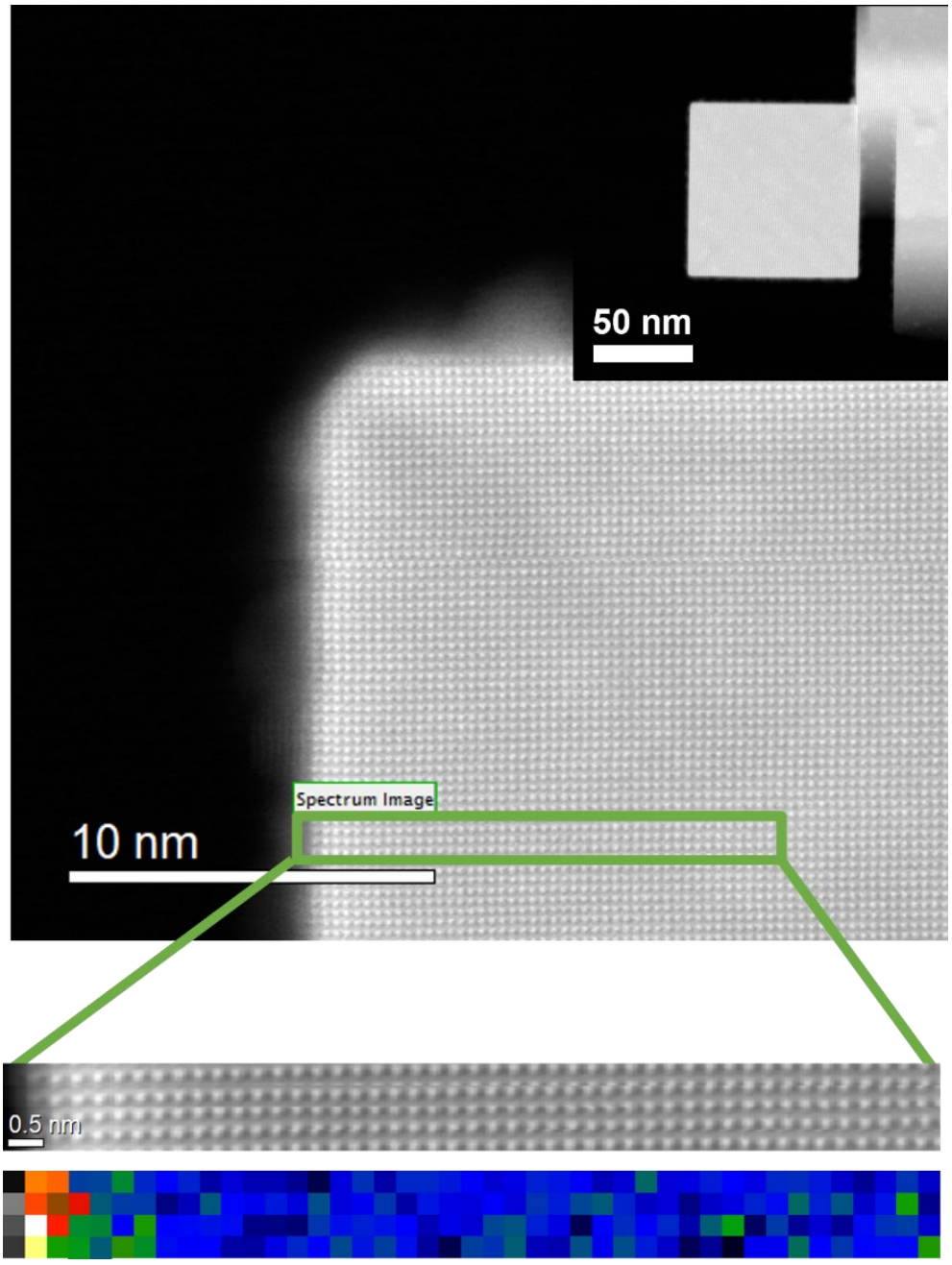

Figure 4-10. STEM-HAADF images, and Ce valence mapping images obtained from EELS spectra of Pd/c-CeO_2.

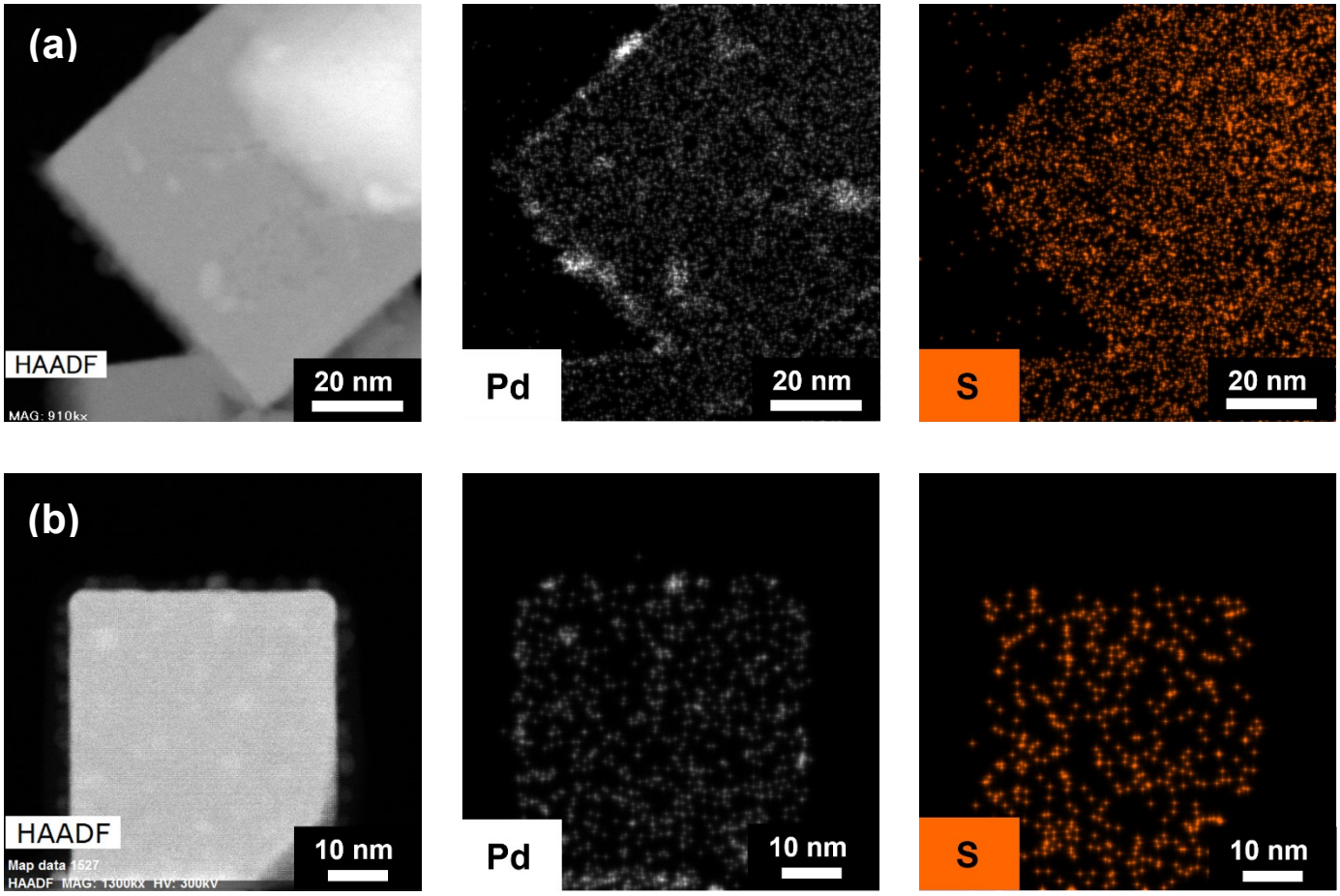

Figure 4-11. STEM-EDS image of (a)Pd/c-CeO_2 after SO_2 treatment at 200 °C (b)Pd/CeO_2 after SO_2 treatment at 400 °C.

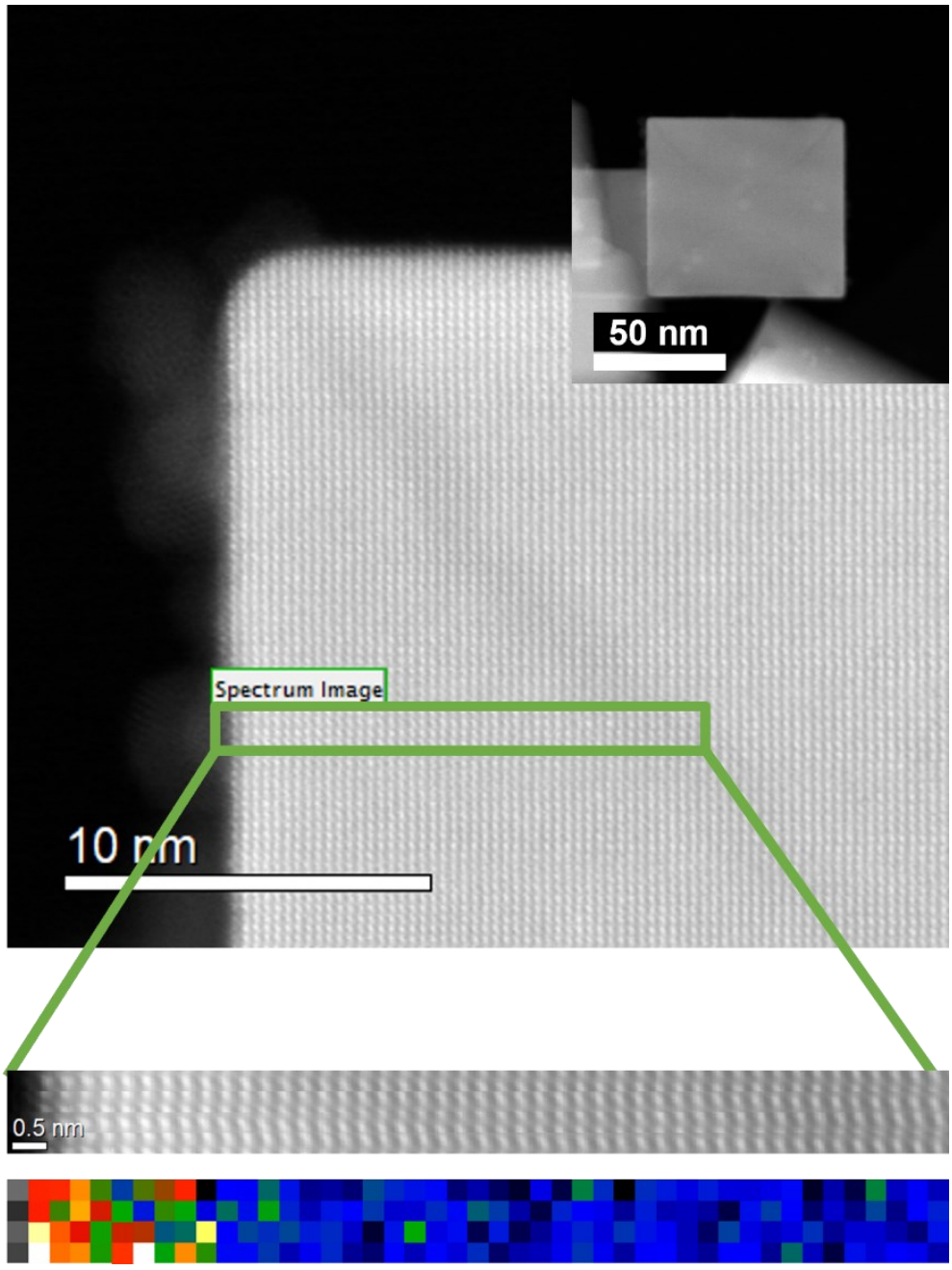

Figure 4-12. STEM-HAADF images and Ce valence mapping images obtained from EELS spectra of Pd/c-CeO_2 after SO_2 treatment at 200 °C for 1 h.

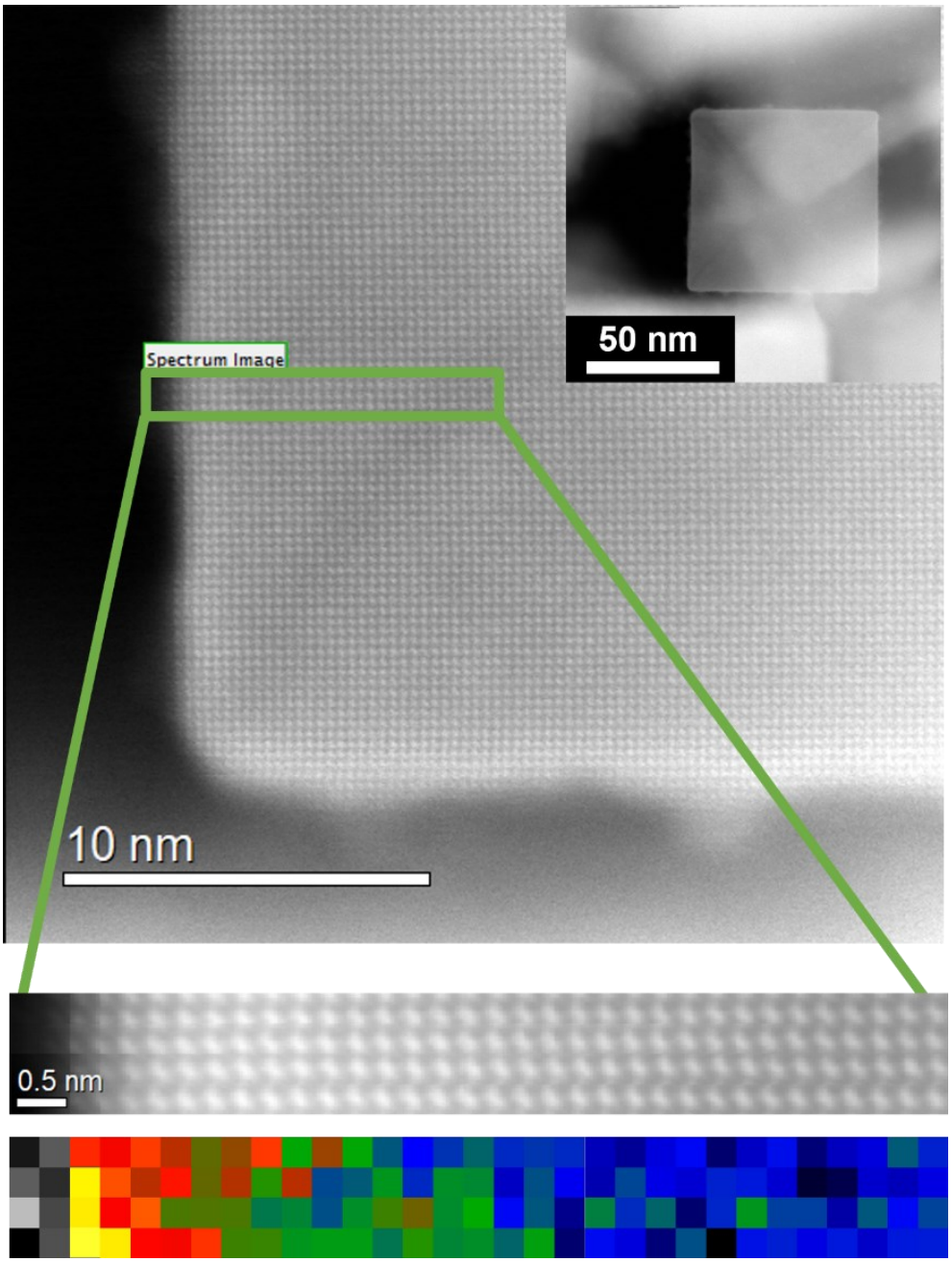

Figure 4-13. STEM-HAADF images, and Ce valence mapping images obtained from EELS spectra of Pd/c-CeO_2 after SO_2 treatment at 400 °C for 1 h.

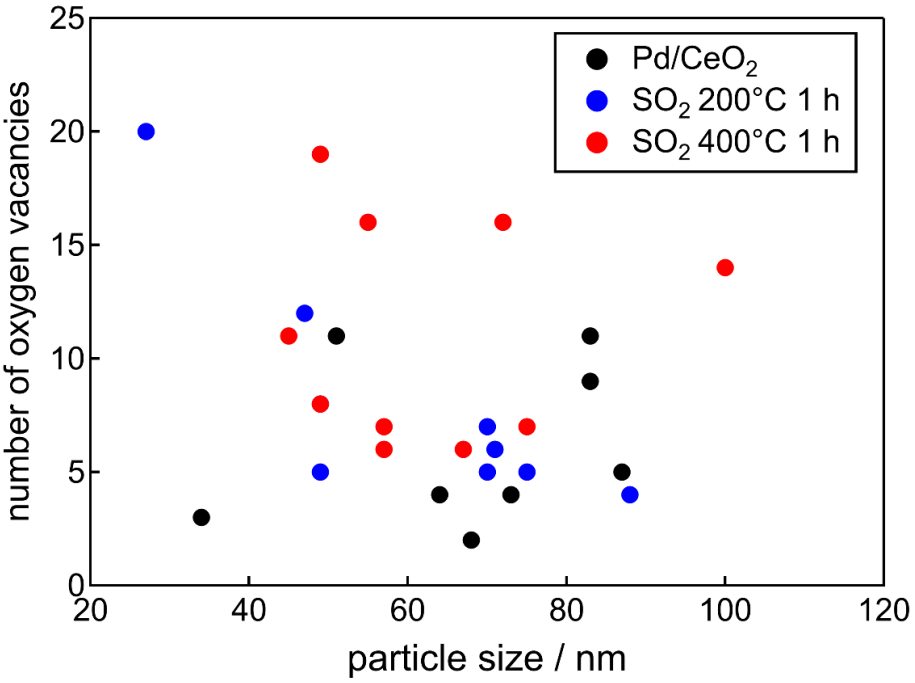

Figure 4-14. Number of oxygen vacancies versus of Pd/c-CeO_2 the particle size of the support c-CeO_2.

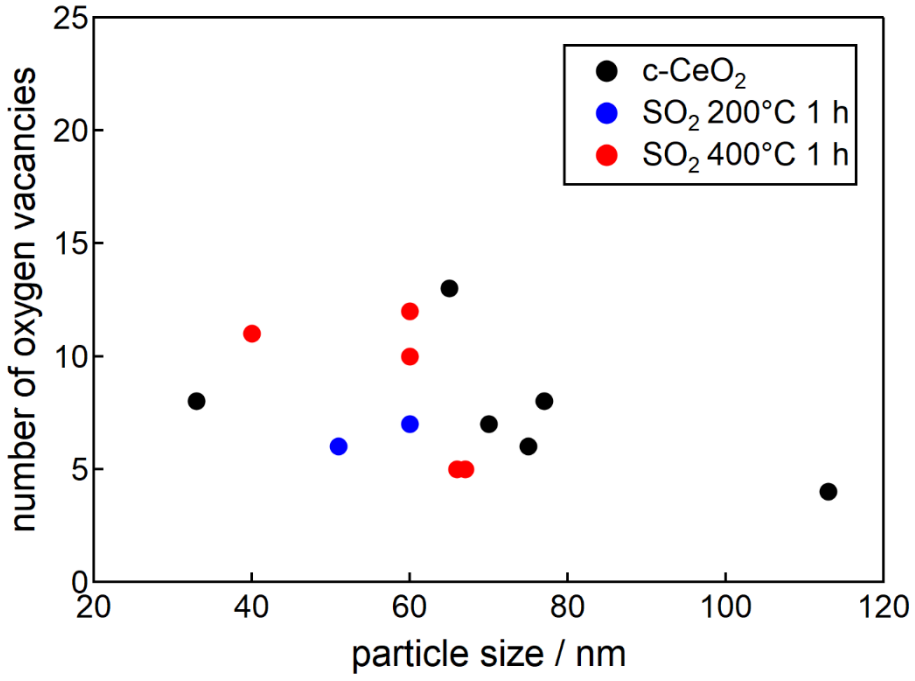

Figure 4-15. Number of oxygen vacancies versus of c-CeO_2 the particle size of the c-CeO_2.

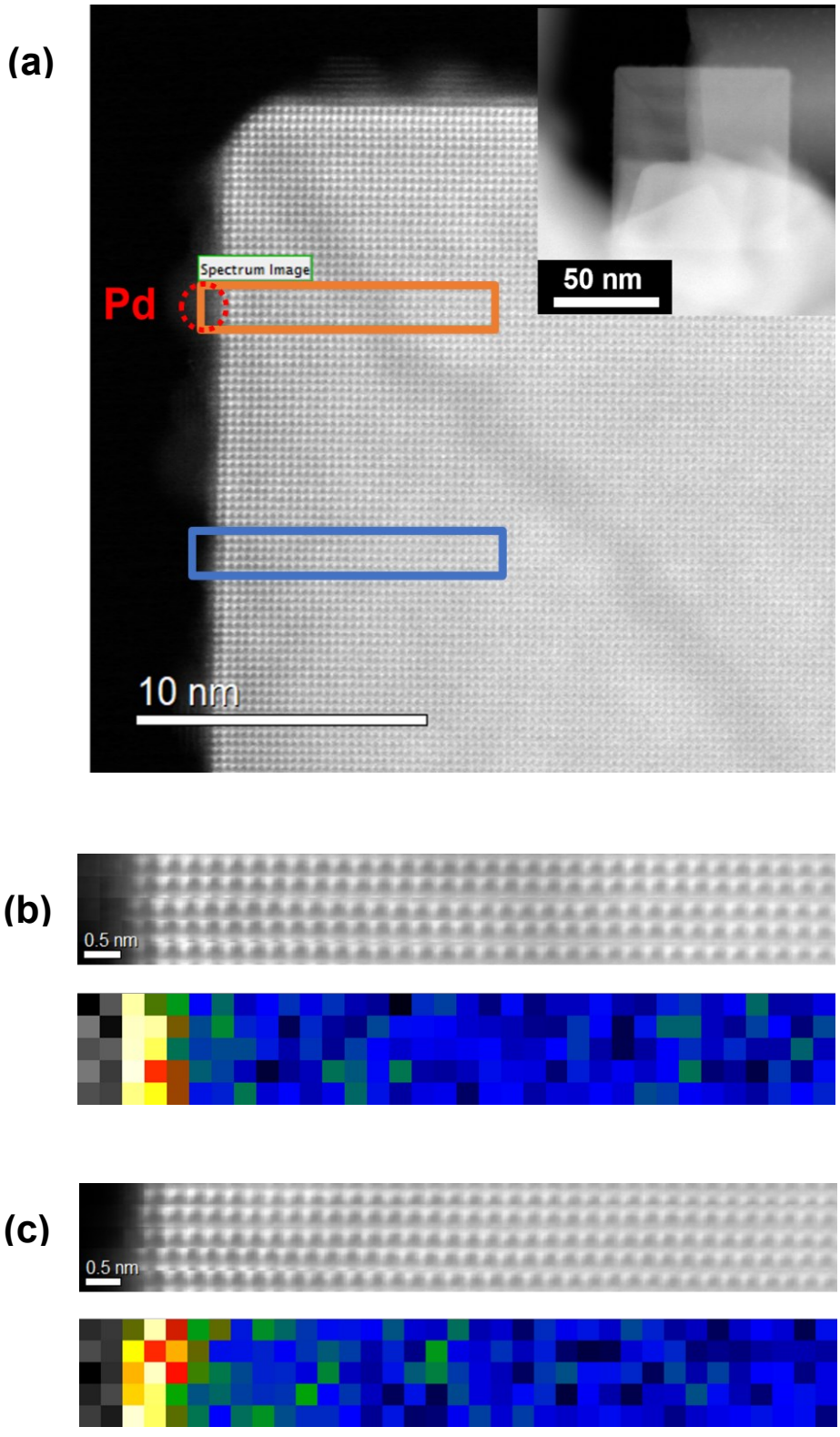

Figure 4-16. (a) STEM-HAADF images of Pd/c-CeO_2.

Ce valence mapping images obtained from EELS spectra of Pd/c-CeO_2 at (b)Pd-CeO_2 interface and (c)CeO_2 surface.

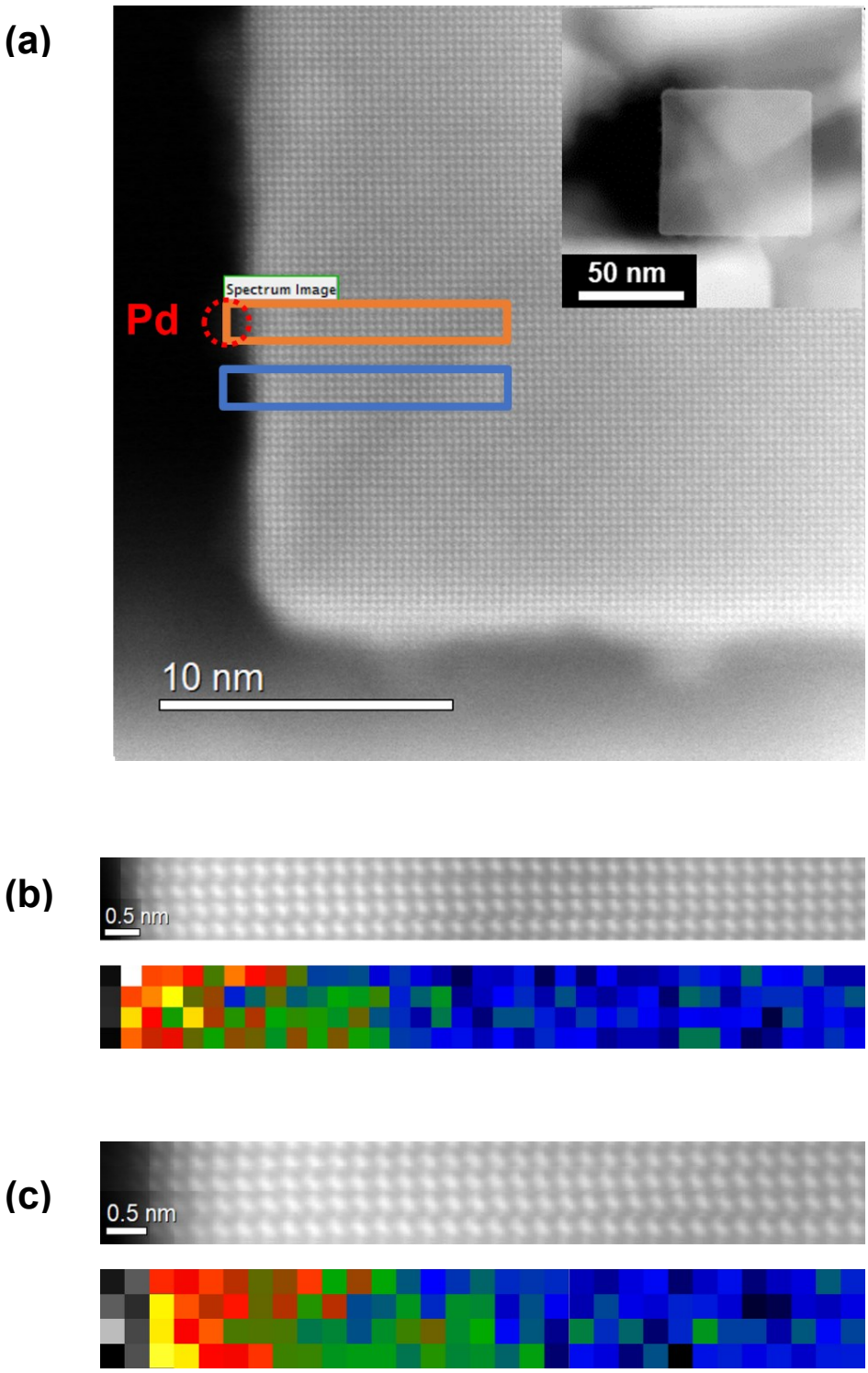

Figure 4-17. (a) STEM-HAADF images of Pd/c-CeO_2 after SO_2 treatment at 400 °C for 1 h. Ce valence mapping images obtained from EELS spectra of Pd/c-CeO_2 after SO_2 treatment at 400 °C for 1 h at (b)Pd-CeO_2 interface and (c)CeO_2 surface.

4.4 Conclusion

In this chapter, to understand the structural changes of Pd/CeO_2 induced by SO_2, morphology-controlled c-CeO_2 was prepared and analyzed in detail using STEM-EELS. Compared to irregular CeO_2, c-CeO_2 had a smaller specific surface area and lower surface reduction properties. Pd was highly dispersed on c-CeO_2. Therefore, the Pd loading did not change the structure of c-CeO_2. *in situ* XAFS measurements revealed that Pd/c-CeO_2 was reduced by SO_2 treatment above 600 °C. STEM-EDS measurements showed that sulfur species formed by SO_2 treatment were present in the entire Pd/c-CeO_2. STEM-EELS measurements revealed that SO_2 treatment at 200 °C did not change the structure of the support CeO_2, while SO_2 treatment at 400 °C reduced the support CeO_2 and increased the number of oxygen vacancies. I revealed that the Pd-CeO2 interface was reduced more than the surface. Therefore, Pd loading could promote the reduction of the supported CeO_2 by SO_2 treatment.

References

[1] Zhou, K.; Wang, X.; Sun, X.; Peng, Q.; Li, Y. Enhanced Catalytic Activity of Ceria Nanorods from Well-Defined Reactive Crystal Planes. *J. Catal.* **2005**, *229* (1), 206–212.

[2] Mai, H.-X.; Sun, L.-D.; Zhang, Y.-W.; Si, R.; Feng, W.; Zhang, H.-P.; Liu, H.-C.; Yan, C.-H. Shape-Selective Synthesis and Oxygen Storage Behavior of Ceria Nanopolyhedra, Nanorods, and Nanocubes. *J. Phys. Chem. B* **2005**, *109* (51), 24380–24385.

[3] Yan, L.; Yu, R.; Chen, J.; Xing, X. Template-Free Hydrothermal Synthesis of CeO_2 Nano-Octahedrons and Nanorods: Investigation of the Morphology Evolution. *Cryst. Growth Des.* **2008**, *8* (5), 1474–1477.

[4] Gao, Y.; Li, R.; Chen, S.; Luo, L.; Cao, T.; Huang, W. Morphology-Dependent Interplay of Reduction Behaviors, Oxygen Vacancies and Hydroxyl Reactivity of CeO_2 Nanocrystals. *Phys. Chem. Chem. Phys.* **2015**, *17* (47), 31862–31871.

[5] Liu, L.; Yao, Z.; Deng, Y.; Gao, F.; Liu, B.; Dong, L. Morphology and Crystal-Plane Effects of Nanoscale Ceria on the Activity of CuO/CeO_2 for NO Reduction by CO. *ChemCatChem* **2011**, *3* (6), 978–989.

[6] Tan, H.; Wang, J.; Yu, S.; Zhou, K. Support Morphology-Dependent Catalytic Activity of Pd/CeO_2 for Formaldehyde Oxidation. *Environ. Sci. Technol.* **2015**, *49* (14), 8675–8682.

[7] Tumuluri, U.; Li, M.; Cook, B. G.; Sumpter, B.; Dai, S.; Wu, Z. Surface Structure Dependence of SO_2 Interaction with Ceria Nanocrystals with Well-Defined Surface Facets. *J. Phys. Chem. C* **2015**, *119* (52), 28895–28905.

[8] Hu, Z.; Liu, X.; Meng, D.; Guo, Y.; Guo, Y.; Lu, G. Effect of Ceria Crystal Plane on the Physicochemical and Catalytic Properties of Pd/Ceria for CO and Propane Oxidation. *ACS Catal.* **2016**, *6* (4), 2265–2279.

[9] Kropp, T.; Paier, J.; Sauer, J. Interactions of Water with the (111) and (100) Surfaces of Ceria. *J. Phys. Chem. C* **2017**, *121* (39), 21571–21578.

[10] Spezzati, G.; Benavidez, A. D.; DeLaRiva, A. T.; Su, Y.; Hofmann, J. P.; Asahina, S.; Olivier, E. J.; Neethling, J. H.; Miller, J. T.; Datye, A. K.; Hensen, E. J. M. CO Oxidation by Pd Supported on $CeO_2(100)$ and $CeO_2(111)$ Facets. *Appl. Catal. B* **2019**, *243*, 36–46.

[11] Li, J.; Liu, Z.; Cullen, D. A.; Hu, W.; Huang, J.; Yao, L.; Peng, Z.; Liao, P.; Wang, R. Distribution and Valence State of Ru Species on CeO_2 Supports: Support Shape Effect and Its Influence on CO Oxidation. *ACS Catal.* **2019**, *9* (12), 11088–11103.

[12] Jiang, F.; Wang, S.; Liu, B.; Liu, J.; Wang, L.; Xiao, Y.; Xu, Y.; Liu, X. Insights into the Influence of CeO_2 Crystal Facet on CO_2 Hydrogenation to Methanol over Pd/CeO_2 Catalysts. *ACS Catal.* **2020**, *10* (19), 11493–11509.

[13] Hojo, H.; Mizoguchi, T.; Ohta, H.; Findlay, S. D.; Shibata, N.; Yamamoto, T.; Ikuhara, Y. Atomic Structure of a CeO_2 Grain Boundary: The Role of Oxygen Vacancies. *Nano Lett.* **2010**, *10* (11), 4668–4672.

[14] Crewe, A. V. High Resolution Scanning Microscopy of Biological Specimens. *Philos. Trans. R. Soc. Lond. B Biol. Sci.* **1971**, *261* (837), 61–70.

[15] Pennycook, S. J. Z-Contrast Stem for Materials Science. *Ultramicroscopy* **1989**, *30* (1), 58–69.

[16] Xu, Y.; Yamazaki, M.; Villars, P. Inorganic Materials Database for Exploring the Nature of Material. *Jpn. J. Appl. Phys.* **2011**, *50* (11S), 11RH02.

[17] Leitenburg, C. de; Trovarelli, A.; Kašpar, J. A Temperature-Programmed and Transient Kinetic Study of CO_2 Activation and Methanation over CeO_2Supported Noble Metals. *J. Catal.* **1997**, *166* (1), 98–107.

[18] Bhogeswararao, S.; Srinivas, D. Catalytic Conversion of Furfural to Industrial Chemicals over Supported Pt and Pd Catalysts. *J. Catal.* **2015**, *327*, 65–77.

[19] Centi, G. Supported Palladium Catalysts in Environmental Catalytic Technologies for Gaseous Emissions. *J. Mol. Catal. A Chem.* **2001**, *173* (1), 287–312.

[20] Soldatov, A. V.; Ivanchenko, T. S.; Della Longa, S.; Kotani, A.; Iwamoto, Y.; Bianconi, A. Crystal-Structure Effects in the Ce L_3-Edge X-Ray-Absorption Spectrum of CeO_2: Multiple-Scattering Resonances and Many-Body Final States. *Phys. Rev. B: Condens. Matter Mater. Phys.* **1994**, *50* (8), 5074.

[21] Nachimuthu, P.; Shih, W.-C.; Liu, R.-S.; Jang, L.-Y.; Chen, J.-M. The Study of Nanocrystalline Cerium Oxide by X-Ray Absorption Spectroscopy. *J. Solid State Chem.* **2000**, *149* (2), 408–413.

[22] Dexpert, H.; Karnatak, R. C.; Esteva, J.-M.; Connerade, J. P.; Gasgnier, M.; Caro, P. E.; Albert, L. X-Ray Absorption Studies of CeO_2, PrO_2, and TbO_2. II. Rare-Earth Valence State by L III absorption Edges. *Phys. Rev. B Condens. Matter* **1987**, *36* (3), 1750–1753.

[23] Centi, G. Supported Palladium Catalysts in Environmental Catalytic Technologies for Gaseous Emissions. *J. Mol. Catal. A Chem.* **2001**, *173* (1), 287–312.

[24] Bhogeswararao, S.; Srinivas, D. Catalytic Conversion of Furfural to Industrial Chemicals over Supported Pt and Pd Catalysts. *J. Catal.* **2015**, *327*, 65–77.

Chapter 5 Effect of Cu addition of CeO_2-supported Pd catalyst on catalytic oxidation of CO to CO_2 under dilute O_2 condition

5.1 Introduction

The addition of other elements is effective in improving the activity of Pd catalysts. To date, CO oxidation of Pd-only loaded Pd/CeO_2 has been extensively studied [1-6]. In this study, this topic was also investigated in Chapter 1. The addition of transition metals effectively improves the activity of Pd catalysts. For example, Pd-Au [7-10], Pd-Zn [11-15], Pd-Mo [16-18], and Pd-Cu catalysts [19-27] have been reported to exhibit higher activity than Pd catalysts. The addition of transition metals changes the electronic state of Pd and improves its dispersion, which in turn alters the reactivity of the substrate, resulting in increased activity.

Pd-Cu catalysts have been extensively studied because Cu is an inexpensive material with excellent redox properties. Wacker catalysts have been studied as homogeneous catalysts (ref), and heterogeneous catalysts have also been studied in many reactions [27]. In supported Pd-Cu catalysts, the formation of the Pd-Cu alloy structure results in lower reduction temperatures and higher catalytic activity of the Pd catalyst [19-26]. Both Pd/CeO_2 and Cu/CeO_2 show high CO oxidation activity in CO oxidation. Therefore, the CO oxidation activity is expected to be improved even when the alloy structure is not formed.

In this chapter, the effect of Cu on the catalytic CO oxidation of Pd-Cu catalysts in which the alloy structure is not formed is discussed. I report the structural and catalytic properties of $Pd\text{-}Cu/CeO_2$ with different loadings and compare them with those of other supported catalysts. The catalysts were characterized by X-ray diffraction (XRD), X-ray Absorption Near Edge Structure (XANES), Extended X-ray Absorption Fine Structure (EXAFS), High-Resolution

Transmission Electron Microscopy (HR-TEM), Scanning Transmission Electron Microscopy-High-Angle Annular Dark Field (STEM-HAADF), diffuse reflectance Fourier Transform Infrared Spectroscopy (FTIR), and H_2-Temperature Programmed Reduction (TPR) studies. The catalytic performance of Pd-Cu/CeO_2 was evaluated at 90-150 °C under dilute oxygen conditions ([O_2]/[CO] = 0.5). The efficacy of the Cu addition to Pd/CeO_2 for CO oxidation was discussed in detail.

5.2 Experimental

5.2.1 Catalyst preparation

Supported Pd-Cu catalysts (Pd-Cu/TiO_2, Pd-Cu/Al_2O_3, Pd-Cu/CeO_2) were prepared by impregnation methods. Catalyst supports (TiO_2: JRC-TIO-4(2), Al_2O_3: JRC-ALO-8, CeO_2: JRC-CEO-5) were obtained from the Catalysis Society of Japan. $Pd(NH_3)_4(NO_3)_2$ (Sigma-Aldrich Co., Ltd.) and $Cu(CH_3COO)_2$▪H_2O (Wako Pure Chemical Industries, Ltd.) were used as metal precursors for the catalysts. The aqueous precursor containing these materials was dropped into the catalyst support powder and then dried in a hot water bath. The catalyst samples were dried at 100 °C, calcined at 400 °C for 2 h in the air, and then reduced at 200 °C for 1 h under H_2 flow. The Pd loading was set to 1 wt%. For the Pd-Cu/CeO_2 preparation, after impregnation with Pd precursor solution and drying at 60 °C, Cu precursor solution was impregnated and dried at 100 °C. The Pd-Cu/CeO_2 was then dried at 100 °C. Care should be taken when mixing Pd and Cu precursors in an aqueous solution since Cu^{2+} precipitates as $Cu(OH)_2$ under basic conditions. Moreover, the isoelectric point of CeO_2 is 6.7-8.6; therefore, maintaining the basicity of the Pd-containing solution is necessary to fix $Pd(NH_3)_4^{2+}$ on the CeO_2 surface. To investigate the effect of Cu loading amount, the molar ratio of Cu to Pd was changed from 1 to 10 and denoted as Pd-Cu(1)/CeO_2, Pd-Cu(2)/CeO_2, Pd-Cu(5)/CeO_2, and Pd-Cu(10)/CeO_2.

5.2.2 Catalyst characterization

XRD patterns were obtained using a RIGAKU RINT 2200 instrument with Cu-Kα radiation at 40 kV and 20 mA. STEM observations and energy dispersive spectroscopy (EDS) elemental mapping were performed using Titan G2 cubed (Gatan). XANES and EXAFS spectra were obtained at Kyushu Synchrotron Light Research Center (SAGA-LS). EXAFS spectra of the Pd K-edge were collected in the transmission mode; XANES spectra of the Pd L_3-edge were

collected in fluorescence mode. Fourier transform EXAFS spectra were obtained from k^3-weighted EXAFS data at 3.0-13.0 Å. FTIR studies were performed using an FTIR-4100 (Jasco) with diffuse reflection accessory with KBr window. Prior to measurements, samples were heated to 300 °C in a He flow. Spectra were collected at 80 °C with a resolution of 4 cm^{-1}. Temperature-programmed reduction with H_2 (H_2-TPR) was conducted with a BEL-CAT (MicrotracBEL). The catalyst was pretreated under O_2 flow for 1 h at 350 °C. In the H_2-TPR measurements, the catalyst was heated from 50 °C to 950 °C at 5 °C/min.

5.3 Results and discussion

5.3.1 Structures of Pd particles on the supporting materials

XRD patterns of the supported Pd/CeO_2 and $Pd\text{-}Cu/CeO_2$ catalysts (Figure 5-1). The patterns of the catalysts show peaks attribute to the fluorite structure of CeO_2. The XRD pattern of the Pd/CeO_2 catalyst is almost the same as that of the support (CeO_2), showing that the structure of the support has not changed after Pd deposition, followed by oxidation and H_2 reduction in the catalyst preparation. Diffraction peaks of Pd and PdO were not detected in Pd/CeO_2, indicating that the Pd species were highly dispersed on the CeO_2. In addition, the XRD pattern of $Pd\text{-}Cu/CeO_2$ hardly changed when the Cu loading was changed, indicating that the Cu loading did not affect the support structure. Pd, PdO, and CuO diffraction peaks were not detected, and these particles on CeO_2 were less than 30 nm. In the XRD pattern of Cu/CeO_2, only the CeO_2 peak was also detected, and no CuO peak was detected.

Pd K-edge XANES and EXAFS spectra of Pd/CeO_2 and $Pd\text{-}Cu/CeO_2$ are shown in Figure 5-2. The Pd K-edge spectra of the catalysts showed a peak at 24.4 keV, which was attributed to the transition from the 1s to 5p orbital. After the addition of Cu, the spectra did not change significantly (Figure 5-2(a)). In the EXAFS spectra (Figure 5-2(b)). The spectra of both catalysts showed peaks at 1.6 Å and 3.0 Å, which were attributed to the Pd-O bond and Pd-(O)-Pd bond, respectively. For the $Pd\text{-}Cu/CeO_2$ catalyst, the peak intensities for the Pd-O bond and Pd-(O)-Pd bond were smaller than that of the Pd/CeO_2 catalyst. Table 5-1 shows the fitted parameters of Pd catalysts from Pd K-edge EXAFS. The coordination number for the $Pd\text{-}Cu/CeO_2$ catalyst is lower than that for the Pd/CeO_2 catalyst, indicating that the size of the PdO particles on the CeO_2 decreased with Cu addition. Some research shows that the codeposition of Pd and Cu on CeO_2 forms a Pd-Cu alloy. Fox et al. reported that the EXAFS spectra of the Pd-Cu bimetallic catalyst showed a peak at approximately 2.2 Å; this peak was attributed to the

Pd-Cu bond [24]. On the other hand, no such peaks were observed for the Pd-Cu/CeO_2 catalyst used in this study. The Pd K-edge spectrum of the Pd-Cu/CeO_2 catalyst was well-fitted by the Pd-O and Pd-O-Pd contributions, indicating that only PdO species were formed in the catalyst (Figure 5-2(c)).

Pd L_3-edge XANES spectra of Pd-Cu/CeO_2 and Pd/CeO_2 are shown in Figure 5-3. In the spectra of Pd-Cu/CeO_2 and Pd/CeO_2, a peak at 3174.4 eV was observed, which is attributed to the transition from the 2p to the 4d orbital. The XANES spectra of Pd-Cu/CeO_2 and Pd/CeO_2 were almost identical. Moreover, the Pd K-edge XANES spectra after Cu loading showed no significant change compared to the spectra before loading, indicating that the addition of Cu did not affect the oxidation state of Pd on CeO_2.

Figure 5-4 shows HR-TEM images of Pd/CeO_2 and Pd-Cu(1)/CeO_2. The HR-TEM image of Pd/CeO_2 showed Pd particles of approximately 3 nm on the CeO_2. In the image of Pd-Cu(1)/CeO_2, Pd particles and Cu particles were not observed. This result indicates that the particle size of PdO on CeO_2 decreased with the addition of Cu, which agrees with the results of the XAFS studies. STEM-EDS images of Pd/CeO_2, Pd-Cu(1)/CeO_2, Pd-Cu(5)/CeO_2, Pd-Cu(10)/CeO_2, and Cu/CeO_2 are shown in Figure 5-5. The EDS images of Pd/CeO_2 show that the Pd particles were distributed uniformly over the entire CeO_2. STEM-EDS images of Cu/CeO_2 also show that CuO was highly dispersed on CeO_2. The images of Pd-Cu(1)/CeO_2 also show that the Pd and Cu particles were highly distributed on the CeO_2, and the particle size was 2-3 nm. In contrast, the Pd particle size increased to about 5-10 nm in Pd-Cu(10)/CeO_2. Thus, excessive Cu loading was found to increase the Pd particle size.

XPS measurements were performed to investigate the oxidation state of Cu. XPS spectra of Cu 2p used to study the oxidation state of Cu species on CeO_2 are shown in Figure 5-6. In Pd-Cu(10)/CeO_2, sufficient peaks to evaluate the oxidation state were not obtained. This is due to

the low Cu loading. The Pd-Cu(10)/CeO_2 spectrum shows peaks corresponding to Cu^{2+} at about 933.8 eV and 953.8 eV and satellite peaks corresponding to CuO at about 942 eV and 962 eV, indicating that the Cu species of Pd-Cu(10)/CeO_2 was CuO.

Table 5-1. Fitted parameters from Pd K-edge EXAFS for Pd/CeO_2 and $Pd\text{-}Cu/CeO_2$.

	Coordination number	Radial distance (Å)	Debye-Waller factor
Pd/CeO_2	4.309	2.009	0.003
$Pd\text{-}Cu(1)/CeO_2$	3.736	2.002	0.003

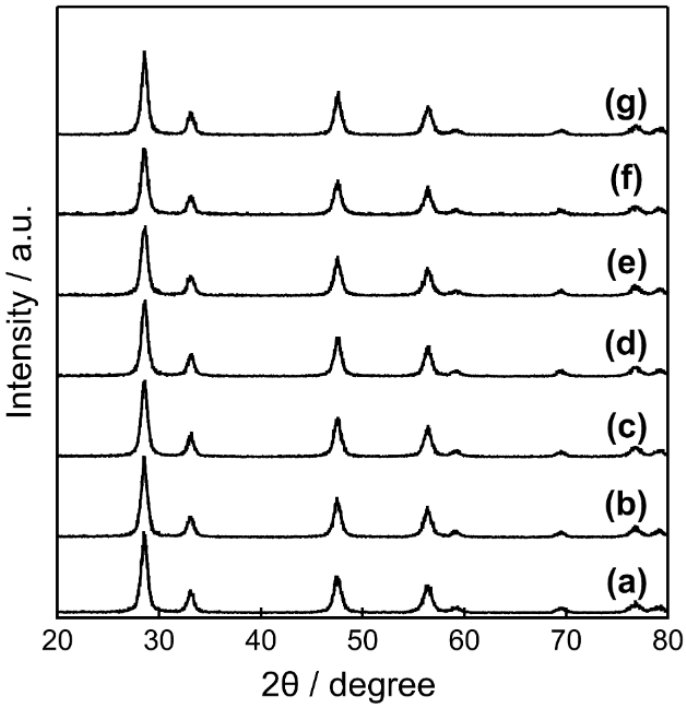

Figure 5-1. XRD patterns of Pd/CeO_2 catalysts and $Pd\text{-}Cu/CeO_2$ catalysts. (a)CeO_2; (b)Pd/CeO_2; (c)$Pd\text{-}Cu(1)/CeO_2$; (d)$Pd\text{-}Cu(2)/CeO_2$; (e)$Pd\text{-}Cu(5)/CeO_2$; (f)$Pd\text{-}Cu(10)/CeO_2$ (g)Cu/CeO_2.

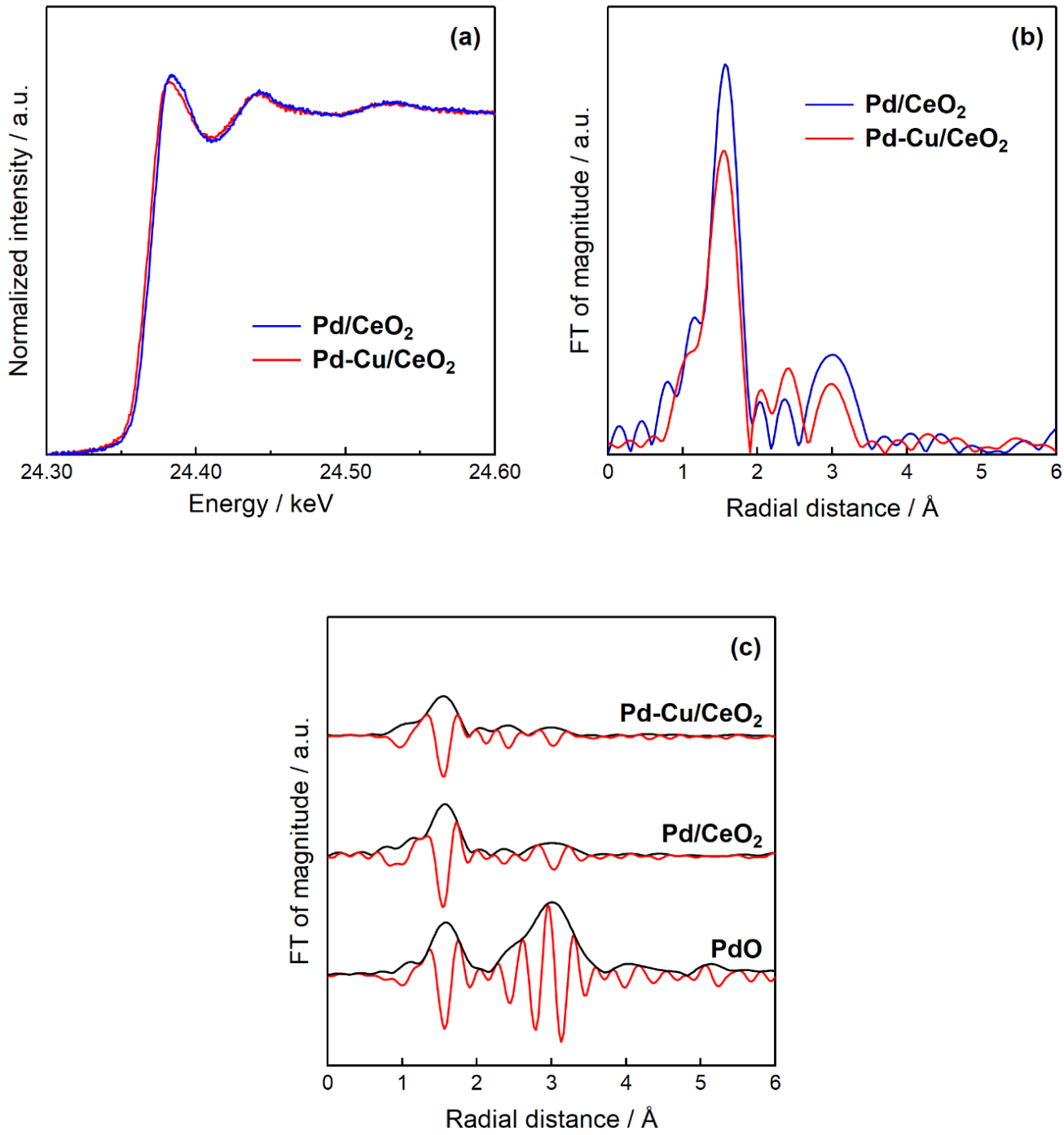

Figure 5-2. Pd K-edge (a)XANES spectra of Pd/CeO_2 and $Pd\text{-}Cu/CeO_2$; (b)EXAFS spectra of Pd/CeO_2 and $Pd\text{-}Cu/CeO_2$; (c)EXAFS spectra and imaginary parts of Pd/CeO_2 catalysts and PdO.

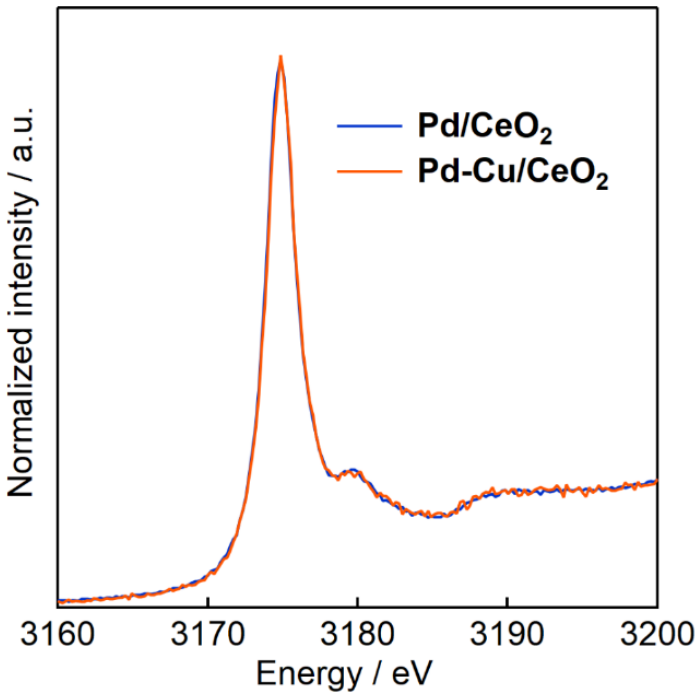

Figure 5-3. Pd L_3-edge XANES spectra of Pd/CeO_2 and $Pd\text{-}Cu/CeO_2$.

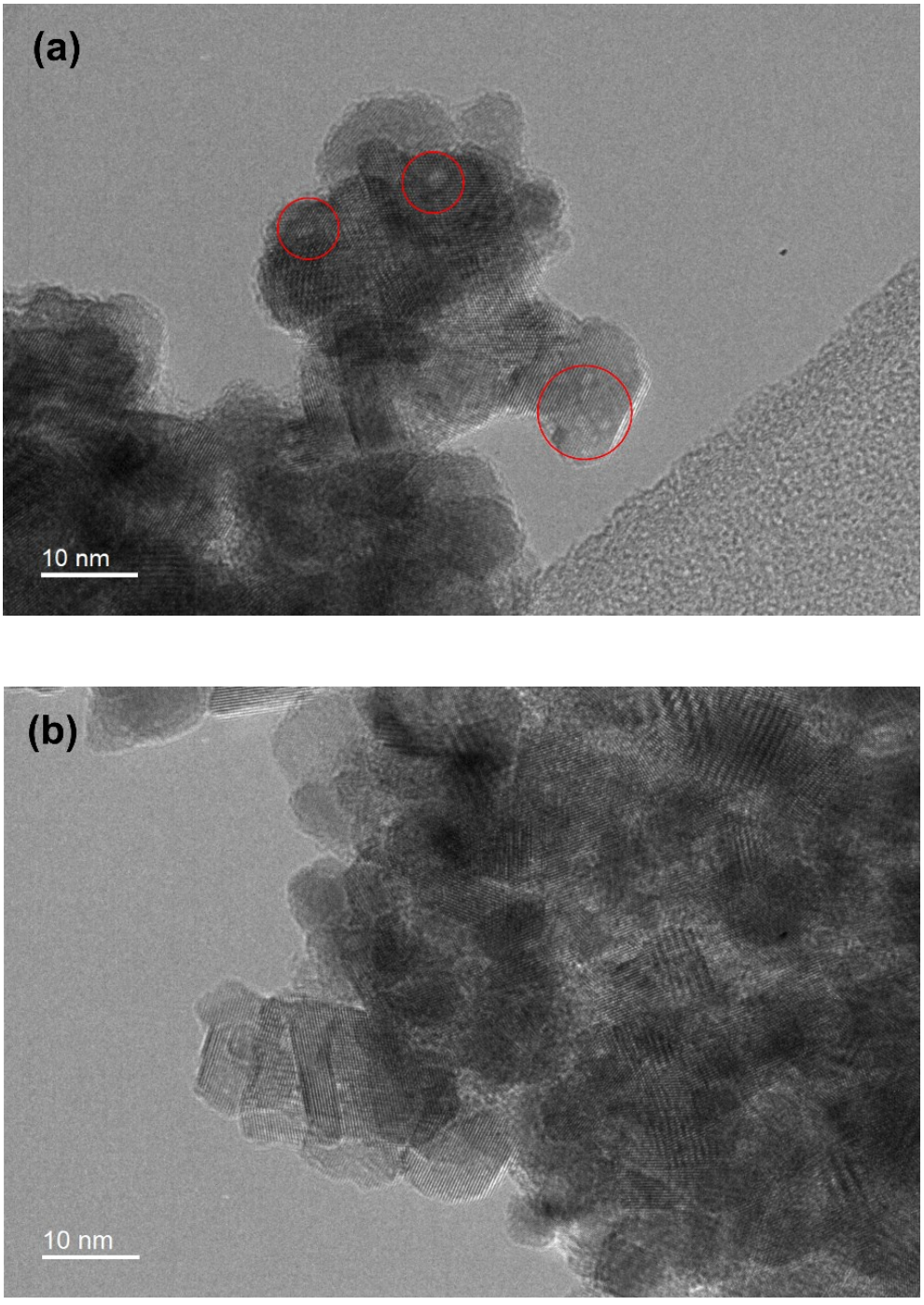

Figure 5-4. HR-TEM images of (a)Pd/CeO_2 (b)Pd-Cu(1)/CeO_2.

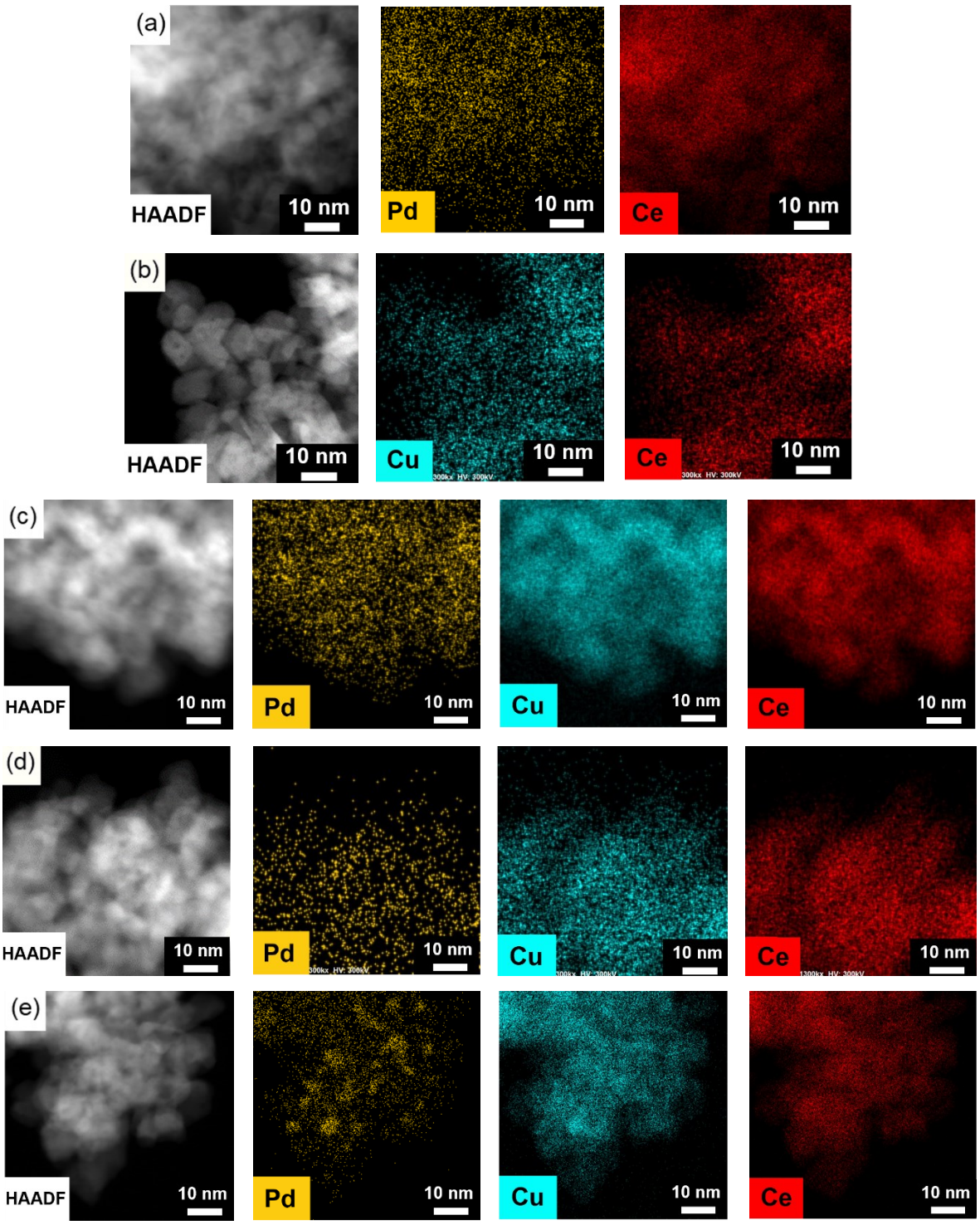

Figure 5-5. STEM-EDS images of (a)Pd/CeO_2; (b)Cu/CeO_2; (c)Pd-Cu(1)/CeO_2; (d)Pd-Cu(5)/CeO_2; (e)Pd-Cu(10)/CeO_2.

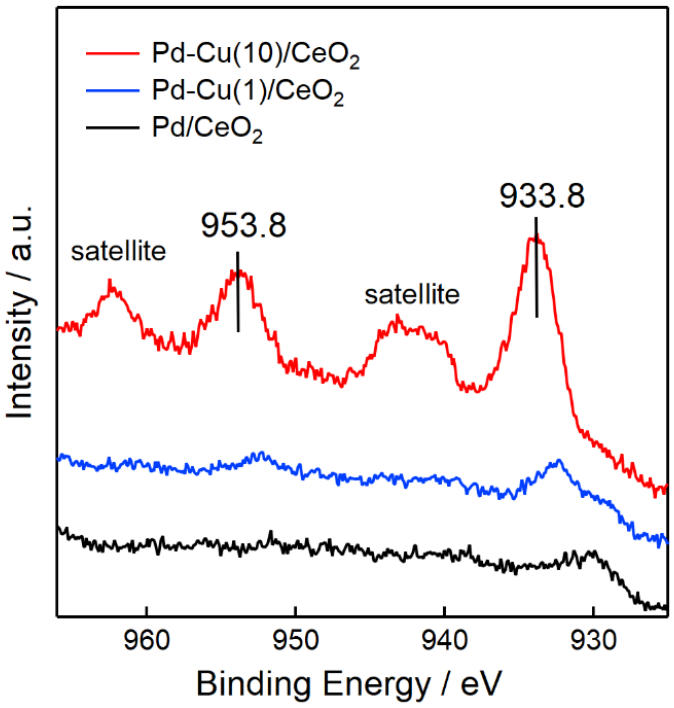

Figure 5-6. Cu 2p XPS spectra of Pd/CeO_2 and $Pd\text{-}Cu/CeO_2$.

5.3.2 Catalytic CO oxidation

The effect of the addition of Cu to Pd/CeO_2 on the CO oxidation activity under dilute O_2 conditions was investigated. CO oxidation activity of supported Pd and Pd-Cu catalysts are compared in Figure 5-7. The addition of Cu to the supported Pd catalysts improved their activities. The addition of Cu significantly enhanced especially the activity of the Pd/CeO_2 catalyst. The $Pd\text{-}Cu/CeO_2$ catalyst showed the highest activity in the 90-250 °C region. The activity of the Pd/Al_2O_3 catalyst was enhanced at higher temperatures by the addition of Cu. On the other hand, the activity of the Pd/TiO_2 catalyst showed little change due to the addition of Cu. The activity curves for Pd/CeO_2 and $Pd\text{-}Cu/CeO_2$ did not show the typical sigmoid shape, unlike in previous studies [3, 5, 6]. This is because our reaction condition is stoichiometric ($[CO]/[O_2] = 2$) rather than oxygen-rich conditions. Furthermore, the Pd/CeO_2 and $Pd\text{-}Cu/CeO_2$ catalysts have multiple active sites for CO oxidation: Pd, CeO_2, Cu, and the interface between these sites are active for CO oxidation. Therefore, one possible reason is that the activity curve deviates from a simple sigmoid curve since the CO oxidation activity differs depending on the active site. Another possible reason could be that the rate-limiting step is diffusion in the high-temperature region [28, 29].

To investigate the effect of Cu addition to Pd/CeO_2 in detail, we investigated the dependence of CO oxidation properties on Cu loading (Figure 5-8). The CO conversion increased when the Cu/Pd molar ratio was up to 5; however, the CO conversion rate decreased when the Cu/Pd molar ratio increased to 10. However, below 180 °C, all $Pd\text{-}Cu/CeO_2$ catalysts showed higher activity than Pd/CeO_2. Figure 5-8(b) shows the results of CO oxidation using Cu/CeO_2 as the catalyst for comparison. CO conversion increased monotonically with increasing Cu loading, and the highest activity was obtained with the $Cu(10)/CeO_2$ catalyst.

Reaction rates for CO oxidation over $Pd\text{-}Cu/CeO_2$ and Cu/CeO_2 catalysts with varying Cu/Pd ratios are compared in Figure 5-8(c). Here, we measured the rates under low conversion

conditions at 120 °C. The reaction rate with the Pd-Cu/CeO_2 catalyst increased with increasing Cu loading at low loadings (Cu ≤ 0.5 mmol).In this case, Pd-Cu/CeO_2 showed higher activity than Cu/CeO_2. On the other hand, the activity of the Pd-Cu(10)/CeO_2 catalyst was comparable to that of the Cu(10)/CeO_2 catalyst at high loadings. Therefore, the Cu addition to Pd/CeO_2 effectively improved the CO oxidation activity even at low Cu loadings.

To further consider the effect of the Cu loading on CO oxidation with Pd-Cu/CeO_2 catalysts, the activities of Pd-Cu/CeO_2 and the physical mixture were compared (Figure 5-9). The CO oxidation activities of the physical mixture of 2 wt% Pd/CeO_2 and 2 wt% Cu/CeO_2 were compared to those of Pd/CeO_2, Cu/CeO_2, and Pd-Cu/CeO_2. Pd-Cu/CeO_2 showed higher CO oxidation activity below 150 °C, indicating that the proximity of Pd and Cu is essential to improving the CO oxidation activities.

To investigate the effect of Cu addition on the reduction properties of the Pd catalyst, H_2-TPR was performed for CeO_2, Pd/CeO_2, Cu/CeO_2, and Pd-Cu/CeO_2 catalysts (Figure 5-10(a)). The surface CeO_2 was reduced at 250-600 °C, and the bulk CeO_2 was reduced at 700-950 °C [30, 33]. The reduction temperature of the CeO_2 surface was decreased with the addition of Pd to CeO_2. In the case of Pd/CeO_2, PdO was reduced to Pd below 50 °C (Figure 5-10(c)). The amount of H_2 consumed in this reduction process was larger than that of PdO, suggesting that the reduction of H_2 on the CeO_2 surface is proceeding simultaneously with the reduction of PdO. Therefore, Pd addition increased the reactivity of the lattice oxygen on the CeO_2 surface. This finding agrees with the results that highly dispersed nanosized PdO on CeO_2 is reduced by H_2 at temperatures below 50 °C. [23-24, 30-34]. In the Cu/CeO_2 catalyst, a peak attributed to the reduction of highly dispersed CuO on the CeO_2 appeared in the range of 80-180 °C [35-38]. The reduction temperature of the CeO_2 surface decreased by Cu addition, suggesting that the addition of Cu enhanced the reactivity of the surface lattice oxygen of CeO_2.

Figure 5-10(b) also shows the H_2-TPR profiles of Pd-Cu/CeO_2 with different Cu loadings. Profile of Pd-Cu(1)/CeO_2 shows that the reduction of PdO to Pd was observed to proceed at temperatures below 50 °C, as Pd/CeO_2. Therefore, the addition of Cu at low loadings did not affect the reducibility of PdO on CeO_2. In the case of this catalyst, no CuO reduction peak was observed in the range of 80-180 °C, showing that the reduction of CuO proceeds at lower temperatures. For the catalysts with a higher Cu/Pd ratio, the intensity of the reduction peak at 60 °C increased with increasing Cu loading. This peak is attributed to the reduction of PdO to Pd and CuO to Cu, indicating that the higher the Cu loading, the PdO reduction progresses at higher temperatures. In Figure 5-10(c), reduction peaks are observed around 20 °C for both Pd/CeO_2 and Pd-Cu(1)/CeO_2, indicating that the reduction properties of PdO are not significantly affected by Cu loading.

For Cu/Pd=10, a PdO reduction peak was observed around 60 °C, which indicates that excess Cu loading reduced the reducibility of PdO on CeO_2. As described above, Pd-Cu(10)/CeO_2 showed lower CO oxidation activity than Pd-Cu(1)/CeO_2. For Pd-Cu(10)/CeO_2 catalysts, aggregation of PdO with a particle size of 5-10 nm was observed in the STEM-EDS images (Figure 5-5(e)). These results indicate that excessive Cu loading leads to Pd agglomeration and an increase in particle size, which decreases the reducibility of PdO and, consequently, the activity of CO oxidation.

The surface density of a monolayer of CuO on CeO_2 is 3.0 atom/nm^2, assuming that CuO is theoretically a monoclinic structure. The surface area of the catalyst and the amount of Pd and Cu indicates that the amount of Cu per unit surface area of the catalyst is 5 Cu/nm^2 for Pd-Cu(5)/CeO_2, which is slightly more or similar to the amount of CuO that forms a monolayer on CeO_2. In Pd-Cu(5)/CeO_2, STEM-EDS mapping shows that Pd is highly dispersed on CeO_2. The highly dispersed Cu on the CeO_2 surface does not weaken the PdO-CeO_2 interaction that contributes to the high dispersion of PdO but rather serves to reduce the grain size of PdO. On

the other hand, in the case of Pd-Cu(10)/CeO_2, the surface concentration of CuO is estimated to be 10 atoms/nm^2, and the surface density of the above monolayer desiccated bed suggests that the CeO_2 surface is completely covered by CuO. The higher amount of CuO on CeO_2 weakens the PdO-CeO_2 interaction and promotes PdO aggregation; CuO interacts strongly with CeO_2 and is unlikely to form large particles even at high CuO loading levels, as shown by STEM-EDS mapping.

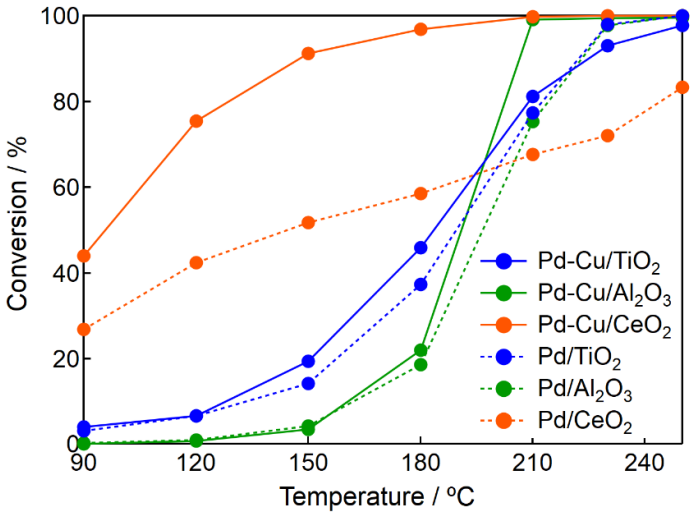

Figure 5-7. Effect of Cu on CO oxidation with Pd catalysts under dilute O_2 condition.

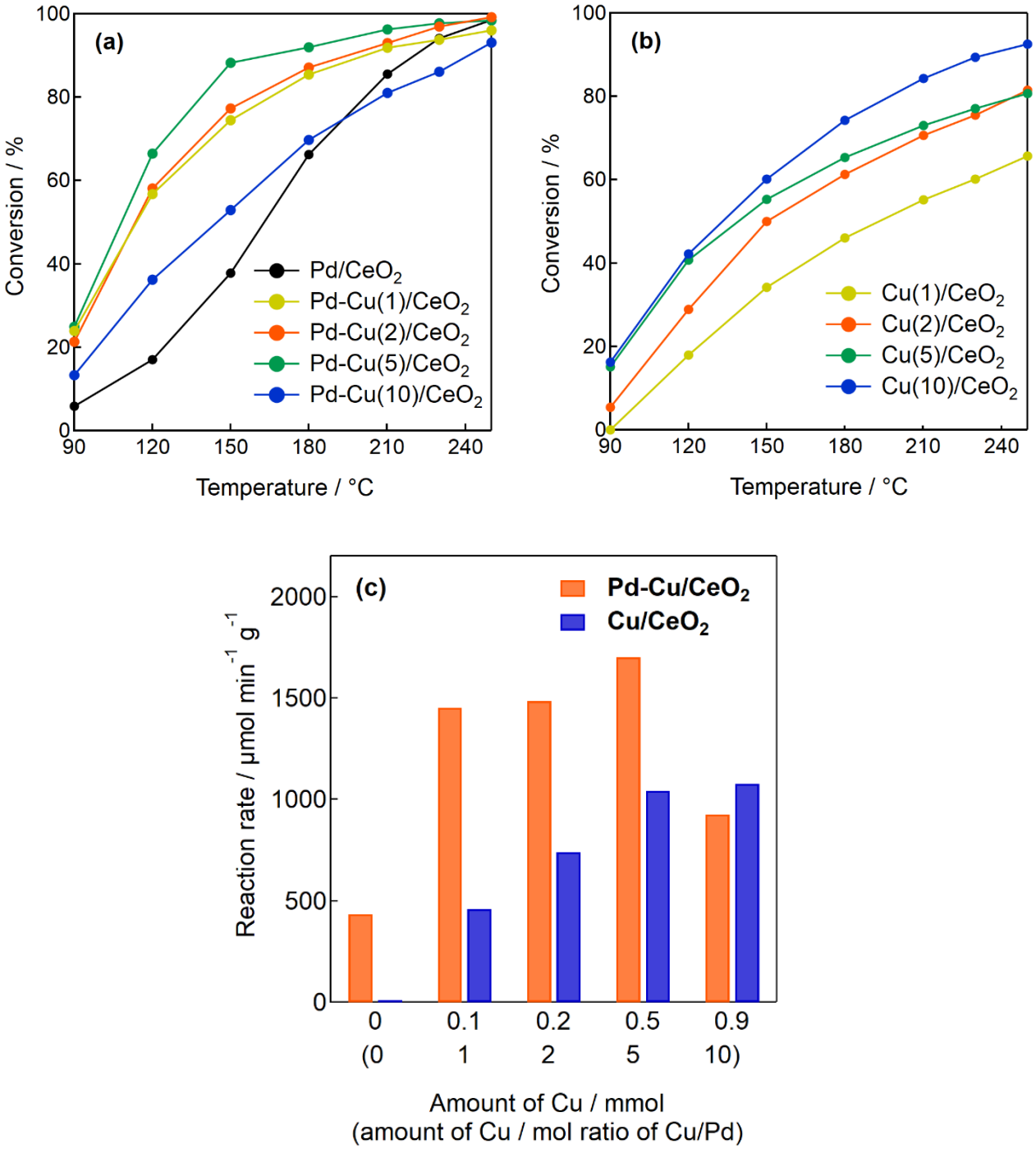

Figure 5-8. Effect of the amount of Cu loading on CO oxidation with (a)Pd-Cu/CeO_2 and (b)Cu/CeO_2 Catalyst weight 0.020 g, 0.5% CO-0.25% O_2- He(balance), gas flow rate 250 mL/min; (c)Effect of the amount of Cu loading on the reaction rate of CO oxidation at 120 °C with Pd-Cu/CeO_2 and Cu/CeO_2. Catalyst weight 0.020 g, 0.5% CO-0.25% O_2- He(balance), gas flow rate 250 mL/min.

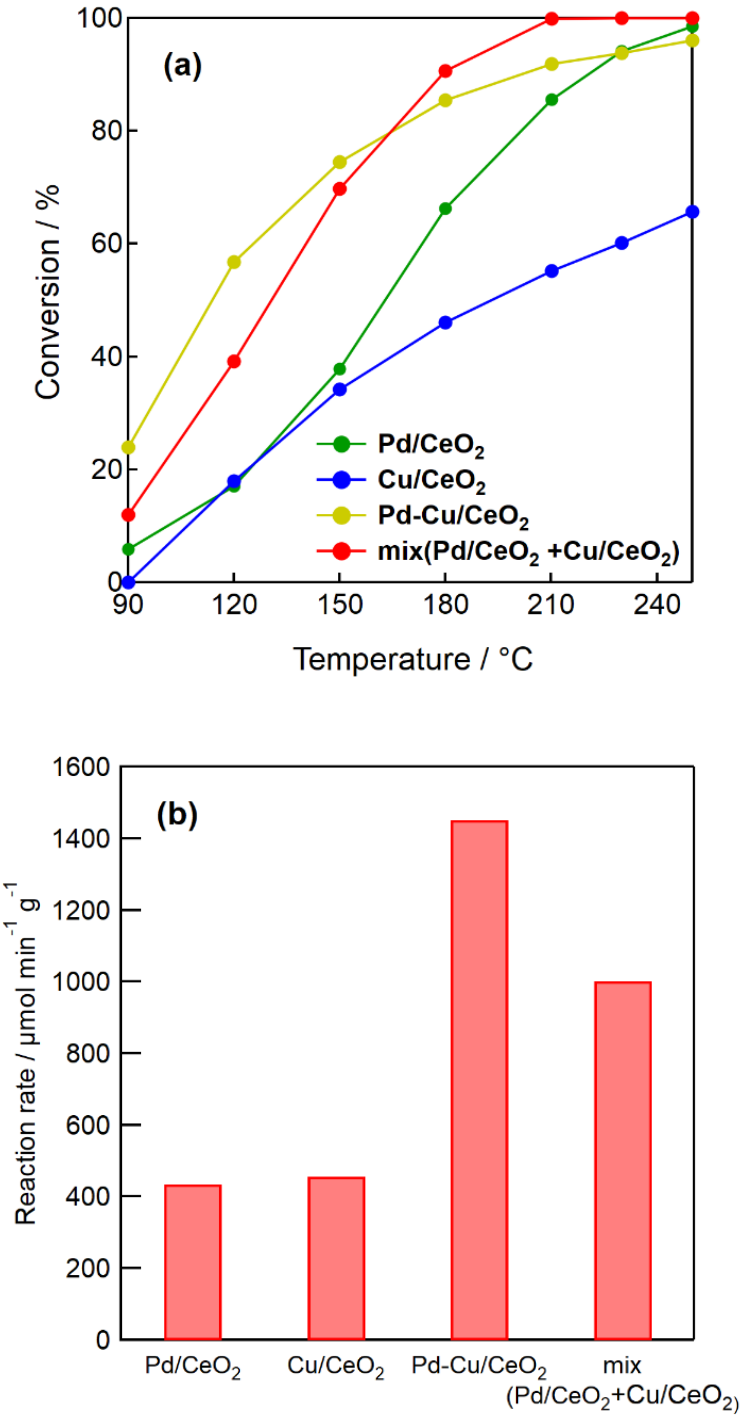

Figure 5-9. (a)Comparison of the activity of Pd-Cu/CeO_2 catalyst with physically mixed catalyst of 2 wt% Pd/CeO_2 and 2 wt% Cu/CeO_2; (b)Reaction rate at 120 °C.

Catalyst weight 0.025 g, 0.5% CO-0.25% O_2- He(balance), gas flow rate 250 mL/min.

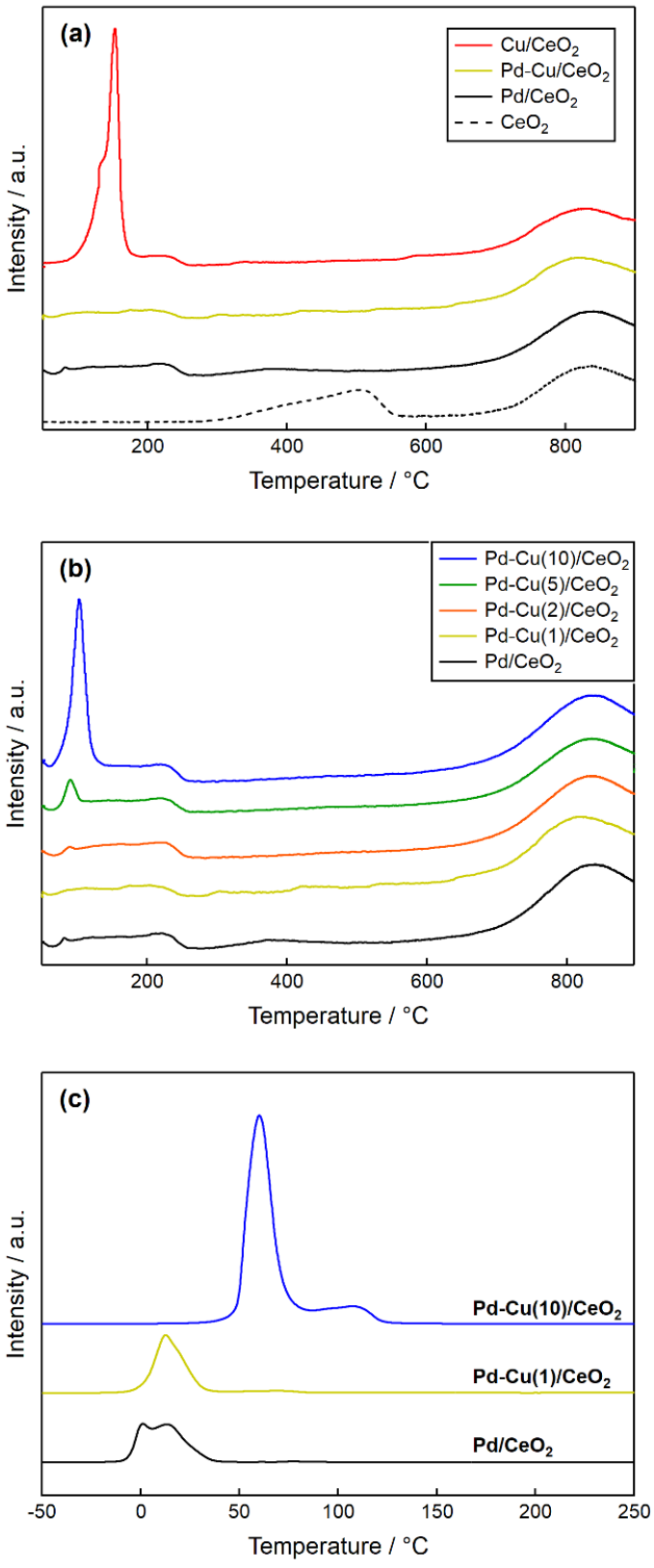

Figure 5-10. (a)H_2-TPR profiles of CeO_2 and supported CeO_2 catalysts; (b)H_2-TPR profiles of Pd/CeO_2 and $Pd\text{-}Cu/CeO_2$; (c)H_2-TPR profiles of Pd/CeO_2 and $Pd\text{-}Cu(1, 10)/CeO_2$.

5.3.3 Diffuse reflectance FTIR studies.

Figure 5-11 shows the FTIR spectra of CO species adsorbed on Pd/CeO_2, Cu/CeO_2, and $Pd-Cu(1)/CeO_2$ under $CO-N_2$ flow and $CO-O_2-N_2$ flow. The spectra of the Pd catalysts showed peaks of linearly coordinated CO on Pd at approximately 2100 cm^{-1} and peaks of bridged coordinated CO at approximately 1960 cm^{-1}. The peaks at approximately 2110 cm^{-1} are attributed to linearly coordinated CO species on Pd^{2+} or Pd^{+} [21, 39-43]. For Cu/CeO_2 catalyst, a peak of linearly coordinated CO on Cu was detected at 2104 cm^{-1}. $Pd-Cu(1)/CeO_2$ also showed a peak at 2104 cm^{-1} [44-45]. This is due to the overlap of the CO species peak on Pd and Cu. The intensity of the peak of bridge-coordinated CO on $Pd-Cu/CeO_2$ was lower than that on Pd/CeO_2. This finding indicates that the number of bridge-coordinated CO on Pd decreased due to the decrease in the sizes of the Pd particles, and this finding agrees with the EXAFS studies. The peak intensity of CO species adsorbed on the $Pd-Cu/CeO_2$ catalyst decreased significantly when the gas flow was switched to $CO-O_2-N_2$ gas, the same as Pd/CeO_2 catalyst. The peak intensity ratio at 2104 cm^{-1} calculated by normalizing the intensity under $CO-O_2-N_2$ flow to that under $CO-N_2$ flow is 0.12 for $Pd-Cu/CeO_2$, which is lower than that of Pd/CeO_2 (0.17). This result suggests that the number of Pd sites contributing to the CO oxidation reaction is higher in $Pd-Cu/CeO_2$ than in Pd/CeO_2 because of the smaller size of the Pd particles in $Pd-Cu/CeO_2$. When the gas was changed to O_2-N_2 from $CO-O_2-N_2$, the peak almost disappeared within 3 minutes, confirming the rapid oxidative desorption of adsorbed CO species on the $Pd-Cu/CeO_2$ catalyst (Figure 5-12).

Figure 5-13 shows the FTIR spectra of $Pd-Cu/CeO_2$ with different Cu/Pd ratios. $Pd-Cu(2)/CeO_2$ shows no peak shift of linearly-adsorbed CO species on Pd and Cu. In the spectra of $Pd-Cu(5)/CeO_2$ and $Pd-Cu(10)/CeO_2$, the peak of CO adsorbed species on the catalysts shifted to 2114 cm^{-1}, which is attributed to CO species adsorbed on Cu^{+} [46, 47]. The Pd particle size of the $Pd-Cu(10)/CeO_2$ catalyst was larger than that of other $Pd-Cu/CeO_2$ catalysts,

according to STEM-EDS. On the other hand, the peak of bridge-adsorbed CO species on Pd particles in Pd-Cu(10)/CeO_2 is significantly reduced compared to those in Pd-Cu(1)/CeO_2 (Figure 5-13(b)). This is in contrast to the general trend of an increase in bridge-adsorbed CO species as Pd particle size increases. Therefore, excess copper loading may have covered the Pd sites, resulting in a decrease in CO species bridged adsorbed on Pd.

The addition of a small amount of Cu to Pd/CeO_2 significantly increased the rate of CO oxidation under dilute O_2 conditions, as shown above. The added CuO acted as an active site for CO oxidation, reducing the size of PdO particles and promoting the oxidation of CO adsorbed on Pd by O_2. The loading of Pd and Cu to CeO_2 also enhanced the reduction of lattice oxygen on the CeO_2 surface, which also increased the activity of CO oxidation.

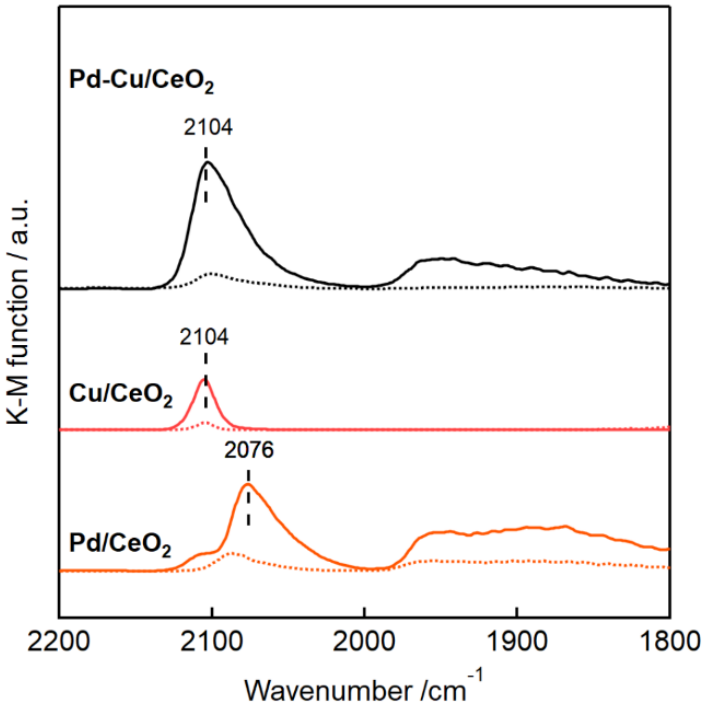

Figure 5-11. FTIR spectra of CO adsorbed on Pd catalysts and Cu/CeO_2 and $Pd\text{-}Cu/CeO_2$. solid line: 1% CO-He(balance); dotted line: 0.5% CO-0.25% O_2- He(balance).

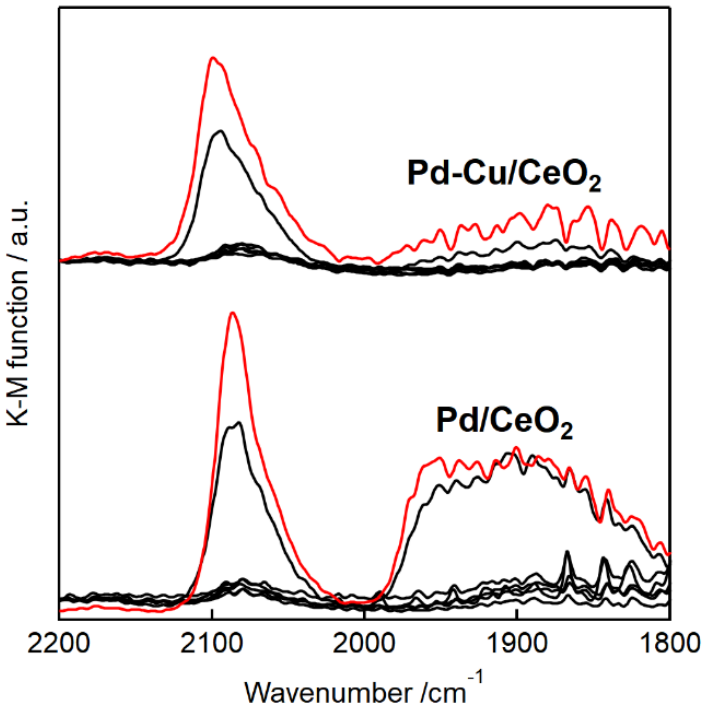

Figure 5-12. Changes of FTIR spectra of CO adsorbed on Pd/CeO_2 and $Pd\text{-}Cu/CeO_2$.
red line: under 0.5% CO-0.25% O_2- He(balance) for 30 min.
black line: under 0.25% O_2- He(balance) for 1, 3, 5, 10, 15, 20 min.

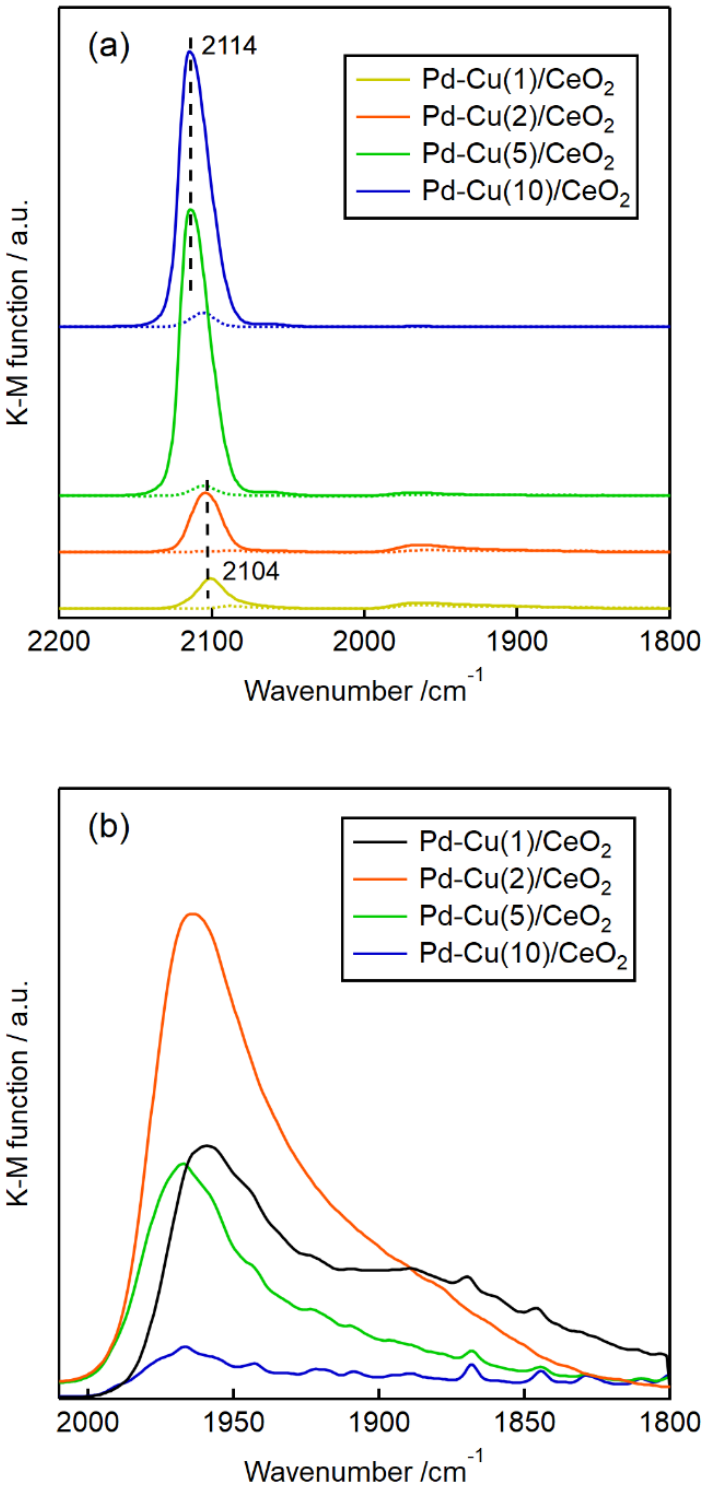

Figure 5-13. FTIR spectra of Pd-Cu/CeO_2 catalysts at (a) 1800-2200 cm^{-1} (b)1800-2000 cm^{-1}. solid line: 1% CO-He(balance); dotted line: 0.5% CO-0.25% O_2- He(balance).

5.4 Conclusion

In this chapter, I investigated the addition of Cu to Pd catalysts and its effect on their catalytic properties in CO oxidation under dilute O_2 conditions. CeO_2-supported Pd and Pd-Cu catalysts were prepared by impregnation. The catalytic CO oxidation activity of Pd/CeO_2 was higher than that of Pd/TiO_2 and Pd/Al_2O_3 at low temperatures below 180 °C. The addition of Cu to Pd/CeO_2 improved the activity, and $Pd\text{-}Cu/CeO_2$ exhibited the highest activity in all temperature ranges (90–250 °C). $Pd\text{-}Cu/CeO_2$ showed higher CO oxidation activity than Cu/CeO_2, which has been reported to exhibit high CO oxidation. The addition of Cu did not affect the electronic state of Pd and did not form Pd-Cu bimetallic particles. However, it reduced the Pd particle size and improved the dispersion of Pd. The Pd and Cu loading also improved the reactivity of surface lattice oxygen. On the other hand, the addition of excess Cu caused Pd agglomeration, which increased the particle size and reduced the reducibility of PdO, resulting in lower CO oxidation activity. FTIR studies revealed that Cu improved the oxidative desorption of CO species adsorbed on the catalysts. The addition of Cu to Pd/CeO_2 increased the number of active Pd sites for CO oxidation and improved the catalytic properties of Pd/CeO_2. Thus, the addition of Cu to Pd/CeO_2 resulted in a more efficient catalyst for CO oxidation under low-concentration oxygen conditions.

References

[1] Slavinskaya, E. M.; Gulyaev, R. V.; Zadesenets, A. V.; Stonkus, O. A.; Zaikovskii, V. I.; Shubin, Y. V.; Korenev, S. V.; Boronin, A. I. Low-Temperature CO Oxidation by Pd/CeO_2 Catalysts Synthesized Using the Coprecipitation Method. *Appl. Catal. B* **2015**, *166-167*, 91–103.

[2] Ye, J.; Xia, Y.; Cheng, D.-G.; Chen, F.; Zhan, X. Promoting Effects of Pretreatment on Pd/CeO_2 Catalysts for CO Oxidation. *Int. J. Hydrogen Energy* **2019**, *44* (33), 17985–17994.

[3] Luo, M.-F.; Hou, Z.-Y.; Yuan, X.-X.; Zheng, X.-M. Characterization Study of CeO_2 Supported Pd Catalyst for Low-Temperature Carbon Monoxide Oxidation. *Catal. Letters* **1998**, *50* (3), 205–209.

[4] Boronin, A. I.; Slavinskaya, E. M.; Danilova, I. G.; Gulyaev, R. V.; Amosov, Y. I.; Kuznetsov, P. A.; Polukhina, I. A.; Koscheev, S. V.; Zaikovskii, V. I.; Noskov, A. S. Investigation of Palladium Interaction with Cerium Oxide and Its State in Catalysts for Low-Temperature CO Oxidation. *Catal. Today* **2009**, *144* (3), 201–211.

[5] Oh, S.-H.; Hoflund, G. B. Chemical State Study of Palladium Powder and Ceria-Supported Palladium during Low-Temperature CO Oxidation. *J. Phys. Chem. A* **2006**, *110* (24), 7609–7613.

[6] Satsuma, A.; Osaki, K.; Yanagihara, M.; Ohyama, J.; Shimizu, K. Activity Controlling Factors for Low-Temperature Oxidation of CO over Supported Pd Catalysts. *Appl. Catal. B* **2013**, *132-133*, 511–518.

[7] Ward, T.; Delannoy, L.; Hahn, R.; Kendell, S.; Pursell, C. J.; Louis, C.; Chandler, B. D. Effects of Pd on Catalysis by Au: CO Adsorption, CO Oxidation, and Cyclohexene Hydrogenation by Supported Au and pd–Au Catalysts. *ACS Catal.* **2013**, *3* (11), 2644–2653.

[8] Zhang, J.; Jin, H.; Sullivan, M. B.; Lim, F. C. H.; Wu, P. Study of Pd–Au Bimetallic Catalysts for CO Oxidation Reaction by DFT Calculations. *Phys. Chem. Chem. Phys.* **2009**, *11* (9), 1441–1446.

[9] Xu, J.; White, T.; Li, P.; He, C.; Yu, J.; Yuan, W.; Han, Y.-F. Biphasic Pd-Au Alloy Catalyst for Low-Temperature CO Oxidation. *J. Am. Chem. Soc.* **2010**, *132* (30), 10398–10406.

[10] Venezia, A. M.; Liotta, L. F.; Pantaleo, G.; La Parola, V.; Deganello, G.; Beck, A.; Koppány, Z.; Frey, K.; Horváth, D.; Guczi, L. Activity of SiO_2 Supported Gold-Palladium Catalysts in CO Oxidation. *Appl. Catal. A* **2003**, *251* (2), 359–368.

[11] Rodriguez, J. A. Interactions in Bimetallic Bonding: Electronic and Chemical Properties of PdZn Surfaces. *J. Phys. Chem.* **1994**, *98* (22), 5758–5764.

[12] Jeroro, E.; Vohs, J. M. Exploring the Role of Zn in PdZn Reforming Catalysts: Adsorption and Reaction of Ethanol and Acetaldehyde on Two-Dimensional PdZn Alloys. *J. Phys. Chem. C* **2009**, *113* (4), 1486–1494.

[13] Johnson, R. S.; DeLaRiva, A.; Ashbacher, V.; Halevi, B.; Villanueva, C. J.; Smith, G. K.; Lin, S.; Datye, A. K.; Guo, H. The CO Oxidation Mechanism and Reactivity on PdZn Alloys. *Phys. Chem. Chem. Phys.* **2013**, *15* (20), 7768–7776.

[14] Jeroro, E.; Lebarbier, V.; Datye, A.; Wang, Y.; Vohs, J. M. Interaction of CO with Surface PdZn Alloys. *Surf. Sci.* **2007**, *601* (23), 5546–5554.

[15] Jeroro, E.; Vohs, J. M. Zn Modification of the Reactivity of Pd(111) toward Methanol and Formaldehyde. *J. Am. Chem. Soc.* **2008**, *130* (31), 10199–10207.

[16] He, Z.; He, Z.; Wang, D.; Bo, Q.; Fan, T.; Jiang, Y. Mo-Modified Pd/Al_2O_3 Catalysts for Benzene Catalytic Combustion. *J. Environ. Sci.* **2014**, *26* (7), 1481–1487.

[17] Konopny, L. W.; Juan, A.; Damiani, D. E. Preparation and Characterization of γ-Al_2O_3-Supported PdMo Catalysts. *Appl. Catal. B* **1998**, *15* (1), 115–127.

[18] de Mello, L. F.; Noronha, F. B.; Schmal, M. NO Reduction with Ethanol on Pd–Mo/Al2O3 Catalysts. *J. Catal.* **2003**, *220* (2), 358–371.

[19] Choi, E. J.; Lee, Y. H.; Lee, D.-W.; Moon, D.-J.; Lee, K.-Y. Hydrogenation of CO_2 to Methanol over Pd–Cu/CeO_2 Catalysts. *Molecular Catalysis* **2017**, *434*, 146–153.

[20] Wang, F.; Zhao, K.; Zhang, H.; Dong, Y.; Wang, T.; He, D. Low Temperature CO Catalytic Oxidation over Supported Pd–Cu Catalysts Calcined at Different Temperatures. *Chem. Eng. J.* **2014**, *242*, 10–18.

[21] Shen, Y.; Lu, G.; Guo, Y.; Wang, Y.; Guo, Y.; Gong, X. Study on the Catalytic Reaction Mechanism of Low Temperature Oxidation of CO over Pd–Cu–Clx/Al_2O_3 Catalyst. *Catal. Today* **2011**, *175* (1), 558–567.

[22] Wang, F.; Lu, G. Hydrogen Feed Gas Purification over Bimetallic Cu--Pd Catalysts--Effects of Copper Precursors on CO Oxidation. *Int. J. Hydrogen Energy* **2010**, *35* (13), 7253–7260.

[23] Fox, E. B.; Lee, A. F.; Wilson, K.; Song, C. In-Situ XPS Study on the Reducibility of Pd-Promoted Cu/CeO_2 Catalysts for the Oxygen-Assisted Water-Gas-Shift Reaction. *Top. Catal.* **2008**, *49* (1), 89–96.

[24] Fox, E. B.; Velu, S.; Engelhard, M. H.; Chin, Y.-H.; Miller, J. T.; Kropf, J.; Song, C. Characterization of CeO_2-Supported Cu–Pd Bimetallic Catalyst for the Oxygen-Assisted Water–gas Shift Reaction. *J. Catal.* **2008**, *260* (2), 358–370.

[25] Kugai, J.; Miller, J. T.; Guo, N.; Song, C. Oxygen-Enhanced Water Gas Shift on Ceria-Supported Pd–Cu and Pt–Cu Bimetallic Catalysts. *J. Catal.* **2011**, *277* (1), 46–53.

[26] Kugai, J.; Fox, E. B.; Song, C. Role of CeO_2 Support for Pd-Cu Bimetallic Catalysts for Oxygen-Enhanced Water Gas Shift. *Appl. Catal. A* **2013**, *456*, 204–214.

[27] Smidt, J.; Hafner, W.; Jira, R.; Sieber, R.; Sedlmeier, J.; Sabel, A. The Oxidation of Olefins with Palladium Chloride Catalysts. *Angew. Chem. Int. Ed Engl.* **1962**, *1* (2), 80–88.Duprat, F. Light-off Curve of Catalytic Reaction and Kinetics. *Chem. Eng. Sci.* **2002**, *57* (6), 901–911.

[28] van Spronsen, M. A.; Frenken, J. W. M.; Groot, I. M. N. Surface Science under Reaction Conditions: CO Oxidation on Pt and Pd Model Catalysts. *Chem. Soc. Rev.* **2017**, *46* (14), 4347–4374.

[29] Costa, L. O. O.; Silva, A. M.; Borges, L. E. P.; Mattos, L. V.; Noronha, F. B. Partial Oxidation of Ethanol over Pd/CeO_2 and Pd/Y_2O_3 Catalysts. *Catal. Today* **2008**, *138* (3), 147–151.

[30] Leitenburg, C. de; Trovarelli, A.; Kašpar, J. A Temperature-Programmed and Transient Kinetic Study of CO_2 Activation and Methanation over CeO_2Supported Noble Metals. *J. Catal.* **1997**, *166* (1), 98–107.

[31] Lin, W.; Lin, L.; Zhu, Y. X.; Xie, Y. C.; Scheurell, K.; Kemnitz, E. Novel Pd/TiO_2–ZrO_2 Catalysts for Methane Total Oxidation at Low Temperature and Their 18O-Isotope Exchange Behavior. *J. Mol. Catal. A Chem.* **2005**, *226* (2), 263–268.

[32] Ryou, Y.; Lee, J.; Lee, H.; Kim, C. H.; Kim, D. H. Low Temperature NO Adsorption over Hydrothermally Aged Pd/CeO_2 for Cold Start Application. *Catal. Today* **2018**, *307*, 93–101.

[33] Hoffmann, M.; Kreft, S.; Georgi, G.; Fulda, G.; Pohl, M.-M.; Seeburg, D.; Berger-Karin, C.; Kondratenko, E. V.; Wohlrab, S. Improved Catalytic Methane Combustion of Pd/CeO_2 Catalysts via Porous Glass Integration. *Appl. Catal. B* **2015**, *179*, 313–320.

[34] Si, R.; Raitano, J.; Yi, N.; Zhang, L.; Chan, S.-W.; Flytzani-Stephanopoulos, M. Structure Sensitivity of the Low-Temperature Water-Gas Shift Reaction on Cu–CeO_2 Catalysts. *Catal. Today* **2012**, *180* (1), 68–80.

[35] Wang, W.-W.; Du, P.-P.; Zou, S.-H.; He, H.-Y.; Wang, R.-X.; Jin, Z.; Shi, S.; Huang, Y.-Y.; Si, R.; Song, Q.-S.; Jia, C.-J.; Yan, C.-H. Highly Dispersed Copper Oxide Clusters as Active Species in Copper-Ceria Catalyst for Preferential Oxidation of Carbon Monoxide. *ACS Catal.* **2015**, *5* (4), 2088–2099.

[36] Wang, F.; Tian, J.; Li, M.; Li, W.; Chen, L.; Liu, X.; Li, J.; Muhetaer, A.; Li, Q.; Wang, Y.; Gu, L.; Ma, D.; Xu, D. A Photoactivated cu–CeO_2 Catalyst with cu-[O]-Ce Active Species Designed through MOF Crystal Engineering. *Angew. Chem. Weinheim Bergstr. Ger.* **2020**, *132* (21), 8280–8286.

[37] Avgouropoulos, G.; Ioannides, T. Selective CO Oxidation over CuO-CeO_2 Catalysts Prepared via the Urea–nitrate Combustion Method. *Appl. Catal. A* **2003**, *244* (1), 155–167.

[38] Ortega, A.; Huffman, F. M.; Bradshaw, A. M. The Adsorption of CO on Pd (100) Studied by IR Reflection Absorption Spectroscopy. *Surf. Sci.* **1982**.

[39] Zeinalipour-Yazdi, C. D.; Willock, D. J.; Thomas, L.; Wilson, K.; Lee, A. F. CO Adsorption over Pd Nanoparticles: A General Framework for IR Simulations on Nanoparticles. *Surf. Sci.* **2016**, *646*, 210–220.

[40] Ryczkowski, J. IR Spectroscopy in Catalysis. *Catal. Today* **2001**, *68*, 263–381.

[41] Mondelli, C.; Ferri, D.; Grunwaldt, J.-D.; Krumeich, F.; Mangold, S.; Psaro, R.; Baiker, A. Combined Liquid-Phase ATR-IR and XAS Study of the Bi-Promotion in the Aerobic Oxidation of Benzyl Alcohol over Pd/Al_2O_3. *J. Catal.* **2007**, *252* (1), 77–87.

[42] Busca, G.; Finocchio, E.; Escribano, V. S. Infrared Studies of CO Oxidation by Oxygen and by Water over Pt/Al_2O_3 and Pd/Al_2O_3 Catalysts. *Appl. Catal. B* **2012**, *113-114*, 172–179.

[43] Martínez-Arias, A.; Fernández-García, M.; Soria, J.; Conesa, J. C. Spectroscopic Study of a Cu/CeO_2 Catalyst Subjected to Redox Treatments in Carbon Monoxide and Oxygen. *J. Catal.* **1999**, *182* (2), 367–377.

[44] Hollins, P. The Influence of Surface Defects on the Infrared Spectra of Adsorbed Species. *Surf. Sci. Rep.* **1992**, *16* (2), 51–94.

[45] Luo, J.-Y.; Meng, M.; Zha, Y.-Q.; Guo, L.-H. Identification of the Active Sites for CO and C3H8 Total Oxidation over Nanostructured CuO−CeO_2 and Co_3O_4−CeO_2 Catalysts. *J. Phys. Chem. C* **2008**, *112* (23), 8694–8701.

[46] Liu, L.; Yao, Z.; Deng, Y.; Gao, F.; Liu, B.; Dong, L. Morphology and Crystal-Plane Effects of Nanoscale Ceria on the Activity of CuO/CeO_2 for NO Reduction by CO. *ChemCatChem* **2011**, *3* (6), 978–989.

Chapter 6

The effects of SO_2 on the catalytic VOC oxidation of Pd/γ-Al_2O_3

6.1 Introduction

Volatile organic compounds (VOCs) are harmful to the human body and cause air pollution by reacting with nitrogen oxides in the atmosphere to produce photochemical oxidants. In recent years, VOC emission regulations have been strengthened worldwide. Then reducing the amount of VOCs emitted from factories is needed. There are various methods for removing VOCs, such as adsorption, absorption, thermal combustion, and catalytic oxidation [1, 2]. In the catalytic oxidation of VOCs, supported precious metals are commonly used because they can remove VOCs at low temperatures.

Supported Pd catalysts show high activity for oxidation reactions. γ-Al_2O_3 has a large surface area and can be used as a support to load Pd with highly dispersed. Therefore, many studies have been conducted on the catalytic oxidation of VOCs using Pd/γ-Al_2O_3 catalysts [2-9]. Various factors, such as the preparation method, active site structure, and precious metal-support interaction, determine the catalytic activity in catalytic reactions using supported metal catalysts. Haneda et al. reported that Pd/γ-Al_2O_3 with larger PdO particle size shows higher VOC oxidation activity. On the other hand, catalytic activity decreases when the particle size becomes too large. An example of this is sintering during use at high temperatures. It is known that when sintering occurs, the activity decreases because the particle size of the active metal increases and the specific surface area of the active component decreases [10-12].

VOCs and SO_2 coexist in the exhaust gases, and the catalytic combustion method is used for gas treatment. Poisoning by sulfur coexisting in the flue gas causes a significant decrease in

the catalytic activity of precious metal catalysts [10-16]. The decrease in catalytic activity due to sulfur poisoning is reported to be caused by the adsorption of sulfur on the active metal and support, resulting in the formation of inactive metal sulfides [10, 13-16]. Even when the active species, Pd, is not poisoned, sulfur treatment significantly alters surface properties such as acidity. Numerous studies have attempted to regenerate sulfur-poisoned catalysts by heat treatment or reductive treatment. To our knowledge, however, there have been no reports of sulfur species contributing to the improvement of catalytic properties of Pd/γ-Al_2O_3 in VOC oxidation reactions.

In this chapter, the effect of SO_2 treatment on benzene oxidation using Pd/γ-Al_2O_3 was investigated. The catalytic benzene oxidation activity of Pd/γ-Al_2O_3 catalysts was reduced by high-temperature treatment, and then the activity was improved by SO_2 treatment. I examined in detail the effects of heat treatment and SO_2 treatment on the catalyst structure Pd particle size and oxidation state and benzene adsorption and desorption properties of the catalysts.

6.2 Experimental

6.2.1 Catalyst preparation

Pd/γ-Al_2O_3 was prepared by impregnation methods. Catalyst support was γ-Al_2O_3 (JRC-ALO-8, the Catalysis Society of Japan), and Pd precursor was $Pd(NH_3)_4(NO_3)_2$ (Sigma-Aldrich Co., Ltd.). Pd solution was dropped into the support powder. The catalysts were dried at 100 °C and calcined at 400 °C for 2 h in the air. The H_2 reduction was carried out at 200 °C for 1 h in 5% H_2-N_2 flow. The Pd loading was set to 1 wt %.

6.2.2 Catalyst characterization

X-ray diffraction (XRD) measurement was carried out using a RIGAKU Ultima IV X-Ray diffractometer with Cu-Kα radiation at 40 kV and 20 mA. N_2 adsorption isotherms were measured using a BELSORP-mini II instrument (Microtrac BEL, Japan) at 77 K. Scanning transmission electron microscopy (STEM) observation and energy dispersive spectroscopy (EDS) elemental mapping was carried out using Titan G2 cubed (Gatan).

X-ray absorption near edge structure (XANES) and extended X-ray absorption fine structure (EXAFS) spectra were measured at Kyushu Synchrotron Light Research Center (SAGA-LS). EXAFS spectra of Pd K-edge were measured with transmission mode at BL07. Fourier transform-EXAFS spectra were measured from k^3-weighted EXAFS data at 3.0-13.0 Å. Pd L_3-edge XANES spectra were measured with fluorescence mode at the Kyushu University beamline (KU-BL06).

The S/Pd molar ratio was obtained from the X-ray fluorescence spectra obtained during the measurement. The monochromator was set to a photon energy of 3.5 keV, and both S and Pd

fluorescence spectra were measured. The S/Pd molar ratio of the SO_2-treated catalyst was calculated from the area of S and Pd in the fluorescence spectra.

In situ diffuse reflection FTIR (DRIFTS) measurements were obtained using an FTIR-4100 spectrometer (Jasco Corporation, Japan) equipped with a diffuse reflection accessory with a BaF_2 window. in SO_2 adsorption, spectra were obtained at 600 °C under SO_2 flow with a resolution of 4 cm^{-1}. In adsorbed benzene oxidation, measurements were carried out at 275 °C. After 30 min under 400 ppm benzene-N_2, the spectra were switched to 400 ppm benzene-20% O_2- N_2 gas.

Benzene adsorption and temperature-programmed oxidation (TPO) were performed in a fixed-bed flow system equipped with an FTIR spectrometer (Perkin Elmer Spectrum 3) with a gas cell (optical path length 2.4 m). First, 500 ppm C_6H_6 -N_2 gas was introduced into the bypass line. Next, this gas was switched to the reactor at 50 °C. The outflowing gas from the reactor was analyzed by FTIR spectrometer. The catalyst was then heated to 500 °C at a 5 °C/min rate under 20% O_2- N_2 flow.

6.2.3 Catalytic benzene oxidation

Catalytic benzene oxidation was measured with a fixed bed flow reactor. Pd/γ-Al_2O_3 catalysts were pretreated under various conditions. The catalysts were heated in 20% O_2-N_2 at 800 °C for 3 h for high-temperature treatment. Then, SO_2 treatment was carried out with 500 ppm SO_2-20% O_2-N_2 at 600 °C for 1 h. After the treatment, the SO_2-containing gas was changed to O_2-N_2 flow at 600 °C, and the temperature was gradually decreased to room temperature. Before benzene oxidation, fresh catalyst samples or the pretreated catalysts were heated at 350 °C for 1 h in an O_2/N_2 or N_2 flow. Reaction gas (400 ppm C_6H_6-20% O_2-N_2 balance, 100 mL/min) was introduced into the reactor, and benzene concentration was obtained by GC-FID

(GC 390B, GL SCIENCE). CO_2 concentration was measured by the FTIR spectrometer equipped with a gas cell. The steady-state activity at each temperature was measured via two reaction histories: the catalyst temperature was raised stepwise from 150 °C to 350 °C (heating process), and the temperature was lowered stepwise from 350 °C to 150 °C (cooling process). After the reaction reached a steady state, the conversion was measured.

6.3 Results and discussion

6.3.1 Catalytic benzene activity of Pd/γ-Al_2O_3 before and after treatment

The benzene oxidation activity of Pd/γ-Al_2O_3 catalysts in the range of 150-350 °C was shown in Figure 6-1. Pretreatment conditions and reaction history strongly affect the activity of Pd/γ-Al_2O_3. Figure 6-1(a) shows the activity in the case that the pretreatment was performed under N_2 conditions, and the reaction temperature was raised stepwise to measure the steady-state activity at each temperature. The fresh catalyst showed benzene oxidation activity from 150 °C. Benzene conversion increased monotonously with the reaction temperature. After heating at 800 °C, the light-off temperature increased to 250 °C, and the benzene conversion decreased at all temperatures. The decrease in oxidation activity of the supported Pd catalyst is caused by the sintering and agglomeration of Pd particles supported on γ-Al_2O_3 by high-temperature treatment, as previously reported [11, 17-19]. When the catalyst heat-treated at 800 °C was treated with SO_2 at 600 °C, the catalyst activity increased. Figure 6-2 shows that SO_2-treated Pd/γ-Al_2O_3 catalysts showed high stability for the benzene oxidation reaction. The benzene conversion did not decrease after 480 min at 275 °C. Catalysts heated at 800 °C were also heated at 600 °C in the absence of SO_2 to investigate the effect of SO_2 treatment for comparison. The catalyst exhibited lower activity than the SO_2-treated catalyst. Figure 6-1(b) shows the catalytic activity during the cooling process. As the reaction temperature was lowered stepwise from 350 °C, the activities were changed, and the SO_2-treated catalyst exhibited slightly higher activity than other catalysts. Table 6-1 shows the surface area of each catalyst. The surface area decreased after heating at 800 °C but remained unchanged by the subsequent SO_2 treatment.

Figure 6-1(c) shows the activity when the pretreatment was performed under O_2-N_2 conditions, and the catalyst temperature was increased stepwise. In this case, the light-off

temperature of the fresh catalyst was raised to 250 °C. This result indicates that the oxidized Pd does not contribute to benzene oxidation reaction at temperatures lower than 250 °C, and the reduced Pd is the active site. The decrease in catalytic activity caused by heating at high temperatures was smaller than that caused by pretreatment under N_2 conditions. SO_2 treatment of the catalyst at 600 °C then increased the benzene conversion; in contrast, the activity was decreased after the heat treatment at 600 °C in the absence of SO_2. Figure 6-1(d) shows the activity when the reaction temperature was lowered stepwise. The SO_2-treated catalyst exhibited higher benzene oxidation activity than the other catalysts.

In the case of oxidation reactions using supported noble metal catalysts, catalytic activity differs between the heating and cooling processes, and hysteresis loops are often observed in the activity curve. Generally, the change in the structure and oxidation state of the noble metal due to the thermal history affects the catalytic activity. The result of this study shows that the benzene oxidation activity of both treated catalysts increased when exposed to benzene-containing air at 350 ºC, suggesting that the Pd was reduced and activated. Regardless of the catalyst pretreatment process or reaction histories, SO_2 treatment improves the benzene oxidation activity of the Pd/γ-Al_2O_3 catalysts heated at 800 °C.

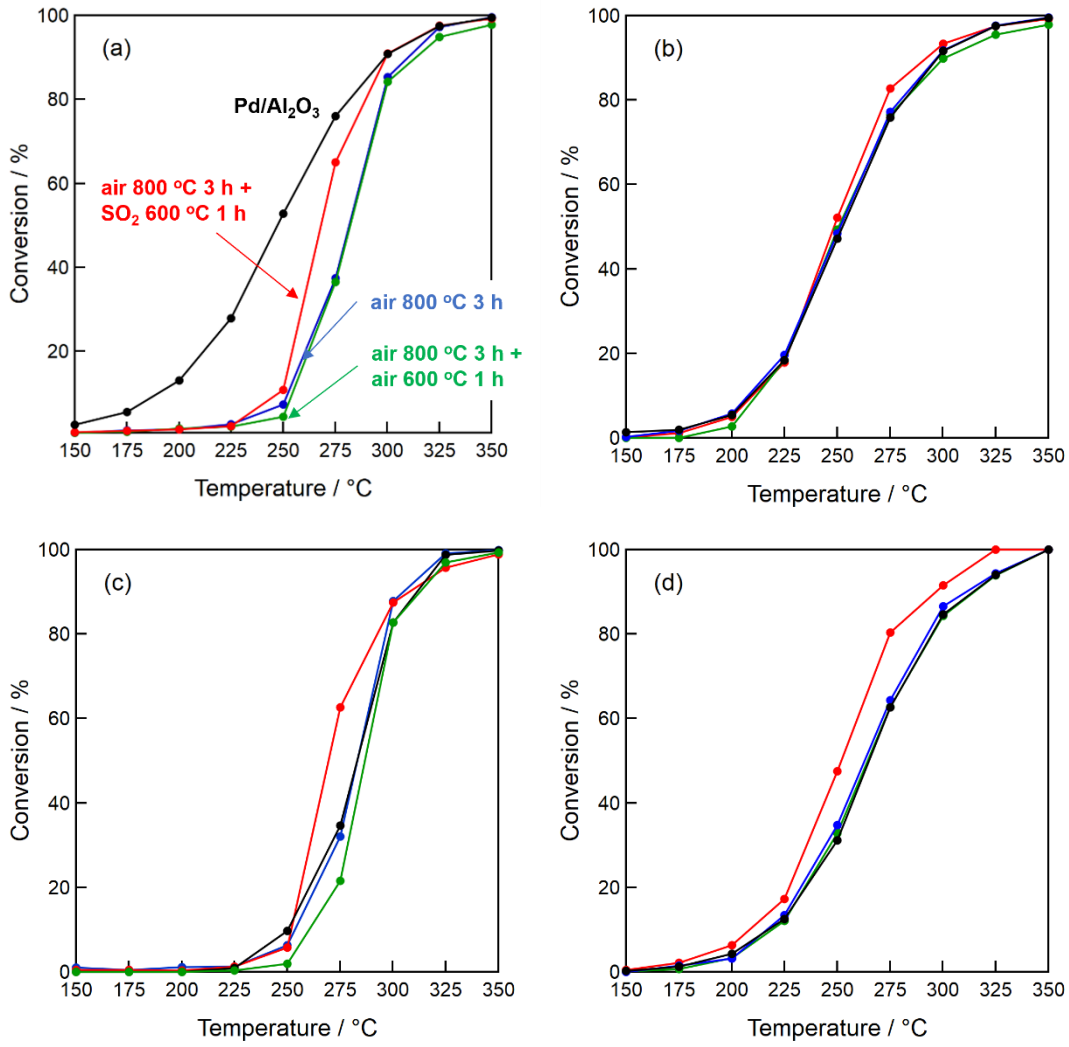

Figure 6-1. Benzene oxidation activities of Pd/γ-Al_2O_3 catalysts in the range of 150-350 °C when the pretreatment was performed under N_2 conditions (a)heating process (b)cooling process; when the pretreatment was performed under O_2-N_2 conditions (c)heating process (d)cooling process.

(—) fresh Pd/γ-Al_2O_3 catalyst; (—) the catalyst heated at 800 ˚C; (—) the catalyst heated at 800 ˚C and SO_2 treated at 600 ˚C; (—) the catalyst heated at 800 ˚C, and then 600 ˚C in the absence of SO_2.

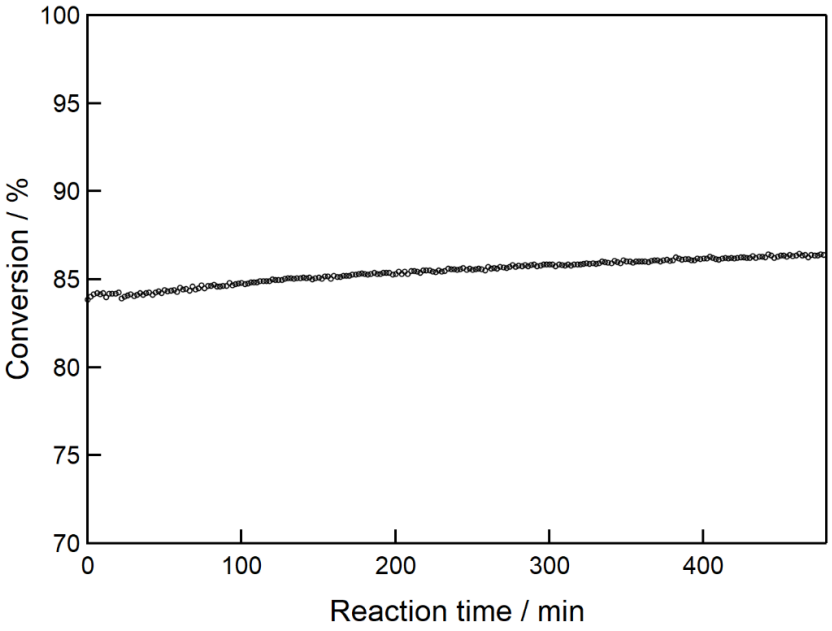

Figure 6-2. Benzene oxidation activities of SO_2-treated Pd/γ-Al_2O_3 catalysts at 275 °C.

Table 6-1. Surface area of Pd/γ-Al_2O_3 and the amount of adsorbed benzene after various treatment.

Treatment	Surface area / m^2 g^{-1}
—	185.1
Heat treatment[a]	164.3
SO_2 treatment[b]	161.6

[a]Catalyst was heated at 800 ˚C in air.

[b]Catalyst was heated at 800 ˚C in air and SO_2 treated at 600 ˚C.

6.3.2 Structural change of Pd/γ-Al_2O_3 after treatment

High-temperature treatment of Pd/γ-Al_2O_3 caused the sintering and coarsening of Pd particles. XRD patterns of γ-Al_2O_3 and Pd/γ-Al_2O_3 before and after the heat treatments are shown in Figure 6-3. In the diffraction pattern of fresh γ-Al_2O_3, peaks attributed to $Al(OH)_3$ were detected at 20° and 41°. On the other hand, in the Pd/γ-Al_2O_3 after calcination at 400 °C, these peaks disappeared due to the transformation of $Al(OH)_3$ to γ-Al_2O_3. The peaks of Pd or PdO were not detected in the diffraction pattern of fresh Pd/γ-Al_2O_3, indicating that Pd was highly dispersed on γ-Al_2O_3. After heat treatment at 800 °C, a peak attributed to Pd^0 was detected around 40°. Therefore, the heat treatment increased the Pd particle size. For the sample treated with SO_2 at 600 °C, the peak of Pd^0 disappeared, and the peaks of PdO were detected at 30° and 54°, revealing that Pd^0 was oxidized to PdO by the SO_2 treatment.

XAFS studies were performed to investigate the change in the local structure of Pd sites in Pd/γ-Al_2O_3 before and after the post-treatment. Pd K-edge XANES spectra of Pd/γ-Al_2O_3 after heating and SO_2 treatments are shown in Figure 6-4(a). In the XANES spectrum of Pd/γ-Al_2O_3, the peak was detected at 24.38 keV attributed to the transition from the 1s orbital to the 5p orbital. After heating at 800 °C, the peak intensity decreased, and the peak shifted to the lower energy side. This change reveals that the average oxidation state of Pd decreased because of the heat treatment. After SO_2 treatment at 600 °C, the peak intensity increased, showing that Pd on γ-Al_2O_3 was re-oxidized.

Pd K-edge EXAFS spectra of Pd/γ-Al_2O_3 after heat treatment and sulfurization are shown in Figure 6-4(b). The spectrum of fresh Pd/γ-Al_2O_3 showed a peak at 1.6Å, which was attributed to the Pd-O bond. The no peak of Pd-O-Pd bonds at the second coordination sphere indicates the presence of small PdO particles on the support. After heating the catalyst at 800 °C in air,

the EXAFS spectrum showed a strong peak around 2.5 Å, which was attributed to the Pd-Pd bond. The peak of Pd-O bonds (1.6 Å) also remained after the heat treatment. These results demonstrated that the smaller PdO particles on the γ-Al_2O_3 were changed into bigger Pd^0 particles, whereas some particles maintained the small PdO particles. Pd^0 was oxidized when the catalyst was treated with SO_2 at 600 °C, as evident by the decrease in the peak intensity of the Pd-Pd bond and the detection of peaks at 1.56 and 3.0, which are attributable to the Pd-O bond and Pd-(O)-Pd bond, respectively. The presence of the Pd-(O)-Pd bond suggests that the SO_2-treated catalyst's PdO particle sizes were significantly larger than those of the fresh catalyst. The thermodynamic stability of PdO and Pd can explain these findings. PdO has a melting point of 750 °C and decomposes into Pd and O_2 above this temperature in the air. Pd^0 is, however, easily oxidized at temperatures lower than 727 °C. Therefore, heat treatment at 800 °C reduces PdO and agglomerates the particles to form large Pd^0 particles. The particles are subsequently oxidized to PdO particles by contact with O_2 at temperatures lower than 727 °C.

In Figure 6-5, The oxidation state of Pd species was also pursued by the Pd L_3-edge XANES studies. The Pd L_3-edge XANES spectra of Pd/γ-Al_2O_3 before or after each treatment show a white line peak at 3174.4 eV, which is attributed to the transition from the 2p orbital to the 4d orbital. The oxidation state of Pd and the cluster sizes of Pd are reflected in the peak intensity of the Pd L_3-edge XANES spectrum [20, 21]. By heating at 800 °C, the white line peak intensity of Pd/γ-Al_2O_3 was decreased. The decreased oxidation state of Pd is consistent with the results of the K-edge XANES and EXAFS studies of Pd. The peak intensity increased after the SO_2 treatment at 600 °C, indicating that the Pd sites were oxidized. After these treatments, no peaks related to Pd sulfide were detected.

STEM-HAADF and STEM-EDS images of Pd/γ-Al_2O_3 before or after each treatment are shown in Figures 6-6. STEM image of fresh Pd/γ-Al_2O_3 shows that the Pd particle size was

around 2-3 nm. Figure 6-6(b2) shows the STEM images of the heat-treated catalyst. The size of Pd particles mostly increased to about 10-30 nm after heating, while Pd particles of 2-3 nm in size partly remained. These results agreed with the observations in the EXAFS studies described above. The size of the Pd particles remained between 10 and 30 nm after the SO_2 treatment. S species were detected from the entire catalyst surface according to the elemental mapping of S by STEM-EDS.

Figure 6-7 shows the S K-edge XANES spectra to identify the sulfur-containing species on the catalyst surface formed by SO_2 treatment. XANES spectrum of SO_2 treated catalyst shows a peak attributed to SO_4^{2-} at 2481.6 eV. No peaks attributable to SO_2 or S^0 were detected. The molar ratio of S/Pd after SO_2 treatment was 2.81. The surface concentration of the sulfate was estimated to be 0.66 molecules/nm2, indicating that the surface coverage of the sulfate was below a monolayer based on the quantity of sulfate and the catalytic surface area.

FTIR spectra of the catalyst under SO_2 flow at 600 °C to identify the sulfate species formed on the catalyst surface in the SO_2 treatment (Figure 6-8). Before measuring, the catalyst was pretreated at 800 C in air. The peaks around 1020 and 1400 cm^{-1} were detected, which are attributed to adsorbed SO_2 and aluminum sulfate on the surface, respectively [22-26].

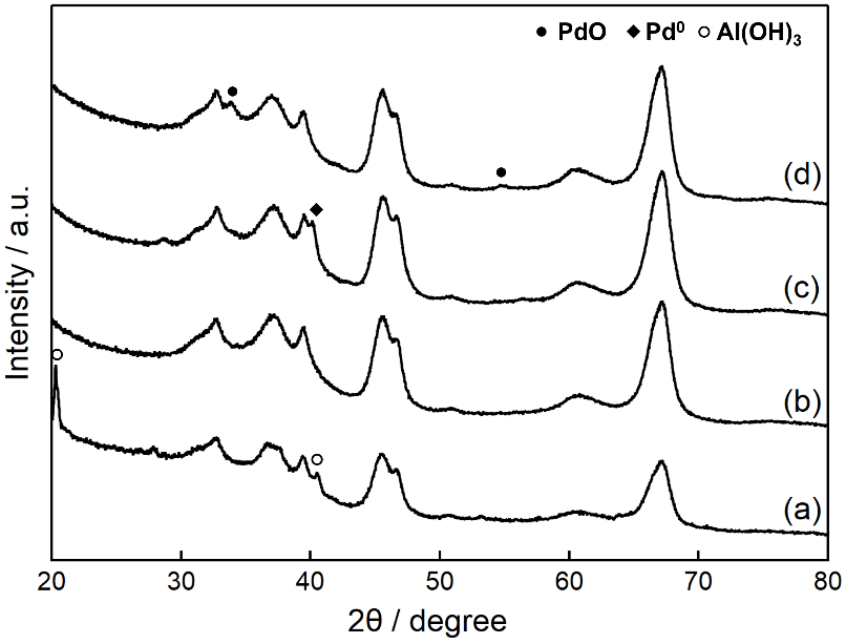

Figure 6-3. XRD patterns of supports and Pd catalysts (a)γ-Al_2O_3; (b)Pd/γ-Al_2O_3; (c)the catalyst heated at 800 ˚C; (d)the catalyst heated at 800 ˚C and SO_2 treated at 600 ˚C.

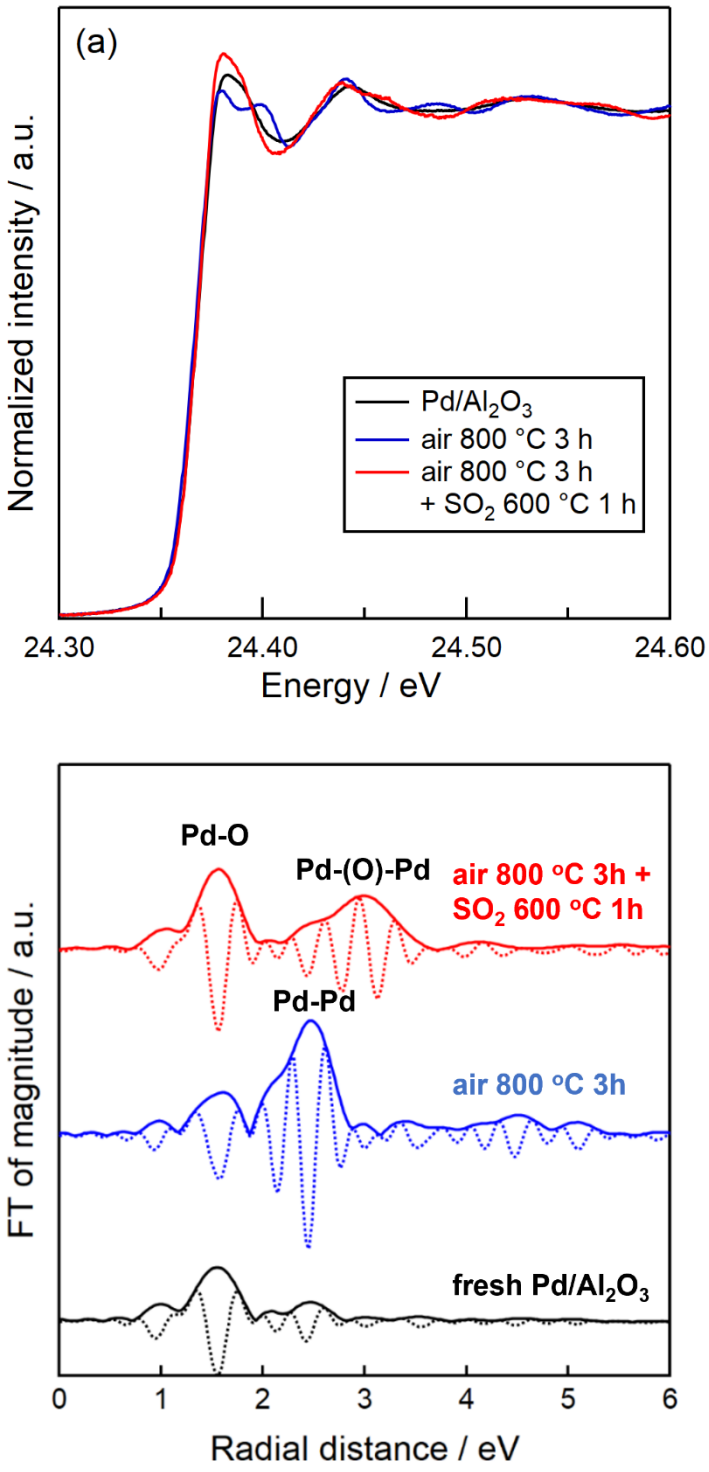

Figure 6-4. (a)Pd K-edge XANES spectra of Pd/γ-Al_2O_3 and after each treatment Pd/γ-Al_2O_3 (b)EXAFS spectra and imaginary parts of Pd/γ-Al_2O_3 and after each treatment.

(—) fresh Pd/γ-Al_2O_3 catalyst; (—) the catalyst heated at 800 ˚C; (—) the catalyst heated at 800 ˚C and SO_2 treated at 600 ˚C.

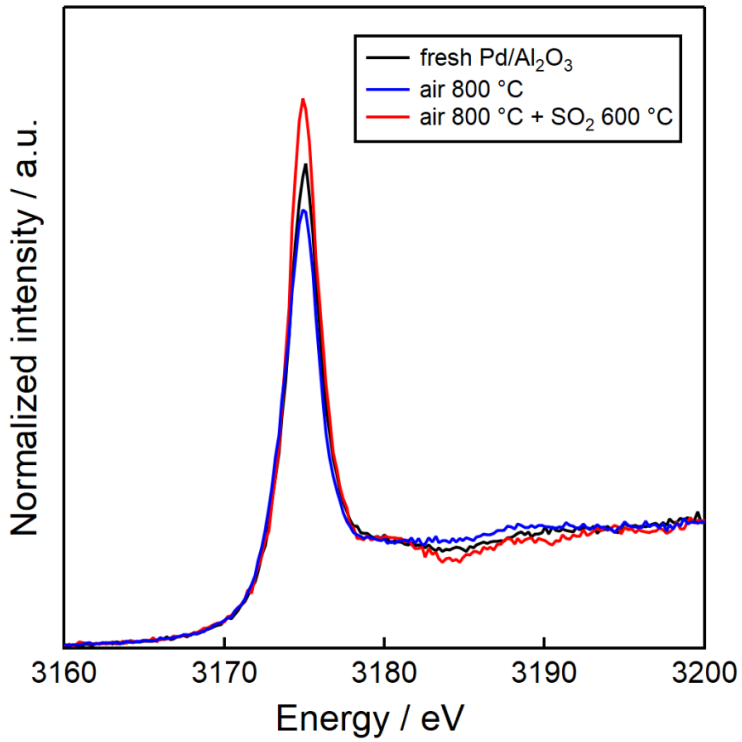

Figure 6-5. Pd L_3-edge XANES spectra of Pd/γ-Al_2O_3 and after each treatment.

(—) fresh Pd/γ-Al_2O_3 catalyst; (—) the catalyst heated at 800 ˚C; (—) the catalyst heated at 800 ˚C and SO_2 treated at 600 ˚C.

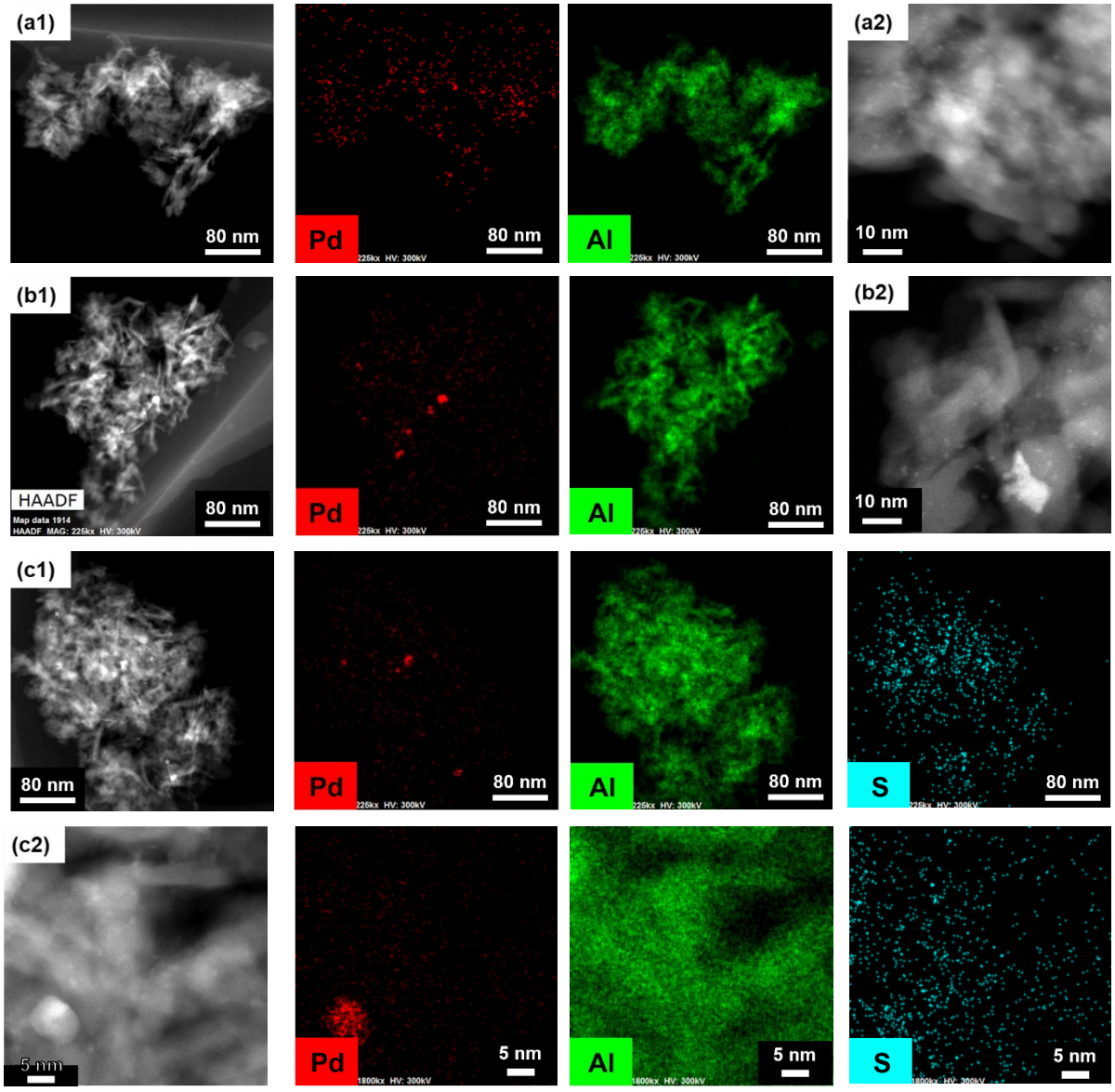

Figure 6-6. STEM-HAADF and STEM-EDS images of (a1) (a2) fresh Pd/γ-Al_2O_3 catalyst; (b1) (b2) the catalyst heated at 800 ˚C; (c1) (c2) the catalyst heated at 800 ˚C and SO_2 treated at 600 ˚C.

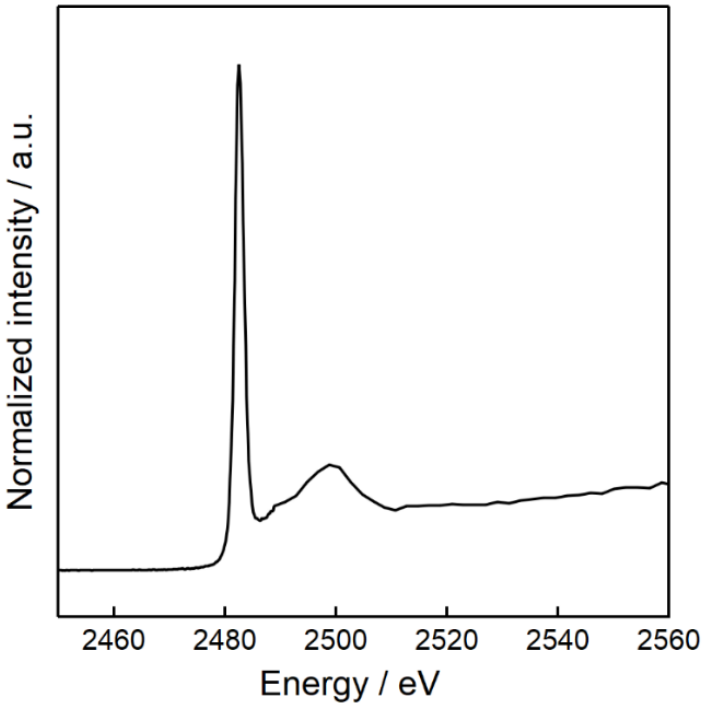

Figure 6-7. S K-edge XANES spectra of SO_2 treated catalyst.

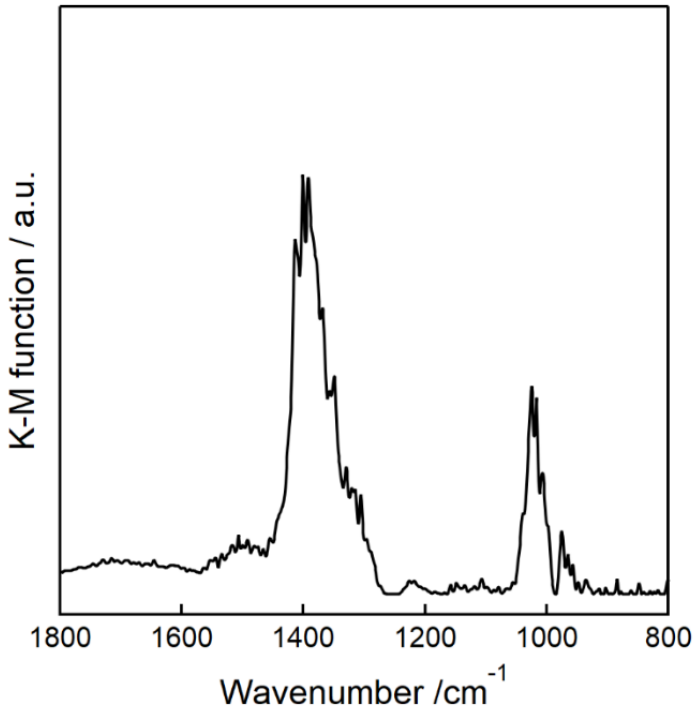

Figure 6-8. FTIR spectra of SO_2 treated catalyst.

6.3.3 Effect of SO_2 on benzene adsorption and desorption characteristics

The adsorption capacities for benzene before and after SO_2 treatment was investigated. The time course of benzene adsorption on variously pretreated Pd/γ-Al_2O_3 catalysts is shown in Figure 6-9. Before the measurements, the catalyst was heated at 350 °C in N_2 flow. Table 6-2 shows the amount of benzene adsorbed determined from the breakthrough curves. The adsorbed amount decreased after heat treatment at 800 °C and did not increase after the SO_2 treatment.

After benzene adsorption, the Pd/γ-Al_2O_3 catalyst was heated in a 20% O_2-N_2 gas flow in the range of 50-500 °C, and the temperature-programmed oxidation (TPO) profile was measured (Figure 6-10). The TPO profiles for fresh Pd/γ-Al_2O_3 show that CO_2 production begins around 150 °C, which is consistent with the light-off temperature of the benzene oxidation (Figure 6-1). The larger CO_2 production peak was detected in the high-temperature region (max. 400 °C) after the production of CO_2 in the 150-280 °C range. These results suggest that there are at least two types of active Pd sites, with a smaller amount of highly active sites and a larger amount of lower active sites. The amount of CO_2 generated calculated from TPO is about 15% of the CO_2 equivalent to the amount of benzene (10.15×10^{-6} mol) as evaluated by the adsorption breakthrough curve. Then, most of the adsorbed benzene is desorbed by the N_2 purge treatment before the TPO measurement, and the TPO profile demonstrates the oxidation desorption behavior of the strongly adsorbed benzene on the catalyst.

After the Pd/γ-Al_2O_3 catalyst was heated at 800 °C, the CO_2 formation peak in the low-temperature range disappeared, and the main peak for CO_2 formation was shifted to the lower temperature side (290 °C). This demonstrates that the small amount of highly active Pd sites present in fresh Pd/γ-Al_2O_3 have disappeared, and the increase in Pd grain size due to heat treatment has reduced the activity of the majority of Pd sites. Then, SO_2 treatment of the Pd/γ-Al_2O_3 catalyst at 600 °C resulted in a slight shift of the main peak of CO_2 production to the

higher temperature side. The CO_2 production temperature was still lower than that on the high-temperature side of the fresh catalyst. This suggests that most of the catalytically active sites on the SO_2-treated Pd/γ-Al_2O_3 catalyst are more active than those on the fresh Pd/γ-Al_2O_3 catalyst. Heating at high temperatures decreased the amount of adsorbed benzene (Table 6-2). SO_2 treatment slightly decreased the amount of adsorbed benzene on the sintered Pd/γ-Al_2O_3 catalyst. These results suggest that the SO_4^{2-} species on the catalyst surface by SO_2 adsorption do not significantly affect the oxidation properties of the Pd sites.

To clarify the effect of SO_2 treatment on activity, DRIFT measurements were performed on Pd/γ-Al_2O_3 catalysts during the benzene oxidation reaction (Figure 6-11). Measurements were carried out at 275 °C, where the increase in activity due to SO_2 treatment is most pronounced. After heat treatment at 800 °C and the introduction of a benzene-N_2 gas into the catalyst, a few bands assigned to surface phenolates were detected around 1450 cm^{-1} and 1575 cm^{-1} [9, 27, 28]. When the gas flow was switched to benzene-O_2-N_2, bands according to surface maleate at 1312 cm^{-1} and acetate at 1370 cm^{-1} were detected, indicating that cleavage of the benzene ring occurred. Bands attributed to surface phenolates at 1450 cm^{-1} and 1575 cm^{-1}, and a band attributed to benzoquinone at 1670 cm^{-1} were also detected [9, 27, 28]. The intensity of these bands increased with time, demonstrating that these partial oxidation products were retained on the catalyst surface.

For the SO_2-treated catalyst in benzene-N_2 flow, a negative band was detected around 1400 cm^{-1}, suggesting that the sulfate species on the catalyst surface were partially decomposed. Only peaks of surface phenolate species were detected at 1455 cm^{-1} and 1580 cm^{-1} when the gas flow was switched to benzene-O_2-N_2, and no other byproducts were observed. Therefore, the presence of SO_4^{2-} species on the catalyst surface prevented the retention of the partial oxidation products formed by benzene oxidation on the catalyst surface.

These results revealed the effect of SO_2 treatment on the catalytic activity of Pd/γ-Al_2O_3 catalysts for benzene oxidation. Fresh Pd/γ-Al_2O_3 catalyst has a small amount of highly active Pd sites, contributing to their high catalytic activity. Pd particles are coarsened to form Pd particles of about 20-30 nm by the heat treatment of the Pd/γ-Al_2O_3 catalyst at 800 °C. The TPO profile reveals that this treatment increases the reactivity of most of the less active Pd sites. This finding indicates that 20-30 nm Pd particles are intrinsically more active for benzene oxidation than PdO particles of 2-3 nm. However, increasing the PdO particle size from 2-3 nm to about 20-30 nm reduced the amount of PdO exposed on the surface to about 1/100, resulting in a decrease in benzene oxidation activity. On the other hand, the formation of surface sulfate on the SO_2-treated catalyst improves the benzene oxidation activities of the aggregated Pd sites, inhibiting the formation of partially-oxidized byproducts or promoting their oxidation.

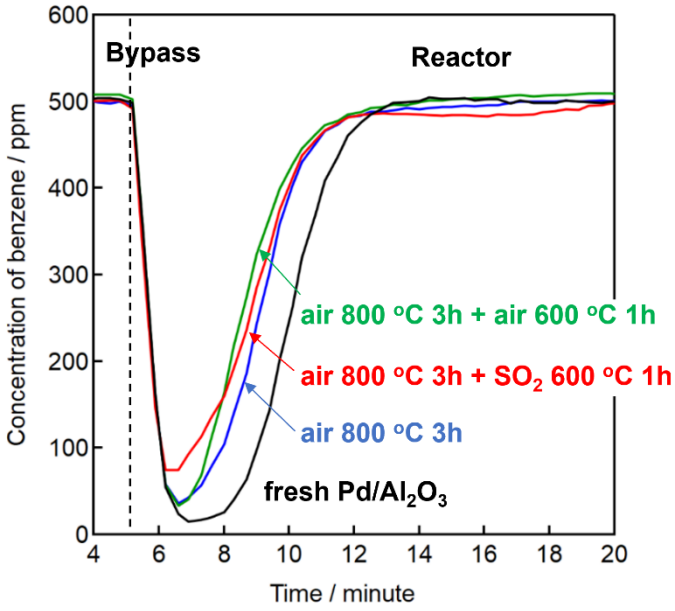

Figure 6-9. Benzene adsorption of Pd/γ-Al_2O_3 after each treatment.

(—) Fresh Pd/γ-Al_2O_3 catalyst; (—) the catalyst heated at 800 ˚C; (—) the catalyst heated at 800 ˚C, and SO_2 treated at 600 ˚C; (—) the catalyst heated at 800 ˚C, and then 600 ˚C in the absence of SO_2.

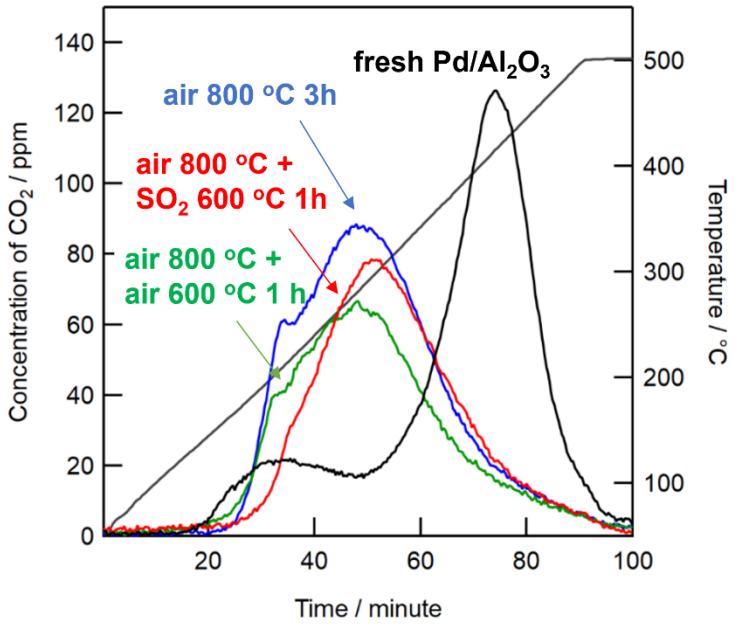

Figure 6-10. TPO profiles of Pd/γ-Al_2O_3 after each treatment.

(—) Fresh Pd/γ-Al_2O_3 catalyst; (—) the catalyst heated at 800 ˚C; (—) the catalyst heated at 800 ˚C, and SO_2 treated at 600 ˚C; (—) the catalyst heated at 800 ˚C, and then 600 ˚C in the absence of SO_2.

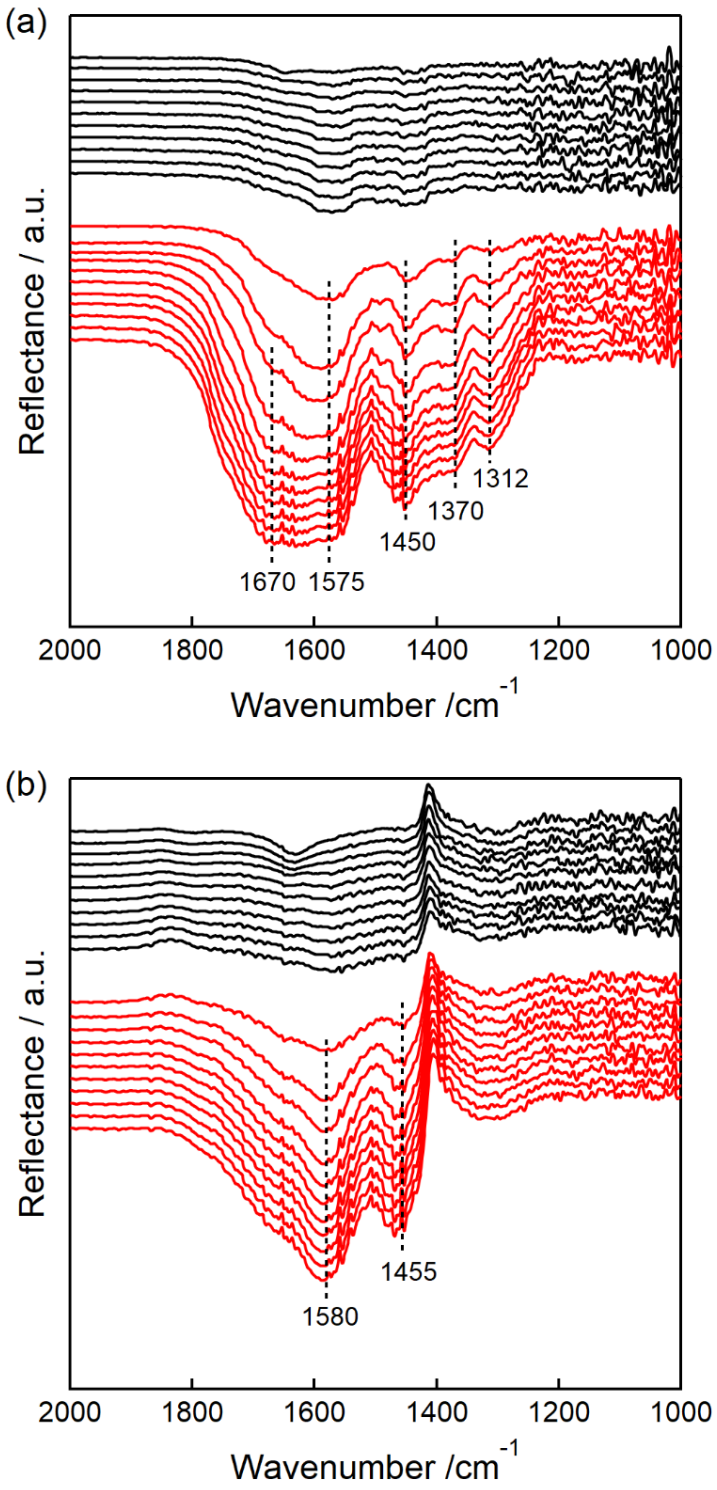

Figure 6-11. FTIR spectra under reaction gas flow at 275 ˚C of (a)the catalyst heated at 800 ˚C; (b)the catalyst heated at 800 ˚C, and SO_2 treated at 600 ˚C.

(—)benzene-N_2; (—)benzene-O_2-N_2, measuring time = 1, 3, 5, 10, 15, 20, 25, 30 min.

Table 6-2. Surface area of Pd/γ-Al_2O_3 and the amount of adsorbed benzene after various treatment.

Treatment	Adsorbed benzene / $\times 10^{-6}$ mol
—	10.15
Heat treatment[a]	8.46
SO_2 treatment[b]	8.12

[a] Catalyst was heated at 800 ˚C in air.

[b] Catalyst was heated at 800 ˚C in air and SO_2 treated at 600 ˚C.

6.4 Conclusion

In this chapter, I focused on the benzene oxidation activity of Pd/γ-Al_2O_3, a widely used catalyst for VOC oxidation. The activity was improved by SO_2 treatment after the activity was reduced by sintering due to high-temperature treatment. According to XAFS studies, Pd species existed as coarsened PdO and did not form sulfides or sulfites. According to HAADF-STEM analysis, SO_4^{2-} species were distributed over Pd/γ-Al_2O_3 catalyst. The high-temperature treatment enhanced the activity of most PdO species according to benzene adsorption and TPO studies of the treated catalysts. However, the amount of active sites is significantly reduced, resulting in reduced catalytic activity. According to DRIFT studies, SO_2 treatment suppressed the formation of byproduct compounds on the catalyst, resulting in increased activity for benzene oxidation.

References

[1] Kamal, M. S.; Razzak, S. A.; Hossain, M. M. Catalytic Oxidation of Volatile Organic Compounds (VOCs) – A Review. *Atmos. Environ.* **2016**, *140*, 117–134.

[2] Zhang, Z.; Jiang, Z.; Shangguan, W. Low-Temperature Catalysis for VOCs Removal in Technology and Application: A State-of-the-Art Review. *Catal. Today* **2016**, *264*, 270–278.

[3] Cordi, E. M.; Falconer, J. L. Oxidation of Volatile Organic Compounds on Al_2O_3, Pd/Al_2O_3, and PdO/Al_2O_3Catalysts. *J. Catal.* **1996**, *162* (1), 104–117.

[4] Ihm, S.-K.; Jun, Y.-D.; Kim, D.-C.; Jeong, K.-E. Low-Temperature Deactivation and Oxidation State of $Pd/\gamma\text{-}Al_2O_3$ Catalysts for Total Oxidation of N-Hexane. *Catal. Today* **2004**, *93-95*, 149–154.

[5] Kim, S. C.; Shim, W. G. Properties and Performance of Pd Based Catalysts for Catalytic Oxidation of Volatile Organic Compounds. *Appl. Catal. B* **2009**, *92* (3), 429–436.

[6] Liotta, L. F. Catalytic Oxidation of Volatile Organic Compounds on Supported Noble Metals. *Appl. Catal. B* **2010**, *100* (3), 403–412.

[7] He, Z.; He, Z.; Wang, D.; Bo, Q.; Fan, T.; Jiang, Y. Mo-Modified Pd/Al_2O_3 Catalysts for Benzene Catalytic Combustion. *J. Environ. Sci.* **2014**, *26* (7), 1481–1487.

[8] Haneda, M.; Todo, M.; Nakamura, Y.; Hattori, M. Effect of Pd Dispersion on the Catalytic Activity of Pd/Al_2O_3 for C3H6 and CO Oxidation. *Catal. Today* **2017**, *281*, 447–453.

[9] Kang, S.; Wang, M.; Zhu, N.; Wang, C.; Deng, H.; He, H. Significant Enhancement in Water Resistance of Pd/Al_2O_3 Catalyst for Benzene Oxidation by Na Addition. *Chin. Chem. Lett.* **2019**, *30* (7), 1450–1454.

[10] Bartholomew, C. H. Mechanisms of Catalyst Deactivation. *Appl. Catal. A* **2001**, *212* (1), 17–60.

[11] Xu, Q.; Kharas, K. C.; Croley, B. J.; Datye, A. K. The Sintering of Supported Pd Automotive Catalysts. *ChemCatChem* **2011**, *3* (6), 1004–1014.

[12] Hansen, T. W.; Delariva, A. T.; Challa, S. R.; Datye, A. K. Sintering of Catalytic Nanoparticles: Particle Migration or Ostwald Ripening? *Acc. Chem. Res.* **2013**, *46* (8), 1720–1730.

[13] Pinna, F.; Menegazzo, F.; Signoretto, M.; Canton, P.; Fagherazzi, G.; Pernicone, N. Consecutive Hydrogenation of Benzaldehyde over Pd Catalysts: Influence of Supports and Sulfur Poisoning. *Appl. Catal. A* **2001**, *219* (1), 195–200.

[14] Oudar, J. Sulfur Adsorption and Poisoning of Metallic Catalysts. *Catalysis Reviews* **1980**, *22* (2), 171–195.

[15] Sharma, H. N.; Sharma, V.; Mhadeshwar, A. B.; Ramprasad, R. Why Pt Survives but Pd Suffers From SOx Poisoning? *J. Phys. Chem. Lett.* **2015**, *6* (7), 1140–1148.

[16] Mowery, D. L.; Graboski, M. S.; Ohno, T. R.; McCormick, R. L. Deactivation of PdO–Al_2O_3 Oxidation Catalyst in Lean-Burn Natural Gas Engine Exhaust: Aged Catalyst Characterization and Studies of Poisoning by H_2O and SO_2. *Appl. Catal. B* **1999**, *21* (3), 157–169.

[17] Kinnunen, N. M.; Nissinen, V. H.; Hirvi, J. T.; Kallinen, K.; Maunula, T.; Keenan, M.; Suvanto, M. Decomposition of Al_2O_3-Supported $PdSO_4$ and $Al_2(SO_4)_3$ in the Regeneration of Methane Combustion Catalyst: A Model Catalyst Study. *Catalysts* **2019**, *9* (5), 427.

[18] Ivanova, A. S.; Slavinskaya, E. M.; Gulyaev, R. V.; Zaikovskii, V. I.; Stonkus, O. A.; Danilova, I. G.; Plyasova, L. M.; Polukhina, I. A.; Boronin, A. I. Metal–support Interactions in Pt/Al_2O_3 and Pd/Al_2O_3 Catalysts for CO Oxidation. *Appl. Catal. B* **2010**, *97* (1), 57–71.

[19] Chen, X.; Cheng, Y.; Seo, C. Y.; Schwank, J. W.; McCabe, R. W. Aging, Re-Dispersion, and Catalytic Oxidation Characteristics of Model Pd/Al_2O_3 Automotive Three-Way Catalysts. *Appl. Catal. B* **2015**, *163*, 499–509.

[20] Cui, W.; Li, S.; Wang, D.; Deng, Y.; Chen, Y. High Reactivity and Sintering Resistance of CH_4 Oxidation over Modified Pd/Al_2O_3. *Catal. Commun.* **2019**, *119*, 86–90.

[21] Tew, M. W.; Miller, J. T.; van Bokhoven, J. A. Particle Size Effect of Hydride Formation and Surface Hydrogen Adsorption of Nanosized Palladium Catalysts: L_3 Edge vs K Edge X-Ray Absorption Spectroscopy. *J. Phys. Chem. C* **2009**, *113* (34), 15140–15147.

[22] Shimizu, K.-I.; Kamiya, Y.; Osaki, K.; Yoshida, H.; Satsuma, A. The Average Pd Oxidation State in Pd/SiO_2 Quantified by L_3 -Edge XANES Analysis and Its Effects on Catalytic Activity for CO Oxidation. *Catalysis Science & Technology* **2012**, *2* (4), 767–772.

[23] Abdulhamid, H.; Fridell, E.; Dawody, J.; Skoglundh, M. In Situ FTIR Study of SO_2 Interaction with $Pt/BaCO_3/Al_2O_3$ NOx Storage Catalysts under Lean and Rich Conditions. *J. Catal.* **2006**, *241* (1), 200–210.

[24] Colussi, S.; Arosio, F.; Montanari, T.; Busca, G.; Groppi, G.; Trovarelli, A. Study of Sulfur Poisoning on Pd/Al_2O_3 and $Pd/CeO_2/Al_2O_3$ Methane Combustion Catalysts. *Catal. Today* **2010**, *155* (1), 59–65.

[25] Zhao, L.; Li, X.; Hao, C.; Raston, C. L. SO_2 Adsorption and Transformation on Calcined NiAl Hydrotalcite-like Compounds Surfaces: An in Situ FTIR and DFT Study. *Appl. Catal. B* **2012**, *117-118*, 339–345.

[26] Konsolakis; Yentekakis; Pekridis. Insights into the Role of SO_2 and H_2O on the Surface Characteristics and de-N_2O Efficiency of Pd/Al_2O_3 Catalysts during N_2O Decomposition in the Presence of CH_4 and O_2 excess, *Appl. Catal. B* **2013**.

[27] Lichtenberger, J.; Amiridis, M. D. Catalytic Oxidation of Chlorinated Benzenes over V_2O_5/TiO_2 Catalysts. *J. Catal.* **2004**, *223* (2), 296–308.

[28] Zeng, J.; Liu, X.; Wang, J.; Lv, H.; Zhu, T. Catalytic Oxidation of Benzene over $MnOx/TiO_2$ Catalysts and the Mechanism Study. *J. Mol. Catal. A Chem.* **2015**, *408*, 221–227.

Chapter 7 Conclusions

Supported Pd catalysts are key materials for reducing the environmental load caused by air pollution. Exhaust gas emission regulations to prevent air pollution are becoming stricter. Furthermore, the price of Pd has skyrocketed due to the rapid increase in demand and current social conditions, and reducing the amount of Pd used is required. Therefore, the development of highly active Pd catalysts is required. Investigation of the influence of sulfur species is necessary for designing highly active catalysts. In this study, the effects of support, transition metal addition, and sulfur species on the catalytic properties of Pd-supported catalysts were investigated to develop high-performance Pd catalysts. The main research contents and results are as follows:

Chapter 1 outlines the research background of this study and the fundamentals of catalytic chemistry.

In Chapter 2, the effect of the support on the CO oxidation reaction under dilute O_2 conditions was examined, and Pd/CeO_2 showed higher catalytic activity in the low-temperature region below 180 °C. STEM images and XAFS measurements revealed that Pd particles on CeO_2 were more highly dispersed than those on TiO_2 and Al_2O_3. FTIR measurements showed that Pd on CeO_2 exists as PdO in an atmosphere and is reduced to Pd^0 under CO flow. Furthermore, oxidative desorption of CO species adsorbed on Pd/CeO_2 is faster than that of CO species on Pd/TiO_2 and Pd/Al_2O_3.

In Chapter 3, the effect of SO_2 on the catalytic structure of Pd/CeO_2 was investigated by *in situ* XAFS measurements to observe the changes under SO_2 flow. *in situ* XAFS measurements revealed that SO_2 treatment at 500 °C sulfurized the surface lattice of CeO_2 to form sulfate and Ce^{3+} species. SO_2 treatment did not form Pd sulfides, and the entire Pd/CeO_2 catalyst surface

was sulfurized. Furthermore, Pd loading on the CeO_2 promoted sulfurization of the support CeO_2.

In Chapter 4, morphology-controlled c-CeO_2 was prepared, and the effect of SO_2 on the CeO_2 structure of Pd/CeO_2 was analyzed at the atomic level using STEM-EELS measurements. Pd was highly dispersed on c-CeO_2. STEM-EELS measurements revealed that SO_2 treatment at 200 °C did not change the structure of the support CeO_2, while SO_2 treatment at 400 °C reduced the support c-CeO_2 and increased the number of oxygen vacancies. Moreover, it was found that sulfurization by SO_2 is enhanced at the Pd-CeO_2 interface.

In Chapter 5, the effect of Cu addition on the CO oxidation activity of Pd/CeO_2 catalysts under dilute conditions was investigated. The addition of Cu to Pd/CeO_2 improved the activity at 90–250 °C, and Pd-Cu/CeO_2 exhibited the highest activity in all temperature ranges. Pd-Cu/CeO_2 exhibited higher activity for CO oxidation than Cu/CeO_2. The addition of Cu did not affect the electronic state of Pd and did not form Pd-Cu bimetallic particles; however, it reduced the Pd particle size and improved the dispersion of Pd.

In Chapter 6, the effect of SO_2 on VOC oxidation over Pd/Al_2O_3 was discussed. In this chapter, I found that the benzene oxidation activity of Pd/γ-Al_2O_3, a widely used catalyst for VOC oxidation, was improved by SO_2 treatment after the activity was reduced by sintering due to high-temperature treatment. Pd species existed as coarsened PdO and did not form sulfides or sulfites. DRIFT studies showed that SO_2 treatment suppressed the formation of byproduct compounds on the catalyst, resulting in increased activity for benzene oxidation.

In this study, I systematically investigated the effects of (1) the catalyst support, (2) the transition metal addition, and (3) the sulfur species on the catalytic properties of Pd catalysts. To improve catalytic activity, I investigated the effects of catalyst support and transition metal additions. The Pd-Cu/CeO_2 catalyst showed high activity in the CO oxidation reaction under

dilute O_2 conditions. In addition, the factors that contribute to activity enhancement were clarified. Furthermore, the effects of sulfur species on catalyst structure and activity were investigated in detail using various spectroscopic techniques to design catalysts highly resistant to sulfur poisoning. Traditionally, elucidating the mechanism of sulfur poisoning has been challenging due to the complexity of catalytic reactions and the difficulty of observing the local structure of actual catalysts. This study significantly contributed to elucidating the mechanism of sulfur poisoning by enabling analysis at the atomic level and under actual reaction conditions. The findings in this study are expected to be applied not only to exhaust gas purification but also to all catalytic reactions under residual sulfur, especially in petroleum refining and hydrogen production from fossil fuels.

Acknowledgements

This thesis is based on experimental work at Einaga-Hojo Laboratory, Department of Molecular and Material Sciences, Graduate School of Engineering Sciences, Kyushu University.

I would like to express my gratitude to my supervisor Professor Hisahiro Einaga for his continuous guidance.

I want to extend my thanks to Professor Hajime Hojo for his constant advice.

I thank my thesis committee, Professor Kengo Shimanoe and Professor Shinji Kudo, for their helpful discussions and guidance with my thesis.

I appreciate the support given to me by Professor Takeharu Sugiyama of the Kyushu Synchrotron Light Research Center in the XAFS measuring.

I would like to thank our secretary Ms. Akiko Nishioka for her support in our research life.

I thank all former and present members of the Einaga-Hojo Laboratory for their help and support.

I would like to thank the staff of Green Asia Course for their help.

Last but not least, I must express my sincere appreciation to my family and friends for their constant and continued support and patience.

Saki Shigenobu

February 2022